Computational Modeling of Heterogeneous Catalysis for Molecular and Kinetic Understanding of Aerobic Oxidation and Electrocatalytic Oxygen Reduction

BY

AURORA N. JANES

A DISSERTATION SUBMITTED IN PARTIAL FULFILLMENT OF
THE REQUIREMENTS FOR THE DEGREE OF

DOCTOR OF PHILOSOPHY
(CHEMISTRY)

AT THE
UNIVERSITY OF WISCONSIN MADISON
2021

Date of finale oral examination: 12/21/2020

The dissertation is approved by the following members of the Final Oral Committee:

J.R. Schmidt, Professor, Chemistry
Daniel Fredrickson, Professor, Chemistry
Shannon Stahl, Professor, Chemistry
Song Jin, Professor, Chemistry

Computational Modeling of Heterogeneous Catalysis for Molecular and Kinetic Understanding of Aerobic Oxidation and Electrocatalytic Oxygen Reduction

Abstract

Rational design of heterogeneous catalysts is of utmost importance to improve the efficiency of industrial chemical synthesis. In this thesis, we investigate two chemical reactions catalyzed by heterogeneous catalysts through theoretical modeling, the aerobic esterification of primary alcohols and the two electron oxygen reduction reaction. First, we develop a microkinetic modeling code, Micki, that both provides an easy-to-use interface for standard statistical mechanical methods for microkinetic modeling as well as novel ways to incorporate complex physics that influence the liquid-solid interface. Then we use Micki to determine the role of P block promoters for the aerobic esterification of alcohols. Tellurium atoms modify the electronic structure of the catalyst which reduces the barrier of the rate limiting step, C-H bond scission, as well as providing lower energy pathways for O_2 reduction. Next, we develop a theoretical framework to evaluate the performance of cobalt dichalcogenides based on density functional theory calculations. Together with experimental collaborators, we discover the best $2e^-$ ORR catalysts in acidic media to date as well as transferable physical principles. We apply these physical principles to nickel dichalcogenides and cobalt nickel dichalcogen alloys. We conclude that while nickel dichalcogenides show great promise for $2e^-$ ORR, the alloy does not as neighboring metal centers have little electronic influence on each other. Finally we use Micki to develop an electrochemical microkinetic model of $2e^-$ ORR on cobalt dichalcogenide catalysts and compare results to bulk electrolysis experiments. While significant work must be done to reach quantitative accuracy for electrochemical kinetic models, our results indicate qualitative trends are properly modeled and electrochemical kinetic models can be used to predict catalyst performance.

Contents

Listing of figures

Published Work and Work in Preparation

1. Hermes, Eric D.; Janes, Aurora N.; Schmidt, J.R. Mechanistic Insights into Solution-Phase Oxidative Esterification of Primary Alcohols on Pd(111) from First-Principles Microkinetic Modeling. ACS Catal. 2018, 272–282.

2. Hermes, Eric D.; Janes, Aurora N.; Schmidt, J.R. Micki: A Python-Based Object-Oriented Microkinetic Modeling Code. J. Chem. Phys. 2019, 151:1.

3. Sheng, Hongyuan; Hermes, Eric D.; Yang, Xiaohou; Ying, Diwen; Janes, Aurora N.; Li, Wenjie; Schmidt, J.R.; Jin, Song. Electrocatalytic Production of H_2O_2 by Selective Oxygen Reduction Using Earth-Abundant Cobalt Pyrite (CoS_2). ACS Catal. 2019, 9, 9, 8433–8442.

4. *Sheng, Hongyaun; *Janes, Aurora N.; Ross, R. Dominic; Kaiman, Dave; Huang, Jinzhen; Song, Bo; Schmidt, J.R.; Jin, Song. Stable and selective electrosynthesis of hydrogen peroxide and the electro-Fenton process on $CoSe_2$ polymorph catalysts. Energy Environ. Sci. 2020, 13, 4189-4203.

   *These authors contributed equally to this work.

5. Lee, Dong Ki; Kubota, Stephen; Janes, Aurora N.; Bender, Michael ; Woo, Jongin; Schmidt, J.R.; Choi, Kyoung-Shin. The Impact of 5-Hydroxymethyl Furfural (HMF)-Metal Interactions on the Electrochemical Reduction Pathways of HMF on Various Metal Electrodes. Submitted.

6. Janes, Aurora N.; Dunnington, Benjamin; Schmidt, J.R. The Role of Tellurium Dopants in the Palladium Catalyzed Esterification of Primary Alcohols. In preparation.

7. Wang, Fengmei; Mathur, Nitish; Janes, Aurora N.; Sheng, Hongyuan; He, Peng; Zheng, Xueli; Yu, Peng; Deruiter, Andrew J.; Schmidt, J.R.; He, Jun; Jin, Song. Defect Induced

Magnetism in Correlated 2D Van Der Waals Transition Metal Phosphorus Trisulfides. In preparation.

Acknowledgments

I gratefully acknowledge both financial support of this work and the tremendous research done by my collaborators. The work presented here has been funded by the National Science Foundation under Grant Nos. CHE-1362136 and CHE-1955074. Computational resources were provided by the Extreme Science and Engineering Discovery Environment (XSEDE), which is supported by National Science Foundation grant number TG-CHE120088 and the UW-Madison Center For High Throughput Computing (CHTC) in the Department of Computer Sciences. The CHTC is supported by UW-Madison, the Advanced Computing Initiative, the Wisconsin Alumni Research Foundation, the Wisconsin Institutes for Discovery, and the National Science Foundation, and is an active member of the Open Science Grid, which is supported by the National Science Foundation and the U.S. Department of Energy's Office of Science. Additionally, much of the work here was a result of collaboration with Professor Song Jin (Hongyuan Sheng and Dominic Ross).

Professionally, I would like to thank all of my mentors and colleagues for furthering my scientific curiosity and developing my research acumen. To JR, for pushing me to be independent and thorough. To Qiang Cui, Arun Yethiraj and Jim Skinner for teaching me so thoughtfully and comprehensively about quantum and statistical mechanics. Additionally, I want to thank members of the Schmidt research group for their support and scientific advice: Mary VanVleet for making sure I never got too lost, Eric Hermes for teaching me everything I know about large scale computing, Xinyi Li for going through all the steps and classes together, and my office mates, Tesia Janicki, Tinting Weng, Kai Cui and Zhongyi Wan for creating a studious but welcoming office environment. Additionally, I would like to thank my undergraduate advisors, Daniela Kohen and Deborah Gross for mentoring me and inspiring me to go to graduate school. Finally, I would like to thank Dr. Price and Mr. Spatz, my high school AP chemistry and AP calculus teachers for giving me a sounds mathematical and chemical foundation as well as showing me how much fun these subjects can be.

Personally, I would like to thank my family for all their love and support. My parents, Rebecca Smith and Nathan Janes, for having unflappable faith in my abilities. Lucas Janes and Yuvraj Joshi, for always reminding me to love myself the way I am. My grandfather, J. Charles Janes, who is not here to see the culmination of this work but was my biggest cheerleader at every step of the way. And finally, to Morgan Tuff and Jenn Shah, my emotional rocks and the two best friends a person could ask for.

0 Introduction

0.1 Importance of Heterogeneous Catalysis

Modern life has been shaped by chemical processes. Indeed, without the Haber-Bosch synthesis of ammonia, the first heterogeneous catalytic system in the chemical industry[150], only 40% of the global population could be fed.[164] 85-90% of all synthetic chemical products produced rely on catalysis at some point.[149] Catalytic processes themselves account for 25% of indus-

trial energy use.[36] The most energy intensive of these catalytic processes use heterogeneous catalysts. Most viable renewable energy sources, such as water splitting, rely on heterogeneous catalysis. Improving and rationally designing heterogeneous catalysts is crucial to fighting a major threat facing society today, climate change. Not only does improving current heterogeneous catalysts lower energy use, but developing new heterogeneous catalysts offers opportunities for development of sustainable, renewable resources.

While historically improvements of heterogeneous catalysts were made through trial and error, advancements in experimental[36] and theoretical techniques[124,185] have allowed for highly controlled, rationally designed processes. However, heterogeneous catalysis involves complex chemical and physical phenomena; therefore significant work is still needed to identify key parameters that control results such as selectivity, activity and stability. At its core, catalysis involves a material or chemical species interacting with chemical reactants and intermediates to reduce the energy barrier for the reaction to occur *without* the catalyst being consumed. For example, the water gas shift (WGS), an important source of $H_{2(g)}$ involves the reaction of CO and H_2O to form CO_2 and H_2 and is important for the growing shift towards a renewable hydrogen economy.[166] This reaction traditionally occurs over iron-chromium or coppper-zinc catalysts. CO and H_2O adsorb to the catalyst surface where H-O bonds are broken and H-H and C-O bonds are formed and then the products H_2O and H_2 desorb.[132]

Catalysts can be homogeneous, where catalyst and reactants are the same phase, or heterogeneous, where catalyst and reactants are different phases. While homogeneous catalysts can play an important role in industrial production of chemicals (for example, in the production of low-volume, high-value chemicals from biomass)[8] and offer many benefits over heterogeneous catalysts, they have one major disadvantage: the catalyst must be separated from the product, which is expensive, time consuming and often energy intensive.[24] By contrast, as long as a heterogeneous catalyst does not suffer from serious degradation (an important concern), the

product desborbs from the catalyst surface and is easily filtered from the reactor.

There are myriad number of metrics from which to evaluate a successful catalyst. From a business perspective, catalysts should be cheap and long-lasting. Environmentally green catalysts should operate at low temperatures and pressures to reduce energy use, utilize non-hazardous chemicals (i.e. not mercury) and be stable so as not to leach into the environment. Chemically, catalysts are evaluated on selectivity (do they produce the desired product at higher rates than undesired side-products?) and activity (how much of the product does the catalysts produce per amount of catalyst per unit time?) Other factors arise from the reactor design. For example, the catalyst needs to to be exposed to the reactant to catalyze the reaction. If the catalyst has a low active surface area, catalyst activity will decrease.[11] However, a rougher catalyst surface complicates surface characterization efforts.

Fully understanding and evaluating a working catalyst is a multi-scale problem. Catalytic performance is not only defined by the atomic level molecular processes taking place on active sites, but also by macroscopic scale factors such as reaction conditions and the design of the reactor. These complicated processes, occurring at multiple lengths and time scales are a challenge to investigate and understand in situ. As a result, fundamental physical chemistry can be exploited to experimentally and theoretically investigate catalyst surfaces for rational design.

0.2 Theoretical Questions for Catalyst Surfaces

While scientists who investigate working catalysts *in situ* have the task of analyzing a complex, multi-scale process and trying to disentangle interweavings of various physical and chemical processes, fundamental physical chemists (both experimental and theoretical) have the opposite problem. Given the simplest version of the system, we must build into our models the most necessary physics and chemistry and extrapolate principles to the working system.

Connecting the simplified model to the actual reactor system has been referred to as bridging the ”materials gap” or the ”pressure gap.” These terms come from the limitations of many experimental characterization methods that require simplified versions of the working catalyst, such as single-crystal surface models instead of the more structurally complex catalysts required for efficient heterogeneous catalysis[144] or from the low pressures needed for ultra-high vacuum (UHV) experiments.[171]

These same type of gaps between model systems and working catalyst reactors exist for theoretical models. While significant advances in both speed and robustness of computational methodology as well as increased access to supercomputing has greatly increased the feasibility of complex computational heterogeneous modeling, current modeling methods still must make significant simplifications. Most heterogeneous catalysis studies rely on density functional theory (DFT), which uses the electron density, a function of three spatial variables, instead of the electronic wavefunction, which is a function of 3N spatial variables,[82] where N is is the number of electrons (which is a very large number for most solids). In order to implement DFT, one must approximate the exchange-correlation potential. Many approaches for approximating the exchange-correlation potential have been attempted. These correlation-exchange functionals have been benchmarked against a variety of metrics and depending on the exact system and computational effort, qualitative and sometimes even quantitative insight can be obtained. Currently, within DFT, bond lengths are reproduced within $\pm$ 0.02 Å, vibrational frequencies within 5%-10% and adsorption energies within 0.1-0.2 eV.[149] While these approaches do not ensure chemical accuracy, they can prove insightful and, as approximations generally show systematic deviations. often reproduce trends with greater precision.

Technically, DFT results strictly describe T=0 and P=0. However, these effects can be added *posteriori* through statistical mechanics. In the isothermal-isobaric (NpT) ensemble the free

energy is

$$G(T) = H(T) - TS(T) = E_{(0)} + E_{ZPE} + p\Delta V - TS(T) \quad (1)$$

where G is the Gibbs free energy of a species, H is the enthalpy of a species, T is the temperature, S is the entropy of a species, E_0 is the DFT calculated potential energy of the species, E_{ZPE} is the zero point energy correction, p is the pressure and V is the volume. ZPE and entropy can be approximated using statistical mechanics. Gas and solution phase entropies are calculated using the ideal gas partition function. For surface bound species, all degrees of freedom are usually treated as vibrational degrees of freedom and calculated using the harmonic approximation and ideal gas vibrational partition function. This approximation is more accurate in the limit of strongly bound species. More complex entropy models are necessary as a weakly adsorbed species approaches the limit of an adsorbed 2D gas.

Reaction barriers can be calculated using transition state theory (TST). Assuming that the energy of the reactant region is Boltzman distributed, the reaction is adiabatic, no tunneling occurs and no recrossing from the product to reactant state occur. Then the rate constant k_{TST} is

$$k_{TST} = \frac{kT}{h} exp(\frac{-\Delta G_{TS}}{kT}) \quad (2)$$

where k is the Boltzman constant, h is planck's constant, T is the temperature and ΔG_{TS} is

$$\Delta G_{TS} = G_{TS} - G_{IS} \quad (3)$$

where G_{TS} and G_{IS} are the free energies of the transition state and initial state respectively and calculated using Equation 1.

While working catalysts are usually large, rough and irregular solid materials, *in silico* models are usually small unit cells of perfect crystal facets for computational efficiency. Then periodic DFT repeats the unit cell in three dimensions to create a perfect, infinite surface for catalysis. Choosing the correct facet to study is of utmost importance for computational modeling. If the active site is a kink or corner and the computational model is a flat surface, the idealized model will not reproduce the catalyst chemistry property. Generally, no systematic ways to predict the active site for a reaction on a metal surface exist.[149] Many periodic DFT models lack realistic solvation effects. Full treatment of solvent effects requires consideration of all solvent electronic degrees of freedom and appropriate sampling of solvent nuclear degrees of freedom, which is currently prohibitively expensive on all but the simplest systems. Methods to capture the largest solvent effects, through schemes such as implicit solvent, however are now computationally feasible.

More complications arise when *in silico* models attempt to model electrochemical reactions. Traditional DFT calculations occur at constant number of electrons while electrochemical experiments are performed at constant potential. Accurate models of the complex double layer created at the catalyst surface are still quite crude. Proton coupled electron transfer (PCET) reactions are poorly described by the traditional transition state theory framework.

Nevertheless, despite all the difficulties representing the complex nature of the working catalyst *in silico*, computational models have provided significant knowledge for screening catalysts for a given reaction as well as creating transferable physical principles to understand catalyst activity. Adsorption energies on a catalyst surface are linearly correlated to each other. For example the binding energy of CH, CH_2 and CH_3 are all linearly correlated to the binding energy of C on surface.[1] These types of correlations also occur between catalyst surfaces. One example is the use of the Nitrogen binding energy to form a so-called volcano plot for the ammonia synthesis reaction to predict the surfaces with the most optimal binding energy.[95] These

linear correlations mean that DFT errors will be systematic, meaning differences in adsorption energies are fairly accurate. Additionally, a significant amount of the complex physical processes occurring in the working catalyst will affect the adsorption energy of species in similar ways. While *in silico* modeling cannot yet reach quantitative, chemical accuracy, it can accurately compare trends across species and catalyst surfaces and prove predictive in catalytic design..

The objective of this research is to create transferable physical principles of catalyst performance and predict new catalysts in collaboration with experimental results, all with the goal of furthering rational catalyst design. We do this by utilizing state-of-the-art DFT methodologies, leveraging correlations between energetics and determining methods to model the most relevant physics for catalysis.

0.3 Overview

In Chapter 1, I present the microkinetic modeling code Micki. Not only does this code create an easy-to-use interface for the traditional framework used in microkinetic modeling, it also offers new ways of modeling important physical processes that are often missing from microkinetic models, such as mass transport limited adsorption, lateral surface interactions and multidentate binding. In Chapter 2, Micki is used to build microkinetic models of the aerobic esterification of primary alcohols on both Pd(111) surfaces and a PdTe(111) system. Comparisons between the models establish the role of Te atoms in the promotion of the reaction.

Chapter 3 details the analysis of $2e^-$ oxygen reduction (ORR) catalysts for the electrochemical synthesis of H_2O_2. By developing computational descriptors to assess the activity, selectivity and stability of a catalyst, we compare the performance of three cobalt dichalcogenides catalysts. In tandem with experimental collaborators, this work led to the discovery of the best

two electron ORR catalysts in acidic media to date. Chapter 4 employs the framework developed in chapter 3 to investigate nickel dichalogenides and nickle cobalt alloy dichalcogenides for $2e^-$ ORR to identify potential avenues of future experimental investigation. Finally, in Chapter 5, we modify Micki to model electrochemical reactions and build microkinetic models of two cobalt dichalcogenide catalysts for two electron ORR with experimental validation.

1

Micki: A Python-Based Object-Oriented Microkinetic Modeling Code

Reproduced in part with permission from Hermes, E. D.; Janes, A. N.; Schmidt, J.R. Micki: A python-based object-oriented microkinetic modeling code. J. Chem. Phys. 2019, 1(151), 014112.[61]

EDH wrote the initial draft of the Micki code and performed electronic structure calcuations for the water gas shift model. ANJ prepared the manuscript and addressed reviewer comments, completed the working example of the water gas shift microkinetic model, and derived the mathematical description of the plug flow reactor. Additionally, as the first user of Micki, ANJ contributed towards testing and refining the code for both accuracy and usability.

1.1 Introduction

Kinetic modeling is a powerful tool for simulating and interrogating complex reaction networks. It can be used to extrapolate experimental data to alternative reaction conditions or predict the behavior of a complex reaction network from first-principles electronic structure data. Perhaps most importantly, the resulting kinetic models also provide insight into the ways in which a catalytic process can be optimized by identifying rate-limiting steps or rate-inhibiting side-pathways.

Atomically-detailed kinetic models (e.g. kinetic Monte Carlo) of heterogeneous catalytic reaction networks are impractical for all but the simplest systems, necessitating several common approximations to make progress. One such approximation is the mean field approximation, where the local surface occupation of a species is represented by a single (average) concentration. This is the approach used in microkinetic modeling, in which a reaction network is expressed as a system of differential algebraic expressions that are amenable to numerical solution.[27] Currently, most microkinetic modeling packages are not open source (e.g. CHEMKIN[142]) or are designed with a particular application in mind (such as descriptor-based

catalyst screening or gas-phase combustion) and are therefore insufficiently general for the purpose of modeling arbitrarily-complex reaction networks.[40,44,112] For example, Cantera[44] is software suite written in C++ for solving systems of chemical kinetics equations and was designed primarily to model gas-phase kinetics and with mass/heat transport. The package requires manual declaration of rate equations and appears to be limited to Arrhenius rate expressions. CatMAP is another popular microkinetic modeling package,[112] but is designed mainly to perform catalysis screening using scaling relations and scanning over a variety of user-specified descriptors. Given the focus on catalyst screening, CatMAP lacks the flexibility to model various reactor types (e.g. batch reactor vs. plug flow) and lacks integration with a fully featured high-performance differential equation solver (e.g. Sundials). Many studies forego the use of microkinetic modeling packages altogether, instead relying on custom-written scripts (often in Matlab or Python) which explicitly invoke the underlying differential equation solver.[46,76,7,170,20] This approach, while mathematically sound, fails to create a clear distinction between the high-level view of a microkinetic model (as a web of reactions between chemical species) and the low level view (as a system of differential equations). This greatly increases the difficulty in developing, using, modifying and teaching microkinetic modeling and thus limits the growth of the scientific field.

This motivated us to develop our own code: Micki. Micki utilizes a modern, object-oriented, modular design that exploits analogies familiar to chemists (reactants, reactions, energies, entropies...) and interfaces with common electronic structure codes (such as VASP) via the Atomic Simulation Environment (ASE)[90]. Because Micki uses symbolic expressions to represent reaction rates, it is possible to introduce lateral interactions and other modifications to model parameters of arbitrary functional form. It is also fast and thus capable of performing many simulations under varying initial conditions or differing model parameters. This enables Micki to perform sensitivity analysis and/or to fit the model parameters to prior experimental

observations.

In the following sections, we first derive the thermodynamic and kinetic parameters necessary for first-principles microkinetic modeling, including aspects that are typically neglected in other rigorous derivations (lateral interactions, multi-dentate binding). Next, we detail the novel functionality present in Micki, which allows the package to account for diffusion limited reactions, thermodynamically consistent lateral interactions and Brønsted–Evans–Polanyi (BEP) estimates of changes in barrier height. Third, we explain the basic structure of the code, including sample input and output. Finally, we provide an example application of Micki to model the water gas shift (WGS) reaction on Pt(111) and compare our results to prior experimental and microkinetic modeling results of Grabow et al.[46]

1.2 Thermodynamic and Kinetic Parameters

Within standard microkinetic models, the catalytic system of interest is divided into two phases: the vapor or fluid phase, which contains reactants and products, and the catalyst surface. The fluid phase is treated as a mean field, meaning that species are characterized by a homogeneous concentration. Adsorption of species from the fluid phase onto the surface is governed by the rate of their collisions with the catalyst surface. The surface is represented as a lattice, where each site can be occupied by at most one adsorbate at a time. Each adsorbate on the catalyst surface is represented by a mean-field coverage.

A microkinetic model requires, as input, a list of all plausible catalytic elementary reaction steps. The thermodynamic and kinetic parameters of the model are then calculated using quantum chemistry and statistical thermodynamics or fit to experimental measurements; these approaches can also be combined, where experimental data is used to refine parameters that have been estimated from first principles, as will be shown later.

Given a set of elementary reactions, $\{r_i\}$, Micki constructs an expression for the overall flux of each species C_i

$$\frac{dC_i}{dt} = \sum_{n=1}^{N_i} r_n - \sum_{m=1}^{M_i} r_m \tag{1.1}$$

where r_n is a reaction that forms C_i and r_m is a reaction that consumes C_i. This set of $\{\frac{dC_i}{dt}\}$ for all species i in the system form the set of differential equations that must be solved numerically.

1.2.1 Partition functions

Microkinetic models require estimates of rate constants and related equilibrium constants for each elementary step. We calculate these quantities using the ideal gas partition function for the fluid phase (corrected for solvation, if required) and the mean field lattice partition function for the catalyst surface. The partition function for the full system is therefore a product of these two subsystems.

Ideal Gas

The fluid phase is frequently treated as an ideal gas mixture, whose partition function is given by the standard form

$$Q_{\text{ideal gas}}(\{N_i\}) = \prod_i \frac{q_i^{N_i}}{N_i!}, \tag{1.2}$$

where q_i is the one-particle partition function for species i. This one-particle partition function can be decomposed into translational, rotational, vibrational, and electronic contributions

$$q_i^{\text{fluid}} = q_i^{\text{trans}} q_i^{\text{rot}} q_i^{\text{vib}} q_i^{\text{elec}}, \tag{1.3}$$

as defined in McQuarrie.[111]

Solvated Species

For solvated species, we correct the ideal gas partition function by modifying q_i^{fluid} to include solvation effects via estimates of ΔG_{solv}, a free energy of solvation. Possible approaches for estimatating ΔG_{solv} include computational estimates calculated using a polarizable continuum model (as in our prior work[60]) or obtained using prior experimental data (e.g. Henry's law constants).

Lattice

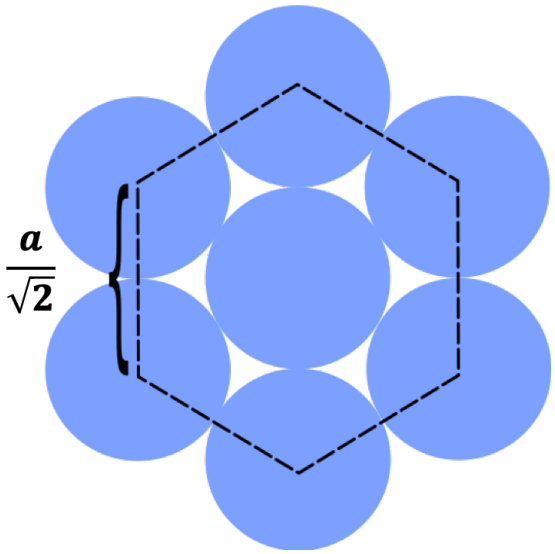

Figure 1.1: Graphical representation of a fcc(111) surface with hexagonal geometry with lattice constant a. Each atom has 6 nearest neighbors

The lattice is characterized by its geometry (e.g. hexagonal, square) and the characteristic area of each site. For example, the (111) surface of an FCC metal has a hexagonal geometry, with each site adjacent to 6 other sites, and the area of each site given by $\frac{\sqrt{3}}{4}a^2$, where a is

the lattice constant of that metal. This is illustrated in figure 1.1. Given a lattice of M sites, occupied by N_i of adsorbate i, and assuming each adsorbate occupies only a single site, the full partition function for the lattice is

$$Q_{\text{latt}}(\{N_i\}) = \prod_i \prod_{n=1}^{N_i} \frac{\left(M - \sum_{j<i} N_j - (n-1)\right)}{n} q_i \tag{1.4}$$

$$= \frac{M!}{(M - \sum_i N_i)!} \prod_i \frac{q_i^{N_i}}{N_i!} \tag{1.5}$$

$$= \frac{M!}{N_*!} \prod_i \frac{q_i^{N_i}}{N_i!}, \tag{1.6}$$

where we have defined $N_* \equiv M - \sum_i s_i N_i$ to be the number of vacant sites on the lattice. The one-particle partition function q_i can be written as

$$q_i^{\text{adsorbate}} = q_i^{\text{hind-trans}} q_i^{\text{hind-rot}} q_i^{\text{vib}} q_i^{\text{elec}}. \tag{1.7}$$

q_i^{vib} and q_i^{elec} have the same form as for the ideal gas, while $q_i^{\text{hind-trans}}$ and $q_i^{\text{hind-rot}}$ correspond to hindered translation and hindered rotation on the surface. There are a number of ways to account for these hindered motions, but herein we shall treat all molecular degrees of freedom as vibrations. Note that Q_{latt} is very similar to $Q_{\text{ideal gas}}$, with the exception of the first term, $\frac{M!}{N_*!}$. This term enforces the indistinguishability of vacant sites, such that $Q(\{N_i = 0\}) = 1$. While this derivation specifically refers to the catalyst surface as a lattice (i.e. fcc(111)), this derivation and resulting code implementation are general and can be used to model any arrangement of catalyst active sites (e.g. metal oxides or zeolites).

1.2.2 Multidentate Binding

The above expressions are standard results utilized in nearly all microkinetic models and are appropriate for describing heterogeneous catalytic reaction networks involving small adsorbates at low coverage. To better account for larger adsorbates, we now extend these results to account for multidentate binding of an adsorbate to the surface.

For a lattice containing adsorbates that bind simultaneously to two or more lattice sites, the partition function depends on the number of possible orientations for such an adsorbate on the lattice. If the lattice sites required to bind a multidentate adsorbate are assigned one at a time, then while the first site can be any of the N_* vacant sites, subsequent sites must be adjacent to the previously assigned site. For any given binding site, within the mean field approximation, the probability that the site is unoccupied and thus counts towards a possible binding geometry is

$$p = \frac{M - N_*}{M}. \tag{1.8}$$

For an adsorbate that occupies multiple sites, given that we have assigned the first site, the number of possible choices for the second site is

$$\sum_{m=1} m \binom{\sigma}{m} p^m (1-p) \quad ^{-m} = \sigma p, \tag{1.9}$$

where σ is the number of nearest neighbors for each lattice site.

In the mean field approximation, the probability p that a given site is free will be the same for all sites. For example, if we are considering the number of orientations available for the second site of a bidentate adsorbate, and we have already assigned N_x sites for other adsor-

bates, then in the mean field approximation, p will be

$$p = \frac{M - N_x - 1}{M}. \tag{1.10}$$

The 1 in the numerator accounts for the site already occupied by the first part of the adsorbate.

For species occupying three or more sites, we can reuse the expression in Eq. 1.9 and replace σ with the number of possible orientations for the third and any subsequent binding site. We define $\sigma_{i,k}$ to be the number of different possible orientations for the kth site of species i, given that all sites $\leq k$ have already been assigned. In general, we can write the partition function as

$$\begin{aligned} Q_{\text{latt}} = \prod_i \prod_{n=1}^{N_i} \Bigg[& q_i \left(\frac{M - \sum_{j<i} s_j N_j - s_i (n-1)}{n} \right) \times \\ & \prod_{k=2}^{s_i} \sigma_{i,k} \left(\frac{M - \sum_{j<i} s_j N_j - s_i (n-1) - k + 1}{M} \right) \Bigg] \end{aligned} \tag{1.11}$$

$$= \frac{M!}{N_*!} \prod_i \left(\frac{\sigma_i q_i}{M^{s_i - 1}} \right)^{N_i} \frac{1}{N_i!}, \tag{1.12}$$

where s_i is the number of sites to which species i binds, $\sigma_{i,k}$ is the number of possible orientations for the kth site of species i, and

$$\sigma_i = \prod_{k=2}^{s_i} \sigma_{i,k} \tag{1.13}$$

is the the "symmetry number" for adsorbate i. Note that in this formalism, $\sigma_{i,2} = \frac{}{2}$ if the adsorbate has end-to-end symmetry, and $\sigma_{i,2} = \sigma$ if it does not. This eliminates double-counting arising from the indistinguishability between orientations of a molecule when it is flipped end-to-end.

Thus, the full partition function for a system comprising a fluid and a lattice can be written

as

$$Q = \frac{M!}{N_*!} \prod_i^{\text{fluid}} \frac{q_i^{N_i}}{N_i!} \prod_j^{\text{adsorbate}} \left(\frac{\sigma_j q_j}{M^{s_j - 1}} \right)^{N_j} \frac{1}{N_j!}. \tag{1.14}$$

1.2.3 Equilibrium and rate constants

Equilibrium constants

Using standard expressions, the equilibrium constant K_{eq} for a fluid phase reaction is

$$K_{\text{eq}}^{\circ} = \frac{\varrho_{\text{C}}/\varrho_{\text{C}}^{\circ}}{\left(\varrho_{\text{A}}/\varrho_{\text{A}}^{\circ}\right)\left(\varrho_{\text{B}}/\varrho_{\text{B}}^{\circ}\right)} = \frac{q_{\text{C}}^{\circ}}{q_{\text{A}}^{\circ} q_{\text{B}}^{\circ}} = \exp\left[-\frac{\Delta G_{\text{rxn}}^{\circ}}{k_B T} \right], \tag{1.15}$$

where q° is the partition function evaluated at the volume corresponding to the reference system concentration. We have also defined the free energy of reaction $\Delta G_{\text{rxn}}^{\circ}$ in a particular choice of reference state such that

$$\Delta G_{\text{rxn}}^{\circ} = \mu_{\text{C}}^{\circ} - \mu_{\text{A}}^{\circ} - \mu_{\text{B}}^{\circ} \tag{1.16}$$

$$\mu_{\text{X}}^{\circ} = -k_B T \ln\left[q_{\text{X}}^{\circ} \right], \tag{1.17}$$

which is the standard definition for the chemical potential of a given species.

The chemical potential of a species in the lattice is easily obtained from Eq. 1.14,

$$\mu_i = -k_B T \ln\left[\frac{\vartheta_*^{s_i} \sigma_i q_i}{\vartheta_i} \right]. \tag{1.18}$$

where ϑ_* is the fraction of empty lattice sites, N_*/M, and ϑ_i is the fraction of lattice sites occupied by species i, N_i/M.

For example, the equilibrium condition for the on-lattice reaction

$$\mathrm{A}* + \mathrm{B}* \longleftrightarrow \mathrm{C}** \tag{1.19}$$

is

$$K_{\mathrm{eq}}^{\circ} = \frac{\vartheta_{\mathrm{C}}}{\vartheta_{\mathrm{A}}\vartheta_{\mathrm{B}}} = \frac{\sigma_{\mathrm{C}} q_{\mathrm{C}}}{\sigma_{\mathrm{A}} q_{\mathrm{A}} \sigma_{\mathrm{B}} q_{\mathrm{B}}} = \exp\left[-\frac{\Delta G_{\mathrm{rxn}}^{\circ}}{k_B T}\right]. \tag{1.20}$$

This is the standard expression for the equilibrium constant for an on-surface reaction with the exception of the σ_{X} terms. In general, $\sigma_{\mathrm{X}} = 1$ for adsorbates occupying only a single site. The free energy of this reaction is

$$\Delta G_{\mathrm{rxn}}^{\circ} = \mu_{\mathrm{C}}^{\circ} - \mu_{\mathrm{A}}^{\circ} - \mu_{\mathrm{B}}^{\circ} \tag{1.21}$$

$$\mu_{\mathrm{X}}^{\circ} = -k_B T \ln\left[\sigma_{\mathrm{X}} q_{\mathrm{X}}\right] \tag{1.22}$$

$$= -k_B T \ln\left[q_{\mathrm{X}}\right] - k_B T \ln\left[\sigma_{\mathrm{X}}\right], \tag{1.23}$$

where the last term in Eq. 1.23 corresponds to the configurational contribution to the free energy.

If the number of sites occupied by the reactants is different from the number of sites occupied by the products, the equilibrium condition changes slightly. For example, for a reaction of the form

$$\mathrm{A}* + \mathrm{B}* \longleftrightarrow \mathrm{C}* + *, \tag{1.24}$$

the equilibrium constant is given by

$$K_{\mathrm{eq}}^{\circ} = \frac{\vartheta_{\mathrm{C}}\vartheta_{*}}{\vartheta_{\mathrm{A}}\vartheta_{\mathrm{B}}} = \frac{\sigma_{\mathrm{C}} q_{\mathrm{C}}}{\sigma_{\mathrm{A}} q_{\mathrm{A}} \sigma_{\mathrm{B}} q_{\mathrm{B}}} = \exp\left[-\frac{\Delta G_{\mathrm{rxn}}^{\circ}}{k_B T}\right]. \tag{1.25}$$

Generalizations of these expressions to other reaction stoichiometries are self-evident.

For an adsorption reaction of the form

$$\mathrm{A}* + * \quad \longleftrightarrow \quad \mathrm{A}*, \tag{1.26}$$

the equilibrium constant is

$$K_{\mathrm{eq}}^{\circ} = \frac{\vartheta_{\mathrm{A}}}{\left(\varrho_{\mathrm{A}}/\varrho_{\mathrm{A}}^{\circ}\right)\vartheta_{*}} = \frac{\sigma_{\mathrm{A}} q_{\mathrm{A}}^{\mathrm{ads}}}{q_{\mathrm{A}}^{\mathrm{fluid},\circ}} = \exp\left[-\frac{\Delta G_{\mathrm{rxn}}^{\circ}}{k_B T}\right] \tag{1.27}$$

where q^{ads} is the partition function for the adsorbate and q^{fluid} is the partition function for the fluid-phase species. The free energy of reaction is

$$\Delta G_{\mathrm{rxn}}^{\circ} = \mu_{\mathrm{A}}^{\mathrm{ads},\circ} - \mu_{\mathrm{A}}^{\mathrm{fluid},\circ}, \tag{1.28}$$

where the free energy of fluids is described by Eq. 1.17 and the free energy of adsorbates is described by Eq. 1.23.

Rate constants

The standard transition state theory rate expression can also be equivalently generalized to account for multidentate adsorption of reactants, products, and transition states. For an on-lattice reaction of the form

$$\mathrm{A}* + \mathrm{B}* \quad \longleftrightarrow \quad \mathrm{AB}^{\ddagger}** \quad \longrightarrow \quad \mathrm{C}**, \tag{1.29}$$

where $AB^{\ddagger}$ is the transition state connecting the reactants A + B to the product C, the rate expression is given by

$$r = k_{\text{for}}\vartheta_{\text{A}}\vartheta_{\text{B}} - k_{\text{rev}}\vartheta_{\text{C}}. \tag{1.30}$$

The transition state theory rate constants are then given by

$$k_{\text{for}} = \frac{k_B T}{h}\frac{\sigma_{\text{AB}^{\ddagger}} q'_{\text{AB}^{\ddagger}}}{\sigma_{\text{A}} q_{\text{A}} \sigma_{\text{B}} q_{\text{B}}} = \frac{k_B T}{h}\exp\left[-\frac{\Delta G^{\ddagger}_{\text{for}}}{k_B T}\right] \tag{1.31}$$

$$k_{\text{rev}} = \frac{k_B T}{h}\frac{\sigma_{\text{AB}^{\ddagger}} q'_{\text{AB}^{\ddagger}}}{\sigma_{\text{C}} q_{\text{C}}} = \frac{k_B T}{h}\exp\left[-\frac{\Delta G^{\ddagger}_{\text{rev}}}{k_B T}\right], \tag{1.32}$$

where $q'_{\text{AB}^{\ddagger}}$ is the partition function for the transition state with the mode perpendicular to the transition state dividing surface removed. $\Delta G^{\ddagger}$ is defined analogously to the previous section, where the transition state is considered to be the product species. The free energy of the transition state is calculated in exactly the same way as the free energy of any other species in the model, except that the imaginary-frequency vibrational mode corresponding to the reaction coordinate is excluded from the species degrees of freedom. These expressions for the rate constant are valid regardless of the number of lattice sites occupied by species A, B, $AB^{\ddagger}$, or C, and are trivially generalized to other reaction stoichiometries.

For adsorption reactions of gas-phase species of the form,

$$\text{A} + * \longleftrightarrow \text{A}*, \tag{1.33}$$

the rate constant is described by collision theory,

$$r = k_{\text{ads}} \varsigma_{\text{A}} \vartheta_{*} - k_{\text{des}} \vartheta_{\text{A}} \tag{1.34}$$

$$k_{\text{ads}} = S_0 N_{\text{av}} A_{\text{site}} \sqrt{\frac{k_B T}{2\pi m_{\text{A}}}} \tag{1.35}$$

$$k_{\text{des}} = \frac{k_{\text{ads}}}{K_{\text{eq}}}, \tag{1.36}$$

where S_0 is the sticking coefficient, N_{av} is Avogadro's number, A_{site} is the area of a single adsorption site on the lattice, and m_{A} is the mass of species A. This expression can be derived both from the kinetic theory of gasses and from transition state theory, in which the transition state is considered to be the gas-phase reactant confined to a two-dimensional box with area A_{site}.

1.3 Mass Transport

Many heterogeneously catalyzed reactions occur in the presence of solvent rather than in the vapor phase. In order to accurately model kinetics of reactions of species in the fluid phase and adsorption/desorption kinetics from the surface, we must account for diffusion and mass transport limitations. Here, we present expressions that are used by Micki to account for diffusion-limited fluid-phase reactions as well adsorption from (or desorption to) the fluid phase.

Fluid Phase Reaction

For a diffusion-controlled reaction in the solution phase of the form

$$\text{A} + \text{B} \longleftrightarrow \text{C}, \tag{1.37}$$

the rate expression is

$$r = k_{\text{for}} \varrho_{\text{A}} \varrho_{\text{B}} - k_{\text{rev}} \varrho_{\text{C}}, \tag{1.38}$$

where

$$k_{\text{for}} = 4\pi DR \tag{1.39}$$

$$k_{\text{rev}} = \frac{k_{\text{for}}}{K_{\text{eq}}}, \tag{1.40}$$

where $D = D_{\text{A}} + D_{\text{B}}$ is the relative diffusion constant between species A and B and $R = R_{\text{A}} + R_{\text{B}}$ is the sum of the effective radii of species A and B [123]. This expression assumes that the reaction is fast and barrierless upon collision of species A with B.

Mass-Transport Limited Adsorption

Adsorption of solution-phase species does not obey collision theory kinetics, as mass transport occurs through much slower diffusive, rather than ballistic, motion. One can assume that the layer of solution that is in direct contact with the lattice surface will be in equilibrium with the surface adsorbates, but adsorption of species from the bulk liquid or desorption of species into the bulk liquid will be much slower and limited by diffusive transport. To model this, we construct an equilibrium-diffusion model for adsorption of solution-phase species. For such a model, the rate constants for adsorption and desorption are

$$k_{\text{ads}} = \frac{D_{\text{A}} A_{\text{site}}}{\vartheta_* L} \tag{1.41}$$

$$k_{\text{des}} = \frac{k_{\text{for}}}{K_{\text{eq}}}, \tag{1.42}$$

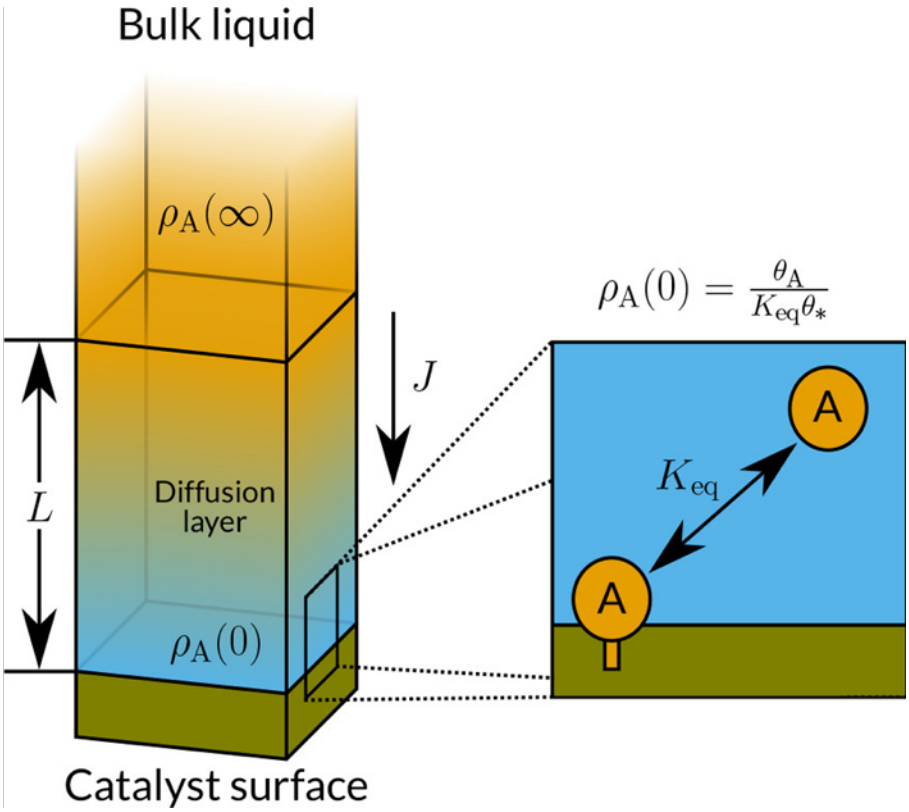

Figure 1.2: Schematic illustration of diffusion-limited adsorption model. Species A is represented by orange, and solvent (i.e. methanol) is represented by blue. L is the diffusive layer thickness, $\varrho_A(\infty)$ is the concentration of species A in the bulk solution, $\varrho_A(0)$ is the concentration of species A in the solution in direct contact with the catalyst surface, J is the net flux of species A towards the catalyst surface, K_{eq} is the equilibrium constant for the adsorption of species A to the catalyst surface, ϑ_A is the coverage of species A on the catalyst surface, and ϑ_* is the fractional number of unoccupied sites on the catalyst surface. Reprinted with permission from ref. 60. Copyright 2018 American Chemical Society.

where D_A is the diffusion constant for species A, A_{site} is the area of a single adsorption site, ϑ_* is the fraction of vacant sites on the lattice, and L is the diffusion length separating the well-mixed bulk liquid from the lattice surface. A detailed derivation of these rate constants is given by Hermes et al.[60]

1.4 Lateral Interactions

The binding energy of a species is highly dependent on the surface coverage. We derive a thermodynamically consistent method to account for the interactions of species on the surface. This interaction is not only limited to intermediates but also affects the energy of transition states. Therefore, we use Brønsted–Evans–Polanyi relations to estimate how coverage-dependant interactions will modify the energy of transition states.

1.4.1 Adsorbate-Adsorbate Interactions

The mean field approximation often fails to accurately represent realistic catalyst surfaces due to the lack of any interactions between adsorbates. It is therefore common to include an effective description of these lateral interactions to supplement the mean field approximation.

Our approach to lateral interactions considers the total (free) energy of the catalyst surface as a many body expansion in terms of the number of adsorbed surface species,

$$G \approx G_0 + \sum_{i}^{\text{adsorbates}} N_i \mu_i^0 + \sum_{i,j}^{\text{adsorbates}} \frac{N_i N_j}{M} E_{ij} + \dots . \tag{1.43}$$

Here, G is the total free energy of the catalyst, G_0 is the free energy of the bare catalyst, μ_i^0 is the chemical potential of species i on the catalyst at infinite dilution (i.e. in the absence of any adsorbate-adsorbate interactions), and E_{ij} is the second-order lateral interaction energy

between species i and j. Note that this expression is not consistent with the partition function described by Eq. 1.14, which contains no energetic cross-terms between adsorbates. To include these cross-terms in the partition function, we introduce corresponding terms in the many body expansion of the free energy,

$$q_{ij\ldots} = \exp\left[-\frac{E_{ij\ldots}}{k_B T}\right]. \tag{1.44}$$

This allows us to write the partition function as

$$Q = \frac{M!}{N_*!}\left(\prod_i^{\text{fluid}} \frac{q_i^{N_i}}{N_i!}\right)\left(\prod_i^{\text{adsorbate}} \left(\frac{\sigma_i q_i}{M^{s_i-1}}\right)^{N_i} \frac{1}{N_i!}\right)\left(\prod_{i,j}^{\text{adsorbate}} q_{ij}^{N_i N_j/M}\right)\ldots \tag{1.45}$$

From this, we can obtain the chemical potential for each species,

$$\mu_i = -k_B T \frac{d\ln Q}{dN_i} = -k_B T \ln\left(\frac{\vartheta_*^{s_i}\sigma_i q_i}{\vartheta_i}\right) + 2\vartheta_i E_{ii} + \sum_{j\neq i}^{\text{adsorbates}} \vartheta_j E_{ij} + \ldots, \tag{1.46}$$

where we have defined $\vartheta_i \equiv N_i/M$. This expression is consistent with Eq. 1.43, as the chemical potential is also defined as

$$\mu_i = \frac{dG}{dN_i} = \mu_i^0 + 2\vartheta_i E_{ii} + \sum_{j\neq i}^{\text{adsorbates}} \vartheta_j E_{ij} + \ldots, \tag{1.47}$$

where we can see that

$$\mu_i^0 = -k_B T \ln\left(\frac{\vartheta_*^{s_i}\sigma_i q_i}{\vartheta_i}\right). \tag{1.48}$$

One important implication of this result is that lateral interactions must be symmetric to

ensure thermodynamic consistency. For example, if species i is destabilized by species j,

$$E_i = E_i^0 + \vartheta_j E_{ij}, \tag{1.49}$$

then species j must also be destabilized by species i,

$$E_j = E_j^0 + \vartheta_i E_{ij}. \tag{1.50}$$

Note that this relation is often violated in other (ad hoc) treatments of lateral interactions. In practice, only a few species will typically dominate the bulk of the catalyst surface, so binding energy dependence on the coverage of minority species can be ignored.

1.4.2 Coverage-dependent transition state energies

These coverage-dependent interaction energies, E_{ij}, can be obtained from a series of calculations at varying coverages of the coadsorbates. However, this approach is often not feasible for transition states due to the computational effort involved with the optimization of saddle points and the large number of calculations that must be performed to calculate lateral interaction energies. An alternative approach is to determine the lateral interaction energies of transition states using the Brønsted-Evans-Polanyi (BEP) principle to estimate the influence of lateral interactions of the transition state from the lateral interactions of the minima it connects. Using standard linear free energy relationship, the free energy barrier of a class of similar reactions is related to the free energy of the reaction,

$$\Delta G^{\ddagger} = \alpha \Delta G + \beta, \tag{1.51}$$

where $\Delta G^{\ddagger}$ is the reaction activation free energy, α is a parameter that characterizes the lateness of the reaction, and β is the activation free energy corresponding to a thermoneutral reaction.[115,97,30,14] If α is known, it can be used to approximate the change in free energy of the transition state due to lateral interactions as a linear combination of the reactant and product lateral interactions,

$$\Delta G^{\ddagger} \approx \Delta E^{\ddagger} = (1-\alpha)\Delta E_R + \alpha \Delta E_P, \tag{1.52}$$

where ΔE_i is the correction to the energy of species i, including lateral interactions.

We estimate α by the forward and reverse activation free energy barriers,

$$\alpha \approx \frac{\Delta G^{\ddagger}_{\text{for}}}{\Delta G^{\ddagger}_{\text{for}} + \Delta G^{\ddagger}_{\text{rev}}}. \tag{1.53}$$

where $\Delta G^{\ddagger}$ is the forward or reverse energy barrier at zero coverage.

If a species includes a constant correction to the free energy (such as adsorbed CO to match experimental values), Equations 1.52 and 1.53 include those corrections.

1.5 Micki

Micki incorporates the above formalism into an efficient, user-friendly, general purpose mean-field microkinetic modeling code. The code is modular, Python-based, and object oriented, employing paradigms that are familiar to chemists (Gas, Adsorbate, Reaction...). Because Micki represents reaction rate expressions symbolically, it is straightforward to introduce lateral interactions and/or reaction parameters of arbitrary functional form. These symbolic expressions are passed to Fortran, where the model is efficiently solved. This allows for sensitivity analysis and/or model optimization to prior experimental observations. The remainder of this section outlines the required input, the generated output, and describes the various reactor

types that can be modeled using Micki. The examples employed in this section correspond to the water-gas shift (WGS) reaction, which is analyzed in more detail in a subsequent section.

1.5.1 Input file

Micki is primarily intended for first-principles microkinetic modeling, and as such expects the user to have prepared electronic structure calculations and vibrational frequency analysis for all minima and transition states. Currently, Micki is only capable of reading the `vasprun.xml` or `OUTCAR` files generated by `VASP`. However, since Micki utilizes the Python environment ASE[90] to read and store the results of electronic structure theory calculations, Micki can trivially be extended to any code supported by ASE.

```
#!/usr/bin/env python

from micki import Adsorbate, Gas
from ase.io import read
from ase.db import connect

sp = {} #create dictionary of all species
sp['co_g'] = Gas('co_g/freq/vasprun.xml',
                 label='co_g',
                 freqs=None,
                 symm=1,
                 spin=0.,
                 eref=None,
                 rhoref=1.,
                 dE=0.)
sp['h2o_g'] = Gas('h2o_g/freq/vasprun.xml',
                  label='h2o_g',
                  symm=2)

sp['slab'] = Adsorbate(read('pt/vasprun.xml'),
                       label='slab',
                       freqs=[],
                       ts=False,
                       spin=0.,
                       sites=[],
                       lattice=None,
                       eref=None,
                       dE=0.,
                       symm=1)
sp['co'] = Adsorbate('co/freq/vasprun.xml',
                     label='co',
                     freqs=None,
                     ts=False,
                     spin=0.,
                     sites=[sp['slab']],
                     lattice=None,
                     eref=None,
                     dE=0.,
                     symm=1)
sp['cooh'] = Adsorbate('cooh/freq/vasprun.xml',
                       label='cooh',
                       sites=[sp['slab']])

sp['ho-h'] = Adsorbate('ho-h/freq/vasprun.xml',
                       label='ho-h',
                       sites=[sp['slab'], sp['slab']],
                       symm=2,
                       ts=True)

with connect('my_micki_db.json') as con:
    for name, species in sp.items():
        species.save_to_db(con)
```

Listing 1: An example of how to read in the output files from VASP frequency calculations.

Listing 1 illustrates how to read in the output from `VASP` frequency calculations. Line 15 illustrates all options available to the `Gas` class, which calculates the free energy of a species under the ideal gas approximation. For lines 16 through 18, arguments corresponding to the default settings have been omitted. Rather than explicitly passing the vibrational frequencies to the `Gas` class, these vibrational frequencies are automatically determined by diagonalizing the Hessian matrix contained within the `vasprun.xml` output file.

Beginning on line 29, species corresponding to adsorbates on the surface are read, starting with the bare slab itself. The `Adsorbate` class treats all adsorbate degrees of freedom under the harmonic oscillator approximation. For the bare slab, we use the `read` method from ASE and explicitly pass an empty list of frequencies, as we do not consider the motion of metal atoms in our vibrational frequency analysis. The `Adsorbate` class takes an additional argument, `sites`, which is used to ensure proper site balancing when writing reactions by specifying the object(s) corresponding to the bare site(s) to which the adsorbate is bound. The ”sites” argument is also the means by which the user can specify that an adsorbate exhibits multidentate binding, or to distinguish between different kinds of adsorbates sites (e.g. step vs. terrace). For lines 30 through 39, all arguments for a species in the `Adsorbate` class, including defaults, are explicitly shown. For lines 39 through 42, all default arguments have been omitted. Line 48 shows an example of reading the transition states frequencies; other than the `ts=True` argument, this is identical to the case of reaction intermediates.

On lines 50 through 52, the newly created thermodynamic objects are saved to an ASE database file. The database file can be read in with a later script that runs the microkinetic model. With the exception of the `dE` argument (an optional empirical shift to the binding energy), all other settings are saved in the `data` field of the ASE database. Using an ASE database to store the species of a microkinetic model not only speeds up the process of running the microkinetic model itself, but also allows one to quickly inspect and analyze the

species using normal ASE utilities.

```
1   #!/usr/bin/env python
2
3   from micki.db import read_from_db
4   from micki import Reaction, Model
5   from ase.units import m, _k, _Nav
6
7   sp = read_from_db('my_micki_db.json', eref=['slab', 'co_g', 'h2o_g', 'h2_g'])
8
9   sp['co'].dE = 0.09496182099234107  # Shift to match experiment binding enthalpy
10  sp['oh'].dE = -0.217133501  # Shift to match experimental TOFs
11
12  sp['co'].lateral = 2*0.784423808 * sp['co'].symbol
13
14  sp['o'].lateral = 1.147079243 * sp['co'].symbol + 2*1.11913902 * sp['o'].symbol
15  sp['co'].lateral += 1.147079243 * sp['o'].symbol
16
17  sp['h'].lateral = 0.237728186 * sp['co'].symbol
18  sp['co'].lateral += 0.237728186 * sp['h'].symbol
```

Listing 2: An example script showing how to read in the database and set lateral interaction parameters.

Listing 2 illustrates the beginning of a new script in which the previously-created database is read. On line 7, a dictionary of thermodynamic objects is recreated from the database, and the energies of all species are shifted so as to set the energies of the defined species to 0 while maintaining all relative energies. The `eref` argument must have as many species as there are unique elements and every element must appear at least once in this set of species. If `eref` is passed the elemental form of each atom (e.g. graphite for carbon, dioxygen gas for oxygen, etc.), then the energy of each species in `sp` is its *formation* energy. `eref` is also necessary to accurately account for the correct number of catalyst atoms on both sides of a chemical equation for reactions that involve multidentate binding.

On lines 9 and 10, the energy of adsorbed CO and OH are shifted to match experimental results. Starting on line 12, the lateral interaction energies between adsorbates are defined. Each

thermodynamic object has a corresponding `symbol` attribute, which is a `sympy` symbol object corresponding to the coverage of that species in the model. Lateral interactions are defined as symbolic expressions which modulate the energy according to the instantaneous coverage of the species in the model. Here, lateral interactions are taken as linear functions of species coverages, but in general this can be any well-behaved expression. Thermodynamic balance is ensured by making all lateral interactions symmetric between species (for example, compare lines 17 and 18).

```
1  rxns = {'co_ads': Reaction(sp['co_g'],
2                             sp['co'],
3                             method='STICK'),
4          'ho-h': Reaction(sp['h2o'],
5                             sp['oh'] + sp['h'],
6                             ts=sp['ho-h']),
7          'o-h-oh': Reaction(2*sp['oh'],
8                             sp['o'] + sp['h2o'],
9                             method='DIEQUIL'),
10         'oco-h-oh': Reaction(sp['cooh'] + sp['oh'],
11                            sp['co2_g'] + sp['h2o'],
12                            method='EQUIL')}
13
14 Asite = np.sqrt(3) * 3.8966**2 / (4 * m**2)  # area per site, in m^2
15 T = 548  # temperature, in Kelvin
16 atm2molar = 101325 / _k / T / _Nav / 1000.
17
18 model = Model(T, Asite, reactor='CSTR')
19 model.lattice = {sp['slab']: {sp['slab']: 6}}
20 model.add_reactions(rxns)
21 model.set_fixed(['co_g', 'h2o_g', 'h2_g', 'co2_g'])
22
23 U0 = {'co_g': 0.145 * atm2molar,
24       'h2o_g': 0.208 * atm2molar}
25
26 model.set_initial_conditions(U0)
27 t1, U1, r1 = model.find_steady_state()
```

Listing 3: An example script illustrating how to set up and run a simple CSTR reactor model.

Listing 3 contains the second half of the script that began with listing 2. It starts by defining reactions considered in this model. The rate of adsorption reactions are approximated using collision theory, which is selected with the `method='STICK'` flag. The rates of reactions with a known transition state are approximated using transition state theory, which is selected by passing the thermodynamic object corresponding to the transition state to the `Reaction` class. For (barrierless) reactions that do not have a transition state, the argument `method='EQUIL'` will cause Micki to approximate the rate constant in the exothermic direction as $(\beta h)^{-1}$, which is equivalent to transition state theory with an activation energy barrier of zero. For some reactions, however, lateral interactions may cause the reaction to oscillate between exothermic and endothermic depending on reaction conditions. This can cause unphysically fast rate constants. In these cases `method='DIEQUIL'` can be used, which estimates the rate constants as

$$k_{for} = \frac{1}{\beta h}\left(\frac{K_{eq}}{1+K_{eq}}\right)$$
$$k_{rev} = \frac{1}{\beta h}\left(\frac{1}{1+K_{eq}}\right).$$

When $K_{eq} \ll 1$ or $K_{eq} \gg 1$, this expression reduces to the same approximation as used with `method='EQUIL'`.

On lines 14 and 15, some model parameters are defined. The area per adsorption site is necessary to determine the rate of adsorption under collision theory, while the temperature is needed to calculate equilibrium constants and rate constants. The model is created on line 18. On line 19, the geometry of the catalyst surface is defined by specifying the number of nearest neighbors for each kind of site included in the model. The first `sp['slab']` term identifies the site whose neighbors we are specifying, while the second `sp['slab']` indicates the type of sites that are neighboring the initial site. Since this example considers a simple FCC(111) surface, there is only one type of site, each of which has 6 nearest neighbors. The reactions are

added to the model on line 20, and the concentrations of gas-phase species are fixed on line 21 in order to model a simplified continuous stirred tank reactor (CSTR).

The initial conditions of the reactor are defined on line 23. Any species whose initial concentration is not specified are assumed to have an initial concentration of 0, with the exception of empty lattice sites, which is defined such that the sum of all adsorbates and empty sites is equal to 1. Upon setting the initial conditions in line 26, Micki sets up, compiles, and imports the Fortran module for solving the differential equations. The `find_steady_state` method called on line 27 then runs this code in order to find the steady state concentrations. It returns three results, `t1`, `U1`, and `r1`, corresponding to the approximate time to reach steady state, the steady state concentrations (in M, fluid phase) or coverages (fractional, adsorbates), and the steady state rates, respectively.

In addition to the `find_steady_state` method, Micki provides a `solve` method for explicitly integrating the microkinetic model for a specified time range. This method returns a list of concentrations and reaction rates at the requested number of time points over the requested time range. Given these converged results, Micki can perform a variety of analyses to probe the reaction network.

1.5.2 Sensitivity Analysis

Sensitivity analysis provides an important tool to identify model parameters that are most important to a particular property of interest, such as turnover frequency or selectivity.[15,170,16] The degree of rate control is a metric originally formulated by Campbell that measures the sensitivity of some output parameter to the rate constants of a particular reaction step,

$$\chi_{\mathrm{RC},i} = \frac{k_i}{P}\left.\frac{dP}{dk_i}\right|_{k_{j\neq i},K_{eq}}, \tag{1.54}$$

where P is some output of the model such as a turnover frequency, and k_i refers to both the forwards and reverse rate constants for step i. Similarly, the degree of thermodynamic rate control measures the sensitivity of some model output to the energy of a particular reaction intermediate,

$$\chi_{\mathrm{TRC},n} = -\frac{1}{\beta P}\left.\frac{dP}{dG_n^\circ}\right|_{G^\circ_{m\neq n},G_i^{\ddagger\circ}}, \tag{1.55}$$

where G_n° is the free energy of species n, and $G_i^{\ddagger\circ}$ refers to the free energy of the transition state corresponding to reaction step i.

Micki allows the user to explicitly perturb the binding energies of reaction intermediates and transition states. Furthermore, Micki provides an interface for scaling the rates of individual reaction steps and the energy, entropy, or free energy of intermediates and transition states by a constant factor. This flexibility allows the user to quickly and easily perform the numerical derivatives necessary to calculates χ_{RC} or χ_{TRC}.

```
    chi_rc = {}
    rmid = r1['co_ads']  # as a proxy for CO2 production
    scale = 0.001
    for rname, rxn in rxns.items():
        rxn.set_scale('kfor', 1 - scale)
        rxn.set_scale('krev', 1 - scale)
        model.set_initial_conditions(U1)
        t2, U2, r2 = model.find_steady_state()
        rlow = r2['co_ads']

    rxn.set_scale('kfor', 1 + scale)
    rxn.set_scale('krev', 1 + scale)
    model.set_initial_conditions(U1)
    t3, U3, r3 = model.find_steady_state()
    rhigh = r3['co_ads']

    rxn.set_scale('kfor', 1)
    rxn.set_scale('krev', 1)

    chi_rc[rname] = (rhigh - rlow) / (2 * scale * rmid)
```

Listing 4: An example script illustrating how to calculate Campbell's degree of rate control. This method is included in the module analysis.py. We use adsorption of CO as a proxy for the production of CO2. In our reaction network, all net adsorption of CO must necessarily result in formation of CO2. Due to the presence of multiple CO2-producing elementary steps, it is easier to measure the net production of CO2 by inspecting the net adsorption of CO.

```
    from ase.units import kB
    from micki import Adsorbate

    chi_trc = {}
    rmid = r1['co_ads']  # as a proxy for CO2 production
    scale = 0.001
    dE = scale * kB * T
    for name, species in sp.items()
    # only calculate chi_trc for adsorbed minima
    if (not isinstance(species, Adsorbate)
    or species.ts
    or name == 'slab'):
    continue

    species.dE -= dE
    for _, rxn in rxns.items():
    rxn.update(T=T, Asite=Asite, force=True)
    model.set_initial_conditions(U1)
    t2, U2, r2 = model.find_steady_state()
    rlow = r2['co_ads']

    species.dE += 2*dE
    for _, rxn in rxns.items():
    rxn.update(T=T, Asite=Asite, force=True)
    model.set_initial_conditions(U1)
    t3, U3, r3 = model.find_steady_state()
    rhigh = r3['co_ads']

    species.dE -= dE

    chi_trc[name] = (rlow - rhigh) / (rmid * scale)
```

Listing 5: An example script illustrating how to calculate Campbell's degree of thermodynamic rate control. This method is included in the module analysis.py.

As an example, consider the target property of interest to be the rate of formation of CO_2 under steady state conditions in the water–gas shift reaction we have used as an example. The degree of rate control for each reaction can be easily calculated, as illustrated in listing 4. Similarly, a script illustrating how to calculate the degree of thermodynamic rate control for each species in the model is illustrated in listing 5.

Note that as implemented in listing 5, the degree of thermodynamic rate control that is calculated is not identical to its original definition as formulated by Campbell.[170] Specifically, Micki explicitly accounts for the correlation between the energy of a transition state with its adjoining minima through an approximate Brønsted–Evans–Polanyi-type relationship as outlined above. Consequently, perturbations to adsorbate energies will also affect the binding energy of transition states, and thereby the forward and reverse rates of reactions involving that adsorbate.

```
    rate_order = {}
    rmid = r1['co_ads']  # as a proxy for CO2 production
    drho = 5e-5
    for name in ['co_g', 'h2o_g']:
    species = sp[name]
    rhomid = U0[name]

    U0_new = U0.copy()
    U0_new[name] -= drho
    model.set_initial_conditions(U0_new)
    t2, U2, r2 = model.find_steady_state()
    rlow = r2['co_ads']

    U0_new[name] += 2*drho
    model.set_initial_conditions(U0_new)
    t3, U3, r3 = model.find_steady_state()
    rhigh = r3['co_ads']

    rate_order[name] = rhomid * (rhigh - rlow) / (2 * drho * rmid)
```

Listing 6: An example script illustrating how to calculate the rate order of reactants. This method is included in the module analysis.py.

```
    from ase.units import kB

    rmid = r1['co_ads']  # as a proxy for CO2 production
    dT = 0.01

    model.T = T - dT
    model.set_initial_conditions(U1)
    t2, U2, r2 = model.find_steady_state()
    rlow = r2['co_ads']

    model.T = T + dT
    model.set_initial_conditions(U1)
    t3, U3, r3 = model.find_steady_state()
    rhigh = r3['co_ads']

    model.T = T
    Ea = kB * T**2 * (rhigh - rlow) / (2 * rmid * dT)
```

Listing 7: An example script illustrating how to calculate the effective activation energy of a model. This method is included in the module analysis.py.

It is also simple to calculate the rate order of a particular reactant by numerically perturbing its initial concentration. An example script illustrating how this can be done is presented in listing 6. As a final example, the effective activation energy for the formation of a particular product can be calculated by numerically perturbing the temperature of the model, as illustrated in listing 7.

1.5.3 Performance

Given the high-performance SUNDIALS differential equation solver, this whole array of sensitivity analysis can be accomplished very rapidly. For example, the water gas shift example (presented below) contains 11 reactions and is solved using a complex plug-flow reactor in less than 6 s on a single core. A more extensive reaction example is given by the esterification of 1-propanol to methyl propionate on a Pd(111) surface.[60] This model, with 47 reactions and 75

species (including transition states), is solved in only 12 s; including full sensitivity analysis for all 75 species, the time increases to approximately 10 min.

1.5.4 Reactor Models

Micki is fully scriptable and as such can be used to simulate a wide variety of reaction conditions and reactor models. Batch reactors can be simulated by analyzing initial rates and concentration as the reaction approaches equilibrium. A (simplified) continuous stir tank reactor (CSTR) is simulated by fixing the concentrations of a subset of reactants/products and then solving the resulting system to steady-state, effectively modeling the reaction at infinitely fast flow. A CSTR is the most common reactor method simulated with microkinetic models.

It is also possible to simulate a steady-state plug flow reactor (PFR). A steady-state PFR is assumed to be perfectly mixed radially across the plug and (at steady-state) does not change concentrations in time, but the concentrations do evolve along the length of the reactor. Under such assumptions, we can reduce the set of two-dimensional PFR differential equations involving both time and space to a one dimensional system of differential algebraic equations (DAEs) involving the space-time along the reactor tube.[43] Fluid phase species evolve over the length of the reactor by obeying the PFR mass balance equations given by

$$\frac{\partial([C_i]A)}{\partial t} = -Q\frac{\partial[C_i]}{\partial z} + f(\{[C],\vartheta_C\})A \tag{1.56}$$

$$\frac{\partial[C_i]}{\partial t} = -\frac{Q}{A}\frac{\partial[C_i]}{\partial z} + f(\{[C],\vartheta_C\}) \tag{1.57}$$

where Q is the flow rate, A is the cross sectional area of the reactor column and $f(\{[C],\vartheta_C\})$ represents the rates of reaction processes that form and consume fluid-phase species C_i. The first term on the right hand side represents the flow of C_i out of a region of the reactor, while

the second term represents the generation / consumption of the species due to reactions.

At steady state, the left hand side of the equation is zero and therefore

$$\frac{Q}{A}\frac{d[C_i]}{dz} = f(\{[C], \vartheta_C\}). \tag{1.58}$$

Changing variables, dz can be transformed into the space-time $d\tau$,

$$d\tau = \frac{dV}{Q} = \frac{Adz}{Q}, \tag{1.59}$$

yielding

$$\frac{d[C]}{d\tau} = f(\{[C], \vartheta_C\}). \tag{1.60}$$

For a surface species, ϑ_{C_i}, the above derivation is the same, however since surface adsorbed species are not subject to flow equation 1.58 simplifies to

$$0 = g(\{[C], \vartheta_C\}) \tag{1.61}$$

where $g(\{[C], \vartheta_C\})$ represent the possible rates that form and consume surface species C.

The space-time, τ, depends on the number of active sites and the flow rate,

$$\tau = \frac{V}{Q}, \tag{1.62}$$

where Q is the volumetric flow rate. We can express the volume of the reactor as

$$V = \frac{M}{\varsigma_*} \tag{1.63}$$

where M is the number of active sites and ς_* is the concentration of active sites. This yields a

total integration time of

$$\tau = \frac{M}{Q\varrho_*}. \tag{1.64}$$

The form of Eq. 1.60 is identical to that of a CSTR, but involving space-time along the reactor (rather than time). Nonetheless, the equation can be numerically integrated using an identical approach. The initial starting coverages are provided from the CSTR surface concentrations at the input fluid concentrations. We calculate the evolution of the PFR along the reactor length by numerical integration of the DAEs by $\Delta\tau$ (perhaps on a non-uniform grid), as show in figure 1.3. Numerical integration is performed using the SUNDIALS package.[65]

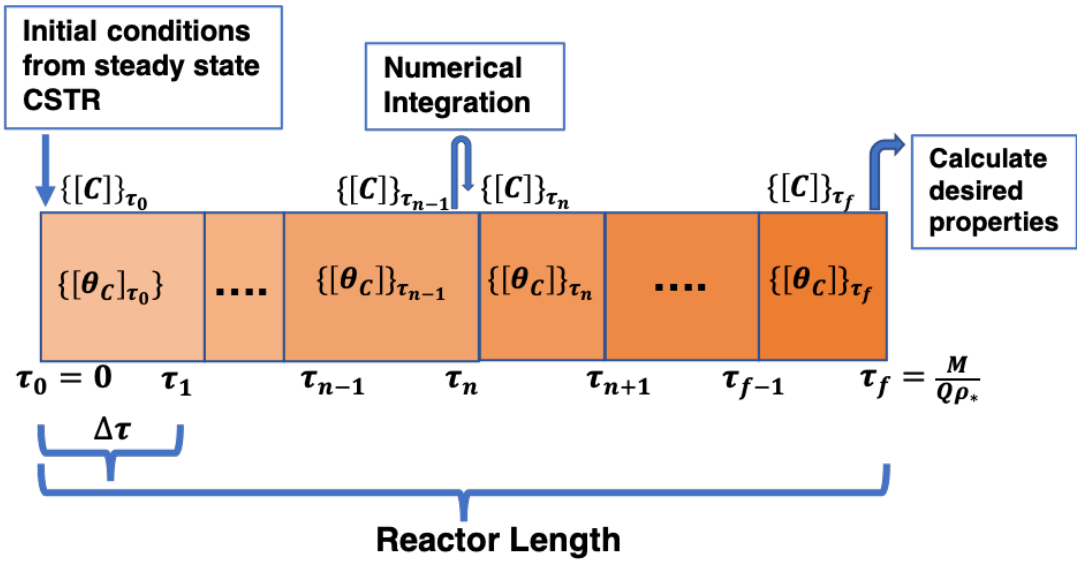

Figure 1.3: Graphical representation of a PFR. A PFR can be conceptualized as a series of stacked CSTRs with evolving fluid-phase concentrations. We solve for the evolution of species along the length of the reactor by numerically integrating Eqs. 1.60 and 1.61.

The overall conversion of reactants into products is determined by species emerging from the end of the PFR, i.e. the concentration of the fluid-phase species at τ_f. The following section will utilize Micki's description of a PFR to model the Water-Gas-Shift reaction on Pt(111).

1.5.5 Extensions of Micki

The primary focus of Micki is on first-principles microkinetic model generation. An intrinsic limitation of this first-principles approach is that it requires the identification and enumeration of all plausible elementary steps, along with calculations of the associated reactants, transitions states, and products. In order to circumvent the need to manually enumerate all possible reaction pathways, the modular nature of Micki would allow for straightforward integration with existing automated reaction pathway generators.[40]

Nonetheless, extension of this purely first-principles approach to extremely large and/or complex reaction networks will likely be hindered by the computational burden of these numerious species. To mitigate this challenge, it should be possible to extend Micki to incorporate additional semi-empirical approaches (e.g. group additivity, scaling relations) or experimental data (e.g. measured binding energies) to supplement *ab initio* data by providing additional arguments to the constructors for the `Species` or `Reaction` objects.

1.6 Water-gas shift reaction

We use Micki to build a microkinetic model for the water-gas shift (WGS) reaction catalyzed by Pt(111) in a plug-flow reactor. Grabow et al. previously investigated this reaction under 21 different experimental reaction conditions, while also developing a parallel (first-principles) microkinetic model whose parameters were subsequently optimized to better match the corresponding experimental results.[46] Below, using Micki, we show that the use of self-consistent lateral interactions, coverage-dependent transition state energies, and dispersion-corrected DFT yields a microkinetic model that yields qualitatively comparable results even without parameter optimization, and quantitative results with fewer and smaller adjustments (within accepted DFT error) as compared with previous first-principles microkinetic models.

Briefly, Grabow et. al studied the WGS reaction over a 3 wt% Pt/Al_2O_3 catalyst and 21 different temperatures and/or partial pressures. Using DFT, they parameterized a microkinetic model whose parameters were subsequently refined to reproduce the experimentally-observed TOF and to elucidate the dominant reaction mechanism. Notably, they reduced the binding energy of key surface intermediates OH* and COOH* by 1.09 and 0.9 eV, respectively. We note that they hypothesize one reason these binding energies must be changed so significantly is that OH* and COOH* may be bound to step sites or defects (although our analysis did not find evidence of this). They also independently fit the transition state energies by modifying the lateness of the transition state via a parameter ω. ω is conceptually analogous to our α parameter, but the latter is calculated self-consistently based on the reactant and product energetics via a BEP relationships (rather than as an independent parameter). They also account for CO coverage effects of CO via coverage-dependent binding energies that depend exponentially on the CO coverage (as opposed to the linear dependence that we use as described above). A summary of their optimized parameters optimized can be found in Grabow et al.[46] All subsequent comparisons are for Grabow et al.'s condition 7, T=548 K, y(CO)=0.145, $y(H_2O)$=0.208.

We consider only the reactions shown in Table 1.1. Grabow et al. also consider additional reactions involving formyl and formate, but found that they do not contribute to the overall activity of the catalyst. Although we initially included them in our reaction network, we also found that these species do not contribute to the reaction flux and thus removed them from the reaction network for simplicity. Additionally, we assume that any CO_2 formed desorbs from the catalyst immediately, ignoring the presence of any physisorbed CO_2 intermediate; we validated that at reaction temperatures, CO_2 is weakly bound and does not appreciably accumulate on the surface.

1.6.1 Methods

All calculations were performed in VASP with the PBE-D3(ABC) dispersion-corrected exchange-correlation functional and a plane wave basis set.[85,86,83,84,135,136,116,10,87] The catalyst surface was represented by a 3x3 primitive Pt(111) surface with four layers. The bottom two layers of the slab were fixed to the geometry of the bulk crystal as determined by PBE-D3(ABC), while the top two layers and adsorbates were relaxed.[116] All calculations used a 450 eV plane-wave cutoff with second-order Methfessel-Paxton smearing with a width of 0.05 eV.[113] The Brillouin zone was sampled by a 3x3x1 Monkhorst-Pack k-point mesh for all calculations involving the catalyst surface. Gas-phase species were calculated in large orthorhombic unit cells with side length at least 20 Å, and the Brillouin zone was sampled only at the Γ point.[131] Geometries were optimized until all forces were less than 0.005 eV $Å^{-1}$. The vibrational frequencies of adsorbates were determined by diagonalizing the partial Hessian comprising only adsorbate degrees of freedom.

The translational and rotational degrees of freedom of gas-phase species were treated under the ideal gas approximation and the rigid rotor approximation, respectively. Vibrational degrees of freedom were treated under the harmonic oscillator approximation. All adsorbate degrees of freedom were considered to be vibrational in nature.

The lateral interactions of all adsorbates with CO were considered, as well as the lateral self-interactions of O.

1.6.2 Optimization

In addition to a purely first-principles microkinetic model, we also considered a model where several crucial model parameters were slightly optimized in order to quantitatively reproduce experimental results. Prior to such such refinement, CO, COOH, H and OH all had thermo-

dynamic degrees of rate control above 0.25 while H_2O and O had thermodynamic degrees of rate control below 0.05. As such, we chose to modify only the binding energies of the first four species (CO, H, COOH and OH). The binding energy of CO and H on Pt(111) has been measured experimentally; therefore, we modified the binding energy of adsorbed CO and the energy of adsorbed H by 0.095 and 0.118 eV, respectively, to match the experimental binding enthalpy.[162] Since the binding energies of OH and COOH are not known experimentally, we treated their binding energies as free parameters. These parameters were fit by optimizing the TOF across all experimental conditions using a BFGS optimizer as implemented in SciPy.[73] The optimized binding energies of OH and COOH were modified by -0.217 and -0.052 eV, respectively. Note that, in contrast to Grabow et al., no transition state energies were fit explicitly. Rather, these binding energy modifications are propagated self-consistently to the transition state energies through the α parameter. All four energy modifications are modest and well within accepted errors of DFT/GGA, and are significantly smaller (and fewer in number) than those employed by Grabow et al. to match the same data set.

1.6.3 Results

In general, the underlying DFT data agrees fairly well with the prior results of Grabow et al., despite the methodological differences (dispersion-corrected PBE-D3(ABC) functional vs the non-dispersion-corrected PW91 functional; see Table 1.1). These differences occur primarily in reactions involving adsorbed O and gas-phase CO_2. We also see more substantial differences in the steady-state enthalpies, presumably due to a combination of how the models are parameterized/optimized to experiment and due to differing treatments of CO coverage effects. We find a steady state coverage of CO of 43% while Grabow et al. see coverages ranging from 65 to 69% for the various conditions. Note that both models also account for coverage effects differently. Our model uses a linear interpolation of coverage effects based on DFT calcula-

Table 1.1: Reaction enthalpies and enthalpies of activation for all reactions considered in this model. All enthalpies correspond to the steady-state catalyst coverage (including lateral interactions) observed for the beginning of the PFR reactor in condition 7 and includes all parameter optimization. In parenthesis are un-optimized zero coverage reaction potential energies and potential energies of activation at zero kelvin. Includes zero point energy. All energies are in eV.

	Grabow et. al.		This work	
Reaction	ΔH_{ss} (ΔE_0)	$\Delta H_{ss}^{\ddagger}$ ($\Delta E_0^{\ddagger}$)	ΔH_{ss} (ΔE_0)	$\Delta H_{ss}^{\ddagger}$ ($\Delta E_0^{\ddagger}$)
$H_2O_{(g)} + * \leftrightarrow H_2O*$	-0.19 (-0.19)		-0.25 (-0.37)	
$CO_{(g)} + * \leftrightarrow CO*$	-1.08 (-1.78)		-0.92 (-1.83)	
$H_{2(g)} + {}_2* \leftrightarrow 2\,H*$	-0.05 (-0.84)		-0.53 (-0.94)	
$H_2O* + * \leftrightarrow OH* + H*$	0.21 (0.52)	0.48 (0.75)	0.66 (0.60)	0.82 (0.82)
$OH* + * \leftrightarrow O* + H*$	2.76 (0.15)	2.76 (0.97)	0.76 (-0.16)	1.36 (0.90)
$2\,OH* \leftrightarrow O* + H_2O*$	2.55 (-0.37)	2.55 (0.00)	0.09 (-0.76)	0.00 (0.00)
$CO* + O* \leftrightarrow CO_{2(g)} + {}_2*$	-2.15 (-0.65)	0.98 (0.98)	-1.61 (-0.04)	0.48 (1.10)
$CO* + OH* \leftrightarrow COOH* + *$	0.10 (-0.32)	0.46 (0.46)	-0.39 (-0.35)	0.18 (0.30)
$COOH* + * \leftrightarrow CO_{2(g)} + H*$	0.51 (-0.18)	0.69 (0.59)	-0.47 (0.15)	0.32 (0.54)
$COOH* + O* \leftrightarrow CO_{2(g)} + OH*$	-2.25 (-0.33)	0.00 (0.23)	-1.22 (0.30)	0.00 (0.33)
$COOH* + OH* \leftrightarrow CO_{2(g)} + H_2O*$	0.30 (-0.70)	0.29 (0.12)	-1.13 (-0.45)	0.00 (0.00)

tions while Grabow et al. parameterize an exponential functional form.

Despite the differences between the two models due to differing input energetics, model assumptions, and optimization strategies, both models predict the same dominant reaction pathway, reproduce TOFs across a range of conditions and accurately predict rate orders and activation energies. Additionally, both models indicate the same rate limiting behavior (using Campbell's degree of rate control).[15]

The dominant reaction pathway begins by adsorbing CO(g) and H_2O(g). Subsequently H_2O* splits to form O* and OH*. OH* then reacts with CO* to form COOH*, which de-

composes to evolve CO_2(g) and and form H*. Surface H* then recombines to form H_2(g). We find that essentially 100% of the COOH* undergoes decomposition vs. oxygen- or hydroxyl-assisted hydrogen abstraction. In contrast, Grabow et al. find that only 87 % of COOH* undergoes the decomposition reaction.

We also analyzed the results of the microkinetic model without further refinement vs. experiment. We find that while the predicted TOF is approximately two orders of magnitude too low across all conditions, the mechanism remains unchanged. As such, the mechanism appears to be robust with respect to small uncertainties in the model parameters.

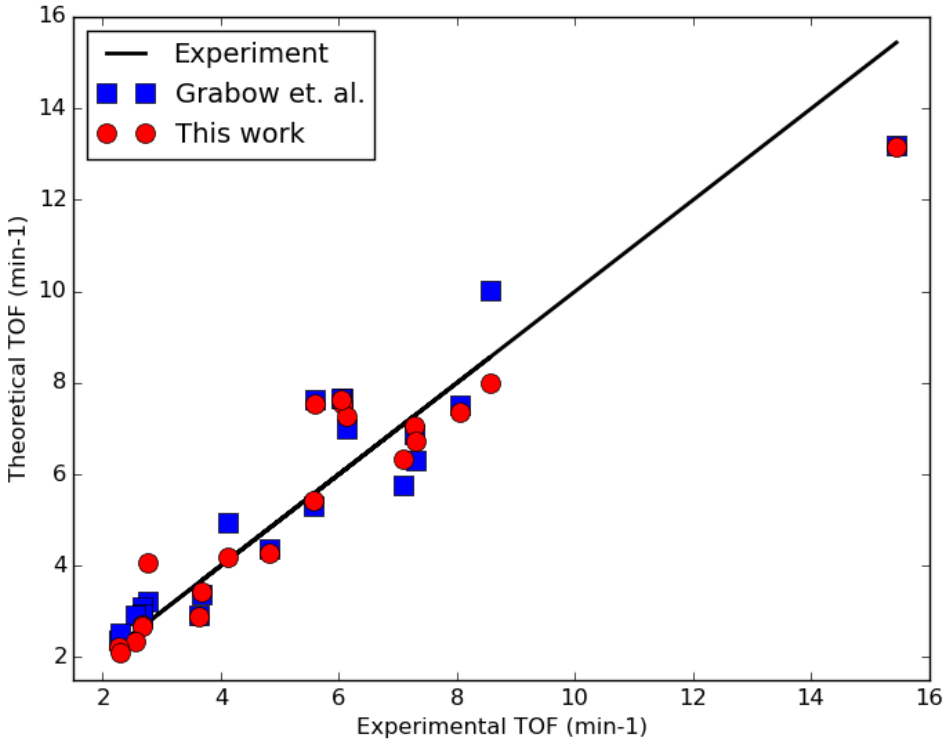

Figure 1.4: Predicted TOF versus experimental TOF for this work (red) and Grabow et al. (blue).

Both microkinetic models were optimized to reproduce the experimental TOF across a

Table 1.2: Experimental conditions and TOF for experiment, Grabow et. al. model and our model for all 21 conditions. Condition 7 is the condition referenced in the paper. Temperature is in units of Kelvin, flow rate is in cm3/min and TOF are in units of [min-1] and

Id #	Temp	y(CO)	y(H_2O)	y(CO_2)	y(H_2)	Flowrate	exp. TOF	Grabow TOF	Micki TOF
1	523	0.154	0.208	0	0	102.9	3.68	3.38	3.44
2	548	0.055	0.208	0	0	85.9	8.56	10.01	7.98
3	548	0.105	0.208	0	0	97.4	8.06	7.51	7.37
4	548	0.137	0.062	0	0	118	3.63	2.93	2.89
5	548	0.144	0.104	0	0	114.8	4.81	4.36	4.28
6	548	0.148	0.145	0	0	108.4	5.56	5.31	5.43
7	548	0.145	0.208	0	0	101.4	7.27	6.87	7.06
8	548	0.106	0.208	0.068	0	106.9	6.05	7.65	7.55
9	548	0.104	0.208	0.109	0	105.6	5.59	7.63	7.55
10	548	0.14	0.208	0.151	0	110.1	6.12	7.01	7.27
11	548	0.102	0.208	0.192	0	109.1	6.03	7.67	7.64
12	548	0.134	0.208	0	0.037	103.5	4.13	4.94	4.20
13	548	0.156	0.208	0	0.037	102.1	2.77	3.21	4.08
14	548	0.13	0.208	0	0.123	105.9	2.67	3.1	2.72
15	548	0.134	0.208	0.177	0.123	95.7	2.67	2.95	2.69
16	548	0.132	0.208	0	0.173	103.8	2.55	2.91	2.35
17	548	0.145	0.208	0	0.191	94.4	2.28	2.38	2.22
18	548	0.159	0.208	0	0.208	101.1	2.29	2.54	2.11
19	548	0.198	0.208	0	0	102.6	7.29	6.31	6.74
20	548	0.223	0.208	0	0	88.3	7.09	5.76	6.34
21	573	0.15	0.208	0	0	103.4	15.44	13.2	13.16

range of conditions. As can be seen in figure 1.4 and 1.2, our model reproduces the experimental TOFs modestly better than Grabow et al., but with significantly less required refinement. In Table 1.3, we find that we can reasonably reproduce experimental rate orders and activation energy, quantities that the model is not directly parameterized to reproduce. The CO(g) rate order is much closer to experimental value than that of Grabow et al. Both our model and Grabow et al. predict a rate order of H_2O(g) that is too large, although our model is further from the experimental value. Note that the binding energy of H_2O(g) was not refined and such refinement may allow for some improvement. The apparent activation energy is slightly higher than the experimentally observed value, but is only 1.1 kJ/mol outside the stated experimental error.

Table 1.3: Reaction orders and apparent activation energy, with their respective error bars, as derived from: (i) experiments based on averaged TOF values for each condition, (ii) microkinetic model from Grabow et al. and (iii) microkinetic model from this work

	Experiment	Grabow et al.	This work
H_2O	0.56 ± 0.05	0.70	0.85
CO	-0.14 ± 0.05	-0.37	-0.17
H_2	-0.33 ± 0.04	-0.39	-0.39
CO_2	0.02 ± 0.09	-0.03	0.00
Ea	71.4 ± 5.2 kJ/mol	67.8 kJ/mol	77.8 kJ/mol

Using Campbell's degree of rate control, Grabow et al. found that the splitting of water had a χ_{RC} of 0.08, the formation of CO_2(g) from decomposition of COOH* and from O* assisted decomposition of COOH* had χ_{RC} values of 0.55 and 0.03 respectively.[15] Although OH* assisted decomposition has a much lower barrier (almost spontaneous) than these other two decomposition pathways, this pathway is limited by the lack of OH* on the surface. This is how Grabow et al. explain the promotional effects of H_2O.

We find that water splitting as a χ_{RC} of 0.23 and the formation of COOH* from CO* and OH* has a χ_{RC} of 0.49. Since the formation of CO_2(g) does not proceed through the O* as-

sisted pathways in our model, we find that those steps have zero rate control. Although we see the degree of rate control primarily in the formation of COOH* instead of the consumption of COOH*, this is still consistent with the experimental observation with the promotional effects of H_2O(g). An increase in H_2O(g) would lead to more H_2O* and therefore more OH*, thus increasing that rate of formation of COOH*, which is the rate limiting step. Overall, both our microkinetic model and Grabow's microkinetic model conclude that the WGS reaction is limited by the low concentration of OH* on the surface.

1.7 Conclusion

We have developed a general-purpose, Python-based microkinetic modeling code (Micki) that enables the rapid development and solution of first-principles microkinetic models. Micki incorporates several key methodological advancements, including: accounting for multi-dentate adsorbates; thermodynamically-consistent lateral interactions; coverage-dependent transition state energies; and treatment of mass transport under solution-phase conditions.

Micki can currently model a wide variety of common reactors, including batch reactors, CSTRs and PFRs, and is easily extensible to alternative reactors. The code also features built-in support for various analyses,including χ_{RC} and *TRC*, allow for determination of the dominant reaction mechanism(s), and the rate-/selectivity-determining step(s).

We have also demonstrated a concrete application of Micki to the case of Pt-catalyzed water-gas shift (WGS). We find that the resulting microkinetic model is able to quantitatively reproduce prior experimental TOF for this reaction with minimal empirical refinement, and that the observed mechanism is stable with respect to the expected uncertainty in the DFT-calculated parameters. The resulting microkinetic model is also in good accord with other key experimental observables such as rate orders and the apparent activation energy. We antici-

pate that Micki will dramatically reduce the barriers to the derivation and application of future first-principles-based microkinetic models for related heterogeneously catalyzed processes.

Micki is an open source software distributed via a GNU Lesser General Public License v3.0. Micki requires Python 2, Atomic Simulation Environment (ASE), NumPy, SymPy and Sundials (a C ODE library)[90,129,114,65] and should be compatible with any modern operating system via a Fortran and C compiler. A link to the Micki code and further documentation can be found on our website, http://schmidt.chem.wisc.edu.

2

The Role of Tellurium Dopants in the Palladium Catalyzed Esterification of Primary Alcohols

Reproduced with permission from Hermes, E. D.; Janes, A. N.; Schmidt, J.R. Mechanistic Insights into Solution-Phase Oxidative Esterification of Primary Alcohols on Pd(111) from First-Principles Microkinetic Modeling. ACS Catal. 2018, **8**, 272–282.

EDH performed electronic structure calculations for all species on Pd(111) from the reactants to the aldehyde intermediate. All other electronic strcuture calculations were performed by ANJ. All microkinetic models discussed in detail in this section were created by ANJ.

2.1 Introduction

Solution phase selective oxidation of alcohols to carbonyls is a crucial industrial process for a variety of synthetic applications from pharmaceuticals to industrial bulk chemicals.[160] Aldeyhdes and esters are of particular interest for the fine chemical industry.[182,9,154] These compounds are often synthesized through oxidation of their alcohol analogue, using stoichiometric amounts of toxic molecular reagents.[155] This process is both inefficient and generates substantial amounts of byproducts.[133] Alternatively, these compounds can be selectively oxidized with environmentally benign molecular oxygen using a heterogeneous catalyst.[99] Traditionally, these heterogeneously catalyzed aerobic processes occur over a platinum-group metal (PGM) such as Pt or Pd[155] with activity and selectivity increased by the inclusion of P-block promoters such as Bi, Te or Pb.[33,104,100,99]

Te, along with Bi, has been shown to have strong promoting abilities.[190,55,140,93] While Bi is insoluble and likely forms adatoms on the PGM surface[128], Te is soluble in Pd and yields a disordered alloy up to 0.125 mole fraction Te.[45,18] Therefore, we predict that Te is likely incorporated in the catalyst surface, forming a Pd-Te alloy, instead of the adatom model commonly used for Bi[117,118] and alkali promotion.[70] One of the most prominent examples of Te promotion in industry is the production of tetrahydrofuran, where a Pd-Te intermetallic com-

pound catalyzes the oxidative diacetoxylation of butadiene (patented by the Mitsubishi corporation).[175,130] Pyruvate can also be formed effectively by oxidizing lactate over a Pd-Te alloy, although the formation of a Pd-rich intermetallic phase was found to kill catalytic activity.[55]

The mechanism for oxidative esterification of primary alcohols over PGMs remains unresolved. While for some alcohols (such as benzyl alcohol), an aldehyde intermediate can be measured, for primary alcohols (specifically 1-octanol), no aldehyde intermediate has been detected.[104] Assuming an aldehyde forms but reacts too rapidly for detection, there are several proposed mechanisms for aldehyde formation. Under basic conditions, the alcohol can be deprotonated in solution and then undergo hydride elimination on the surface to form the aldehyde.[26] However, the reaction has been known to happen in acidic conditions as well, prompting authors to propose that the alkoxide forms on the surface.[25,151] Some have proposed that instead of breaking the O-H bond in the alcohol, the C-H bond is broken first.[180,139]

Further oxidation of the aldehyde to form the desired ester has several proposed mechanisms. The aldehyde could undergo oxidation on the surface, which would explain why no aldehyde intermediate can be measured experimentally.[140] Or, the aldehyde could desorb from the surface and react with an alcohol in solution to form a hemiacetal which subsequently forms the desired ester product.[2,91,110]

Experimental measurements of the Pt metal catalyst working potentials indicate that the alcohol substrate-exposed working catalyst is reduced relative to the oxidized air-exposed resting catalyst.[101,66] However, further surface characterization is limited by the complexity of performing *in situ* measurements of liquid-phase heterogeneous catalysts.

Recently, Te along with Bi has been found to promote a Pd catlayst for primary alcohol oxidation.[140,104] The inclusion of both Te and Bi yields better conversion than either independently and thus it is likely they promote the catalyst through unique mechanisms.

A number of mechanisms for promotion have been hypothesized. (1) promoter atoms could

block ensembles of active sites necessary for unwanted side reactions that lead to catalyst poisoning[32,118,81] such as decarbonylation of the alcohol.[153] (2) they could create unique catalytic centers, creating a simultaneous interaction of the adsorbate with both the promoter and the Pd/Pt atom.[189,167] (3) the creation of a bi-functional catalyst, where different reactants/reactions are catalyzed by different surface materials.[100,102] Bi-functional catalysts are often proposed where there is evidence of distinct spatial domains of the PGM catalyst and promoter (often an oxide). (4) the formation of an alloy or intermetallic, changing the electronic nature of the surface of the catalyst and creating unique catalytic centers.[190,134,55]

In order to understand the mechanism of oxidative esterification of primary alcohols without promoters, we use Pd(111)-catalyzed esterifcation of 1-propanol to methyl propionate under basic conditions as a model of aliphatic primary alcohol esterifcation to understand the reaction pathways. We utilize first-principles microkinetic modeling informed by density functional theory (DFT) calculations of the catalyst surface and the solution-phase species. Microkinetic analysis of the reaction network allows us to identify the dominant reaction pathways that contribute to the catalytic activity from the large number of possible routes from propanol to the final ester product. It also facilitates a direct examination of the state of the catalyst under working conditions and the role of various reactants and reactions. In our work, We build microkinetic models of both the unpromoted Pd(111) surface and a Te promoted Pd(111) surface and contrast the results to elucidate that the role of Te promoters is mainly an electronic effect. Finally, we build a modified unpromoted model that confirms our prediction of an electronic promotion effect.

2.2 Theoretical Methods

All calculations were performed at the same level of theory as in Hermes et al.[60] Calculations were performed using the periodic density functional code VASP[83,85,86,84]. Projector Augmented Wave (PAW) pseudopotentials were used with a cutoff of 450 eV.[10] All calculations were run using the Python environment ASE.[90] Geometry optimizations and vibrational frequency calculations were performed with the PDE-D3(ABC) dispersion-corrected density functional method and single-point energies were evaluated with the range-separated HSE06-D3(BJ,ABC) method at the PBE-D3(ABC) geometries.[135,136,63,62,68,186,49,50,116] Although more computationally intensive than typical semilocal functionals, the inclusion of exact exchange has substantial effect on reaction barrier heights and intermediate binding energies.[42,197,201] PBE-D3(ABC) yields a bulk lattice constant of 3.90 Å, which compares favorably to the experimental lattice constant of 3.89 Å.[39] The Pd(111) surface was modeled as a 4-layer 3x3 slab with a 15 Å vacuum gap where the bottom 2 layers were fixed while the top two layers were allowed to relax. The Brillouin zone was sampled with a 3x3x1 Monkhorst-Pack k-point mesh.[131] Solvation effects on the catalyst surface and adsorbed intermediates were included through the use of single point GLSSA13 continuum solvation model calculations using VASPsol with methanol as the solvent at the PBE-D3(ABC) level of theory.[?] [107,108] Transition states were located using the nudged elastic band method[159,58] and were optimized using the dimer method.[64,57,77] All transition states have exactly one imaginary vibrational frequency corresponding to the reaction coordinate.

Solution phase species were optimized in Gaussian 09[37] with the PBE-D3(ABC) method using the aug-cc-pVTZ basis set[28] and the SMD continuum model[105] with methanol as the solvent. SMD was chosen since it was parametrized to reproduce experimental total free energies of solvation, including the cavitation energy. It should be noted that for periodic cal-

culations involving the catalyst surface, the GLSSA13 PCM was used instead of SMD. This was done because SMD is parametrized to reproduce experimental free energies of solvation, which include contributions arising from the loss of translational entropy of gas-phase species. This is not relevant for immobile systems, such as adsorbates on the catalyst surface. Similarly, GLSSA13 would predict inaccurate solvation free energies of species in solution because of its neglect of translational entropy loss. Single-point calculations were performed with and without solvation correction to determine the free energy of solvation, which was used to correct the energy of the gas-phase species as determined in VASP (see Figure 2.1). Additionally, the energy of each species carrying a formal negative charge was determined by performing calculations of the corresponding neutral radical in VASP and adding to that the electron affinity of that species as determined in Gaussian. Single point calculations were performed using the HSE06-D3(BJ,ABC) method[116] and the energies were extrapolated to the complete basis set limit using the aug-cc-PVnZ basis sets (n=2 to 5). For more details on how the solvation energy was applied to both neutral and charged species, see Hermes et al.[60]

The reaction network was analyzed using the Micki package[61] detailed in Chapter 1 which allows for the construction and solution of microkinetic models from ab initio calculations. On-surface reaction rate constants were calculated using transition state theory. Reverse rate constants were chosen such that all of the reactions obey detailed balance. For barrierless on-surface reactions, transition state theory was used with a free energy barrier of zero eV in the exothermic direction, resulting in a rate constant of $k_B T/h$. We treat O_2(g) as a gas-phase species and enforce its equilibrium surface converage. This is done because O_2 has a low solubility in methanol and is typically introduced to the system by bubbling gas through the reactor. The rates of adsorption of all solution-phase species were calculated using a Langmuir equilibration−diffusion model (see Chapter 1 Figure 1.2), which is described in detail in Chapter 1. In all of the simulations, a stationary layer thickness of 100 µm was used for diffusion.

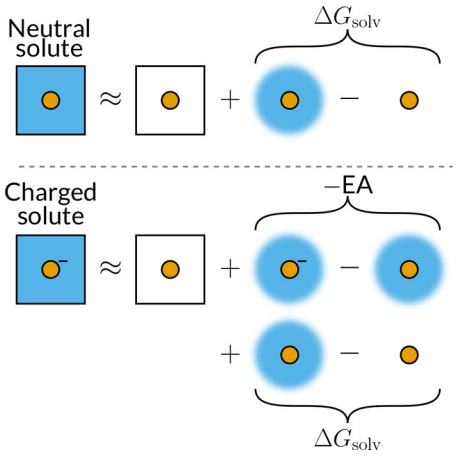

Figure 2.1: Schematic illustration of energy calculations for solution-phase species. The energy of a species in solution under periodic boundary conditions is approximated as the energy of the species in the absence of solvation under periodic boundary conditions plus the free energy of solvation, which is determined using Gaussian and SMD. For anions, we calculate the energy of the corresponding neutral radical under periodic boundary conditions without solvation and then add both the electron affinity and the solvation free energy determined using Gaussian and SMD.

This choice of length scale was motivated by a model for the laminar creeping flow of solvent around spherical nanoparticles with a diameter of 1 nm.

The free energies of adsorbates were calculated by treating all molecular degrees of freedom under the harmonic oscillator approximation. Vibrations involving metal atoms were omitted from the analysis. O_2(g) was treated as an ideal gas.

The free energy for adsorbates are calculated as

$$G_{ads} = E_{elec} + G_{vib} TS_{conf}, \tag{2.1}$$

where E_{elec} is the electronic energy, G_{vib} is the vibrational free energy, and S_{conf} is the configurational entropy. S_{conf} is zero for all species that occupy only a single adsorption site in the microkinetic model, and $k_B ln^{\frac{N_{conf}}{}}$ for species occupying multiple sites, where N_{conf} is the number of equivalent configurations of the species on the surface and σ is the symmetry of the molecule with respect to its binding geometry. Most transition states are considered to take

up two sites, with N_{conf} = 6 corresponding to the hexagonal symmetry of the Pd(111) surface. Most species have a symmetry number of σ = 1, except for symmetrical transition states such as homolytic cleavage of O_2 to two O atoms. The free energy of O_2 was calculated under the ideal gas approximation as

$$G_{gas} = E_{elec} + G_{vib} + G_{rot} + G_{trans} + k_B T ln(2 * S + 1), \tag{2.2}$$

where G_{rot} is the rotational free energy, G_{trans} is the translational free energy, S is the spin, and E_{elec} and G_{vib} are defined in the same way as for adsorbates. For O_2, S = 1, as it is a triplet in its ground state.

The free energies of solution-phase species were calculated by adding the free energy of solvation determined by the SMD continuum solvation model to the free energy of the species in the gas phase determined with the ideal gas approximation. This procedure results in an accurate approximation to the absolute free energy of the solution-phase species. The reference state of O_2(g) and all solution-phase species was chosen to be 1 M, which is the standard state for solution-phase species. It should be noted that this choice affects the reported free energy of adsorption but does not affect any thermodynamic or kinetic parameters of the model. A diffusion constant of $2 \times 10^9\ m^2/s$ was used for all solution-phase species. We find that while adsorption is diffusion-limited, it is not rate-limiting, and therefore, the results of our microkinetic model are invariant to the choice of diffusion constant to within an order of magnitude for all species. We assume that the base reacts with the solvent (methanol) quantitatively to form methoxide, and we ignore the presence of any resulting conjugate acid. In this way, we control the concentration of the base by changing the concentration of methoxide in solution. We further set the concentration of the propoxide anion in solution to obey the predicted equilibrium for proton transfer from propanol to methoxide.

In order to properly model the adsorption and desorption of anions, we model our catalyst as a double layer capacitor in which the stored energy is related to the excess charge on the catalyst surface,

$$E_{cap} = \frac{1}{2}\frac{Q^2}{C} \tag{2.3}$$

where Q is the net charge on the catalyst and C is the effective capacitance of the double layer capacitor. Then, the differential energy of adding a single electron is

$$\frac{dE_{cap}}{dN_{e^-}} = \frac{Q}{C}\frac{dQ}{dN_{e^-}} = \frac{e^2}{C}N_{e^-} \equiv \Delta E_{cap}\vartheta_{e^-} \tag{2.4}$$

where e is the elementary electron charge, N_e is the number of electrons on the catalyst and ϑ_{e^-} is the electron surface coverage. The experimentally determined capacitance of a non-oxidized Palladium electrode is 23.1 μF cm^2.[31] Given that a single adsorption site of a Pd(111) catalyst has an area of approximately 6.57 Å^2, this corresponds with an absolute capacitance of approximately 1.52×10^{20} F per site. ΔE_{cap} is the differential energy associated with adding or removing one electron from the catalyst surface per adsorption site, and is equal to approximately 10.5 eV.

The binding energies of all stable intermediates were also calculated on the H-saturated surface with a single hydrogen atom removed to make room for the adsorbate. The resulting binding energies were used to construct a linear dependence of the binding energies of all intermediates on the H coverage. Similar calculations were done to determine the lateral self-interactions of O and O2. The lateral self-interactions of H, O, and O_2 were fitted to

$$E(slab + nX) - E(slab) = nE(slab + X) + \frac{n^2}{m}E(X \cdots X) \tag{2.5}$$

where E(slab + X) is the energy of X on the surface at infinite dilution, m is the number of binding sites in the periodic slab model (in our model, m = 9), and E(X···X) is the mean-field lateral interaction of species X with itself. We fit the zero- coverage energy and lateral interaction energies of H, O, and O_2 by solving this equation exactly for n = 1 and n = 9. For the lateral interaction of other species with H, we solve a similar equation,

$$E(slab+X+nH)-E(slab)nE(slab+H)-\frac{n^2}{m}E(H\cdots H)=E(slab+X)+\frac{n^2}{m}E(H\cdots X) \quad (2.6)$$

This equation is solved exactly for n = 0 and n = 8. Corrections to the free energy of the transition state are detailed in Chapter 1.4.2.

While the method described above is computationally and combinatorially possible to account for effects of hydrogen coverage, it is not usable to capture the effects of increased coverage of larger (greater than 3 carbon backbone) species. Therefore, we create a term, called dE_{bulky}, to account for the coverage effects of large species due to steric hindrance and stop the unphysical buildup of large species with the functional form

$$dE_{bulky} = e^{(100(\Theta_{bulky}-0.4))} \quad (2.7)$$

where Θ_{bulky} is the sum of the coverage of all species with three or more carbons and dE_{bulky} is the amount by which the large species are destabilized. This limits the total amount of large species to below 40 % by approximating the interactions of large species as steric hindrance and avoids the need to compute multiple interaction energies between large species. An example showing agreement between dE_{bulky} and the DFT calculated self interaction energy for propanol is shown in Figure 2.2. Species with a backbone of 5 atoms, such as the product methyl propionate were modelled as binding to two adsorption sites, using the derivation of multidentate binding in 1.2.2.

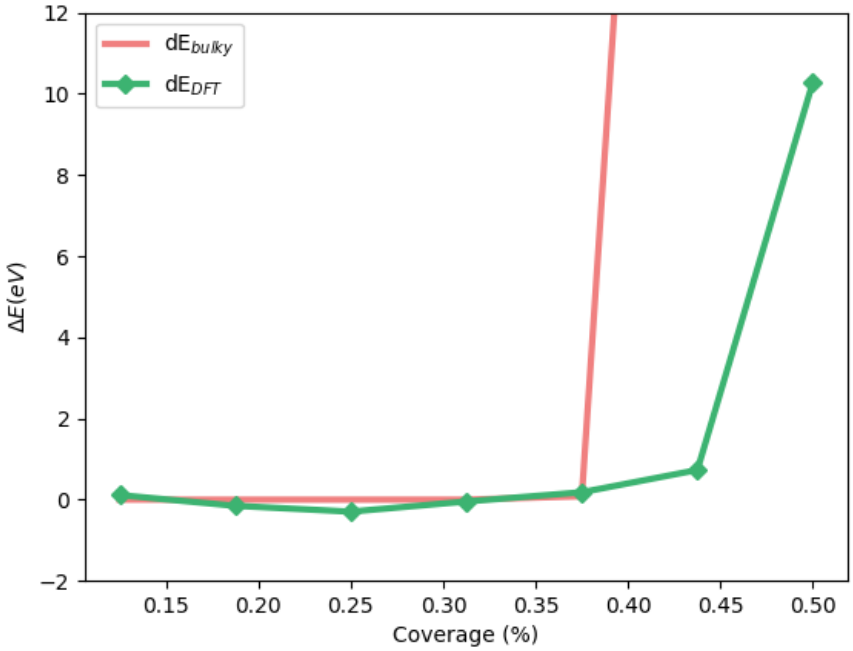

Figure 2.2: Plot of DFT calculated self interaction energy of propanol (green) versus the approximate equation to represent the interaction, dE_{bulky}(red).

The reactor was modeled as an idealized continuous stirred- tank reactor (CSTR) as described in 1.5.4 at 330 K. The gas- and solution-phase concentrations of all reactants and products were fixed at their initial values. The coupled differential equations were solved until the rates of change of all concentrations and coverages were less than $1 \times 10^{-6} s^{-1}$. Sensitivity analysis was performed by numerically perturbing model parameters and rerunning the model to find the new steady-state conditions as detailed in section 1.5.2. For each reaction, Campbell's degree of rate control (χ_{RC}) was determined by increasing and decreasing the forward and reverse rate constants by 0.1%. For each species, the thermodynamic rate control (χ_{TRC}) was determined by increasing and decreasing the free energy of the species by 0.001 $k_B T$.

2.3 Results and Discussion

2.3.1 Unpromoted Pd(111) Microkinetic Model

Table 2.1: Free energies of reaction and forward and reverse free energy barriers for the all reactions considered in the microkinetic model (discussed later) on the pristine catalyst. Missing values for $\Delta G^{\ddagger}_{\text{for}}$ and $\Delta G^{\ddagger}_{\text{rev}}$ indicate that the reaction is barrierless.

Reaction	ΔG (eV)	$\Delta G^{\ddagger}_{\text{for}}$ (eV)	$\Delta G^{\ddagger}_{\text{rev}}$ (eV)
$RCH_2OH_{(sol'n)} + * \longleftrightarrow RCH_2OH*$	−0.35		
$RCH_2O^-_{(sol'n)} + * \longleftrightarrow RCH_2O* + e^-$	−1.97		
$CH_3O^-_{(sol'n)} + * \longleftrightarrow CH_3O* + e^-$	−1.52		
$O_{2(g)} + * \longleftrightarrow O_2*$	0.06		
$RCH_2OH* + * \longleftrightarrow RCH_2O* + H*$	0.47	1.21	0.74
$RCH_2OH* + O* \longleftrightarrow RCH_2O* + OH*$	0.33		
$RCH_2OH* + OH* \longleftrightarrow RCH_2O* + H_2O*$	−0.02		
$RCH_2OH* + O_2* \longleftrightarrow RCH_2O* + OOH*$	0.21		
$RCH_2OH* + * \longleftrightarrow RCHOH* + H*$	−0.11	0.78	0.67
$RCH_2O* + * \longleftrightarrow RCHO* + H*$	−0.85	0.29	1.14
$RCH_2O* + O* \longleftrightarrow RCHO* + OH*$	−0.41	0.65	1.78
$RCH_2O* + OH* \longleftrightarrow RCHO* + H_2O*$	−0.76	0.83	2.08
$RCHOH* + * \longleftrightarrow RCHO* + H*$	0.10	0.73	0.63
$RCHOH* + O* \longleftrightarrow RCHO* + OH*$	−0.41		
$RCHOH* + OH* \longleftrightarrow RCHO* + H_2O*$	−0.76		
$RCHOH* + O_2* \longleftrightarrow RCHO* + OOH*$	−0.53		
$RCHO* \longleftrightarrow RCHO_{(sol'n)} + *$	0.27		

Table 2.1 (continued)

$RCHO* + * \leftrightarrow RCO* + H*$	−0.83	0.10	0.93
$RCO* + CH_3O* \leftrightarrow RCOOCH_3* + *$	−1.09	0.16	1.25
$RCHO_{(sol'n)} + CH_3O^-_{(sol'n)} \leftrightarrow RCHOOCH^-_{3(sol'n)}$	−0.20		
$RCHOOCH^-_{3(sol'n)} + * \leftrightarrow RCHOOCH_3* + e^-$	−2.26		
$RCHOOCH_3* + * \leftrightarrow RCOOCH_3* + H*$	−1.25	0.41	1.66
$RCHOOCH_3* + O* \leftrightarrow RCOOCH_3* + OH*$	−1.39	0.50	1.89
$RCOOCH_3* \leftrightarrow RCOOCH_{3(sol'n)} + *$	0.61		
$O_2* + * \leftrightarrow 2\,O*$	−1.89	0.87	2.76
$O_2* + H* \leftrightarrow OOH* + *$	−0.26	0.69	0.95
$OOH* + * \leftrightarrow O* + OH*$	−1.77	0.07	1.84
$O* + H* \leftrightarrow OH* + *$	−0.14	0.94	1.08
$OH* + H* \leftrightarrow H_2O* + *$	−0.49	0.81	1.30
$2\,OH* \leftrightarrow H_2O* + O*$	−0.35	0.52	0.87
$OH* + e^- \leftrightarrow OH^-_{(sol'n)} + *$	1.55		
$H_2O* \leftrightarrow H_2O_{(sol'n)} + *$	−0.03		
$CH_3O* + H* \leftrightarrow CH_3OH* + *$	−0.67	0.52	1.19
$CH_3OH* + O* \leftrightarrow CH_3O* + OH*$	0.54		
$CH_3OH* + OH* \leftrightarrow CH_3O* + H_2O*$	0.19		
$CH_3OH* + O_2* \leftrightarrow CH_3O* + OOH*$	0.41		
$CH_3OH* \leftrightarrow CH_3OH_{(l)} + *$	0.13		
$2\,H* \leftrightarrow H_{2(sol'n)} + 2\,*$	1.08		
$H* + O_2* + CH_3OH_{(l)} \leftrightarrow OOH* + CH_3OH$	−0.26	0.34	0.6

Table 2.2: Free energies of reaction and forward and reverse free energy barriers for the all reactions considered in the microkinetic model (discussed later) under steady state conditions. Missing values for $\Delta G^{\ddagger}_{\text{for}}$ and $\Delta G^{\ddagger}_{\text{rev}}$ indicate that the reaction is barrierless.

Reaction	ΔG (eV)	$\Delta G^{\ddagger}_{\text{for}}$ (eV)	$\Delta G^{\ddagger}_{\text{rev}}$ (eV)
$RCH_2OH_{(sol'n)} + * \longleftrightarrow RCH_2OH*$	−0.20		
$RCH_2O^-_{(sol'n)} + * \longleftrightarrow RCH_2O* + e^-$	−0.21		
$CH_3O^-_{(sol'n)} + * \longleftrightarrow CH_3O* + e^-$	0.08		
$O_{2(g)} + * \longleftrightarrow O_2*$	0.06		
$RCH_2OH* + * \longleftrightarrow RCH_2O* + H*$	0.83	1.44	0.61
$RCH_2OH* + O* \longleftrightarrow RCH_2O* + OH*$	0.33		
$RCH_2OH* + OH* \longleftrightarrow RCH_2O* + H_2O*$	−0.02		
$RCH_2OH* + O_2* \longleftrightarrow RCH_2O* + OOH*$	0.41		
$RCH_2OH* + * \longleftrightarrow RCHOH* + H*$	0.25	0.78	0.53
$RCH_2O* + * \longleftrightarrow RCHO* + H*$	−0.49	0.37	0.86
$RCH_2O* + O* \longleftrightarrow RCHO* + OH*$	−0.41		
$RCH_2O* + OH* \longleftrightarrow RCHO* + H_2O*$	−0.76		
$RCHOH* + * \longleftrightarrow RCHO* + H*$	0.10	0.73	0.63
$RCHOH* + O* \longleftrightarrow RCHO* + OH*$	−0.41		
$RCHOH* + OH* \longleftrightarrow RCHO* + H_2O*$	−0.76		
$RCHOH* + O_2* \longleftrightarrow RCHO* + OOH*$	−0.53		
$RCHO* \longleftrightarrow RCHO_{(sol'n)} + *$	0.13		
$RCHO* + * \longleftrightarrow RCO* + H*$	−0.47	0.13	0.60
$RCO* + CH_3O* \longleftrightarrow RCOOCH_3* + *$	−1.09	0.16	1.25
$RCHO_{(sol'n)} + CH_3O^-_{(sol'n)} \longleftrightarrow RCHOOCH^-_{3(sol'n)}$	−0.20		

Table 2.2 (continued)

$RCHOOCH^{-}_{3(sol'n)} + * \leftrightarrow RCHOOCH_3* + e^-$	−0.51		
$RCHOOCH_3* + * \leftrightarrow RCOOCH_3* + H*$	−0.89	0.48	1.37
$RCHOOCH_3* + O* \leftrightarrow RCOOCH_3* + OH*$	−1.39	0.50	1.89
$RCOOCH_3* \leftrightarrow RCOOCH_{3(sol'n)} + *$	0.47		
$O_2* + * \leftrightarrow 2\,O*$	−1.89	0.87	2.76
$O_2* + H* \leftrightarrow OOH* + *$	−0.62	0.34	1.16
$OOH* + * \leftrightarrow O* + OH*$	−1.77	0.07	1.84
$O* + H* \leftrightarrow OH* + *$	−0.50	0.77	1.27
$OH* + H* \leftrightarrow H_2O* + *$	−0.85	0.68	1.53
$2\,OH* \leftrightarrow H_2O* + O*$	−0.35	0.52	0.87
$OH* + e^- \leftrightarrow OH^-_{(sol'n)} + *$	−0.06		
$H_2O* \leftrightarrow H_2O_{(sol'n)} + *$	−0.03		
$CH_3O* + H* \leftrightarrow CH_3OH* + *$	−1.04	0.40	1.44
$CH_3OH* + O* \leftrightarrow CH_3O* + OH*$	−0.54		
$CH_3OH* + OH* \leftrightarrow CH_3O* + H_2O*$	−0.19		
$CH_3OH* + O_2* \leftrightarrow CH_3O* + OOH*$	0.41		
$CH_3OH* \leftrightarrow CH_3OH_{(l)} + *$	0.13		
$2\,H* \leftrightarrow H_{2(sol'n)} + 2\,*$	0.36		
$H* + O_2* + CH_3OH_{(l)} \leftrightarrow OOH* + CH_3OH$	−0.62	−0.21	0.83

Table 2.3: Steady state rate and Campbell's degree of rate control for all reactions considered in our unpromoted model.

Reaction	Rate (s^{-1})	χ_{RC}
$RCH_2OH_{(sol'n)} + * \longleftrightarrow RCH_2OH*$	14.2	0.000
$RCH_2O^-_{(sol'n)} + * \longleftrightarrow RCH_2O* + e^-$	−0.6	0.000
$CH_3O^-_{(sol'n)} + * \longleftrightarrow CH_3O* + e^-$	0.9	0.000
$O_{2(g)} + * \longleftrightarrow O_2*$	13.6	0.000
$RCH_2OH* + * \longleftrightarrow RCH_2O* + H*$	0.0	0.000
$RCH_2OH* + O* \longleftrightarrow RCH_2O* + OH*$	13.5	0.000
$RCH_2OH* + OH* \longleftrightarrow RCH_2O* + H_2O*$	14.6	0.000
$RCH_2OH* + O_2* \longleftrightarrow RCH_2O* + OOH*$	−13.9	−0.004
$RCH_2OH* + * \longleftrightarrow RCHOH* + H*$	0.0	0.000
$RCH_2O* + * \longleftrightarrow RCHO* + H*$	13.6	0.481
$RCH_2O* + O* \longleftrightarrow RCHO* + OH*$	0.0	0.000
$RCH_2O* + OH* \longleftrightarrow RCHO* + H_2O*$	0.0	0.000
$RCHOH* + * \longleftrightarrow RCHO* + H*$	0.0	0.000
$RCHOH* + O* \longleftrightarrow RCHO* + OH*$	0.0	0.000
$RCHOH* + OH* \longleftrightarrow RCHO* + H_2O*$	0.0	0.000
$RCHOH* + O_2* \longleftrightarrow RCHO* + OOH*$	0.0	0.000
$RCHO* \longleftrightarrow RCHO_{(sol'n)} + *$	0.0	0.000
$RCHO* + * \longleftrightarrow RCO* + H*$	13.6	0.000
$RCO* + CH_3O* \longleftrightarrow RCOOCH_3* + *$	13.6	0.000
$RCHO_{(sol'n)} + CH_3O^-_{(sol'n)} \longleftrightarrow RCHOOCH^-_{3(sol'n)}$	0.0	0.000
$RCHOOCH^-_{3(sol'n)} + * \longleftrightarrow RCHOOCH_3* + e^-$	0.0	0.000

Table 2.3 (continued)

$RCHOOCH_3* + * \leftrightarrow RCOOCH_3* + H*$	0.0	0.000
$RCHOOCH_3* + O* \leftrightarrow RCOOCH_3* + OH*$	0.0	0.000
$RCOOCH_3* \leftrightarrow RCOOCH_{3(sol'n)} + *$	0.47	
$O_2* + * \leftrightarrow 2\,O*$	0.0	0.000
$O_2* + H* \leftrightarrow OOH* + *$	0.0	0.000
$OOH* + * \leftrightarrow O* + OH*$	13.6	0.495
$O* + H* \leftrightarrow OH* + *$	0.0	0.0
$OH* + H* \leftrightarrow H_2O* + *$	0.0	0.000
$2\,OH* \leftrightarrow H_2O* + O*$	0.0	0.000
$OH* + e^- \leftrightarrow OH^-_{(sol'n)} + *$	0.3	0.000
$H_2O* \leftrightarrow H_2O_{(sol'n)} + *$	26.9	0.002
$CH_3O* + H* \leftrightarrow CH_3OH* + *$	0.0	0.000
$CH_3OH* + O* \leftrightarrow CH_3O* + OH*$	0.1	0.000
$CH_3OH* + OH* \leftrightarrow CH_3O* + H_2O*$	12.3	0.000
$CH_3OH* + O_2* \leftrightarrow CH_3O* + OOH*$	0.3	0.000
$CH_3OH* \leftrightarrow CH_3OH_{(l)} + *$	-12.7	0.001
$2\,H* \leftrightarrow H_{2(sol'n)} + 2\,*$	0.0	0.000
$H* + O_2* + CH_3OH_{(l)} \leftrightarrow OOH* + CH_3OH$	27.2	0.000

Reaction energies and barriers were calculated for all plausible elementary steps for the oxidative esterification of propanol to methyl propionate. The free energies of all reactions considered in this work on the pristine catalyst are presented in table 2.2, and the energies under steady state conditions are presented in table 2.1.

Table 2.4: Steady state concentrations and degree of thermodynamic rate control for all adsorbates considered in our model.

Species	Coverage	χ_{TRC}
H	0.0002	0.281
RCH_2OH	0.3448	−0.959
$RCOOCH_3$	0.0328	−0.028
CH_3OH	0.6184	−2.929
CH_3O	<0.0001	0.000
RCO	0.0001	0.000
O_2	<0.0001	0.0003
RCHO	<0.0001	0.283
$RCHOOCH_3$	0.0003	0.000
RCHOH	<0.0001	0.000
H_2O	<0.0001	0.000
O	<0.0001	0.030
RCH_2O	0.0029	0.698
OOH	<0.0001	0.951
OH	<0.0001	0.030
$*$	0.0003	

Main Reaction Pathway

Using the microkinetic model, we find one major pathway responsible for the production of methyl ester with a turnover frequency (TOF) of 13.6 s^{-1}. The major reaction pathway is as follows: propanol (RCH_2OH) is adsorbed onto the Pd(111) surface, then the O-H bond is broken through a hydroxyl assisted pathway to form water and bound propoxy. The bound propoxy (RCH_2O) will undergo C-H bond scission to form bound propanal (RCHO). This propanal will then immediately undergo another surface C-H bond scission to form bound propanoyl (RCHO). The rapid consumption of the aldehyde on the surface is consistent with the lack of experimentally detected aldehyde intermediate.[140] While the propanal intermediate could desorb and form an ester through a solution phase reaction, we do not find flux through that pathway. Then surface bound methoxy (CH_3O), formed by on surface hydroxyl assisted

O-H bond scission from methanol* and OH*, will react with the propanoyl to form the ester product, methyl propionate ($RCOOCH_3$), which then desorbs. This pathway is illustrated in figure 2.3.

The steady-state surface is 62.8 % covered with methanol and 34.5 % covered with propanol, with minimal coverage of other species as shown in Table 2.3. Based on degree of rate control analysis, the rate limiting step along the major pathway is the first C-H bond scission, forming propanal* and H* from propoxy*, with a degree of rate control of 0.48, listed in Table 2.3. This reaction is exergonic by 0.49 eV with a barrier of 0.37 eV at steady state coverage. This reaction pathway is illustrated in figure 2.4a. The rate order of O_2 is 0.50 and the rate order of the substrate propanol is 0.010. These are in qualitative agreement with experimental rate orders on the promoted PdBiTe catalysts that were experimentally determined to show saturation behavior in substrate and first order in O_2.[103] Experimental rate order data is not available for the unpromoted Pd catalyst or the PdTe catalyst.

Methanol Mediated Hydrogen Shuttling Mechanism

Due to hydrogen bonding, the solvent can accelerate H-transfer reactions. In this case, the solvent methanol is not consumed in the reaction but instead serves as a mediator of H* transfer. On a Pd(111) surface at zero coverage, the barrier to abstracting an H* atom to reduce O_2* to OOH* is 0.60 eV. It is reduced to 0.34 eV with a methanol mediator. A side view of the transition state is shown in figure **??**. A top down view of the reactants, transition state and products are in figure 2.6a. Without this reaction in the microkinetic model, the steady state solution is very different. Our previous work in Reference ref. 60 is missing this reaction. There, we found a TOF of 0.0246 s^{-}, a surface poisoned with H atoms and a main reaction pathway that had the C-H bond scission of the primary alcohol as the first bond breaking step, followed by O-H bond scission. This is qualitatively and quantitatively different than the results detailed

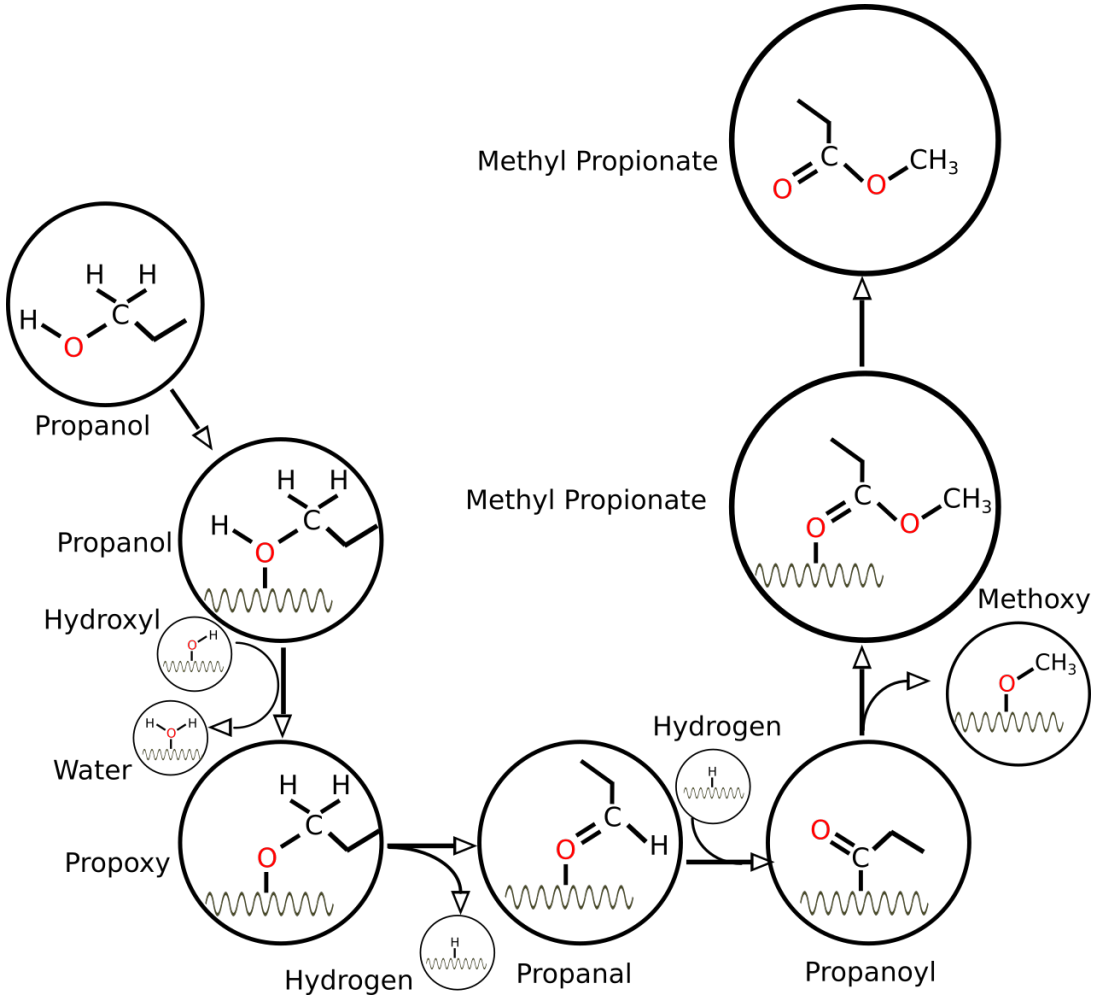

Figure 2.3: Main reaction network for the unpromoted palladium catalyst. Propanol adsorbs to the surface. First the O-H bond and then the C-H bond in propanol is broken to form propanal, which undergoes further C-H bond scission to form propanoyl which reacts with methoxy to form methyl ester, the desired product.

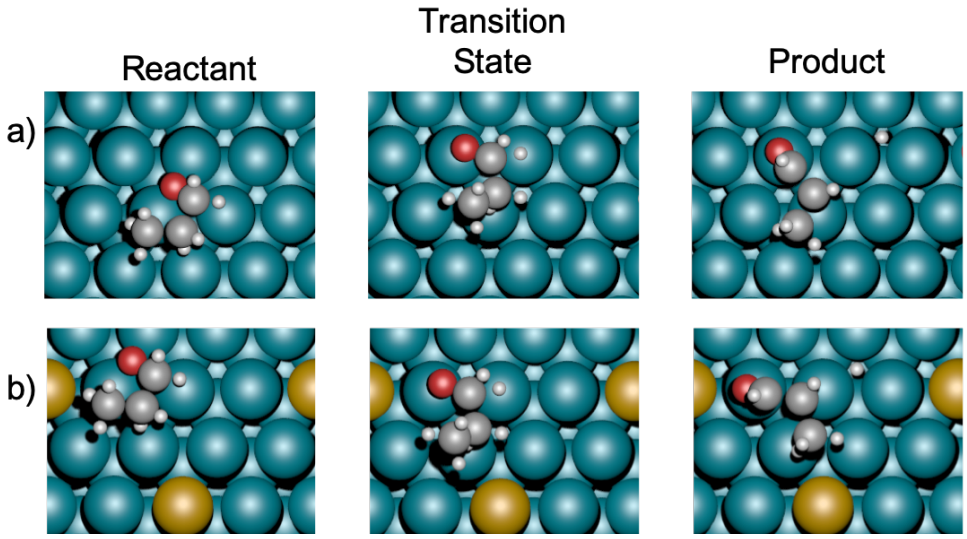

Figure 2.4: C-H bond breaking directly on surface for (a) the unpromoted palladium catalyst and (b) the Te-promoted catalyst. The structure of the reactants, transition states and products are very similar for both catalysts.

here with the experimentally feasible methanol shuttling reaction included, where we find a TOF three orders of magnitude faster, no H atom buildup on the surface and a main reaction pathway that beings with O-H bond scission, followed by C-H bond scission. This highlights a drawback of microkinetic modeling – there is no mechanism to verify that the predicted number of elementary steps includes all chemically relevant steps.

The hydrogen atoms are removed from the surface through this the methanol mediated hydrogen shuttling reaction. With the assistance of the hydrogen bonding methanol solvent, bound O_2* can abstract hydrogen atoms from the surface to form on surface OOH. At steady state, this reaction has a modest barrier of 0.21 eV and is downhill by 0.62 eV. OOH* either decomposes to form O* and OH* (with a degree of rate control of 0.50) or it can react with propoxy* to reform O_2* (and adsorbed propanol). This regenerates O_2* that can then abstract another hydrogen atom. This is illustrated in figure 2.7. The O* atoms formed can assist in breaking the O-H bond of propanol to form more OH* and propoxy. OH* assists the O-H

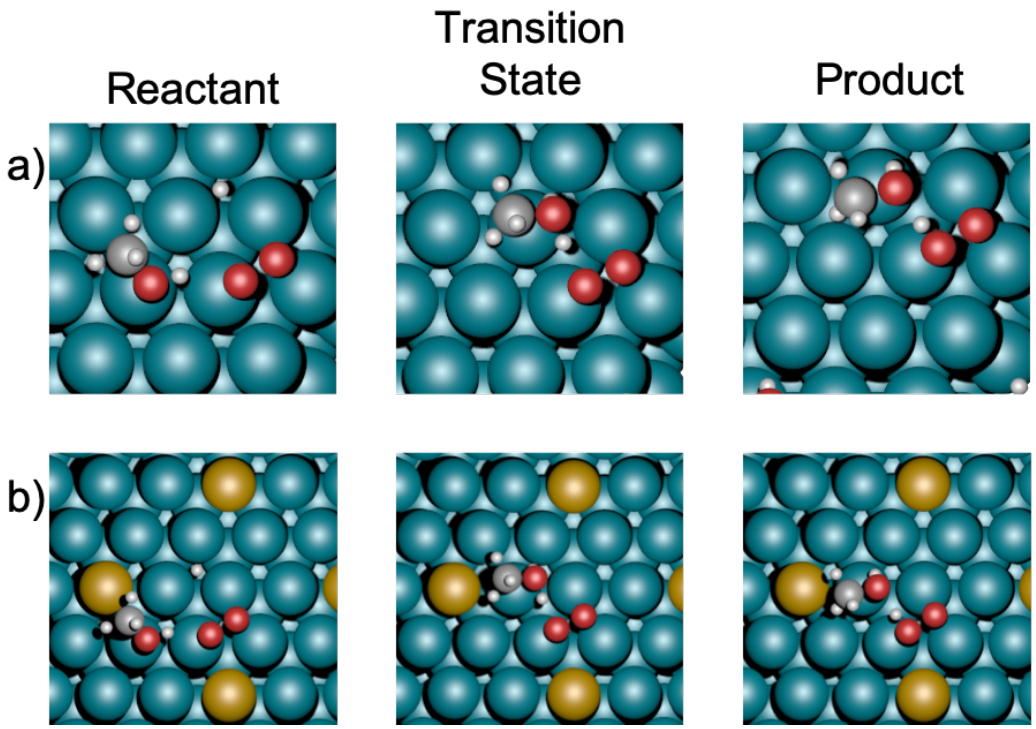

Figure 2.5: H-shuttle reactants, transition state and product for (a) the unpromoted palladium catalyst and (b) the Te-promoted catalyst. The structure of the reactants, transition states and products are very similar for both catalysts.

bond breaking of propanol to propoxy and methanol to methoxy in the main reaction pathway as seen in figure 2.3.

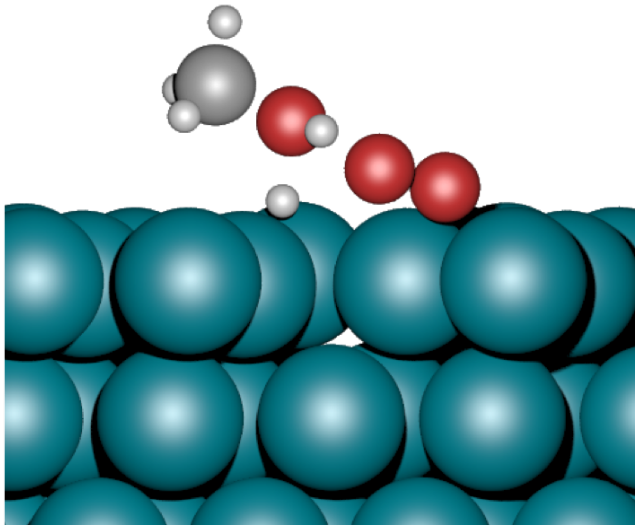

Figure 2.6: Transition state for methanol assisted H-shuttling reaction. Palladium atoms are blue, carbon atoms are gray, hydrogen atoms are white and oxygen atoms are red

Oxygen Reduction and Removal of H atoms

While the solvent-assisted H-shuttling mechanism can reduce O_2 to OOH* and subsequently O* and OH*, there must be a further step to reduce oxygen to H_2O. Direct abstraction of H* by either O* or OH* has a barrier over 1 eV on the pristine surface. Oxygen assisted C-H cleavage pathways also have barriers higher than 1 eV on the pristine surface. Therefore, oxygen assisted O-H bond scission is the only accessible pathway to reduce O* to OH* and reduce OH* to H_2O*.

As this is a base catalyzed reaction, OH* could desorb as OH^-. However, as this is not a grounded electrode catalyst, net flux of charge must be *zero*. Our double capacitor model (de-

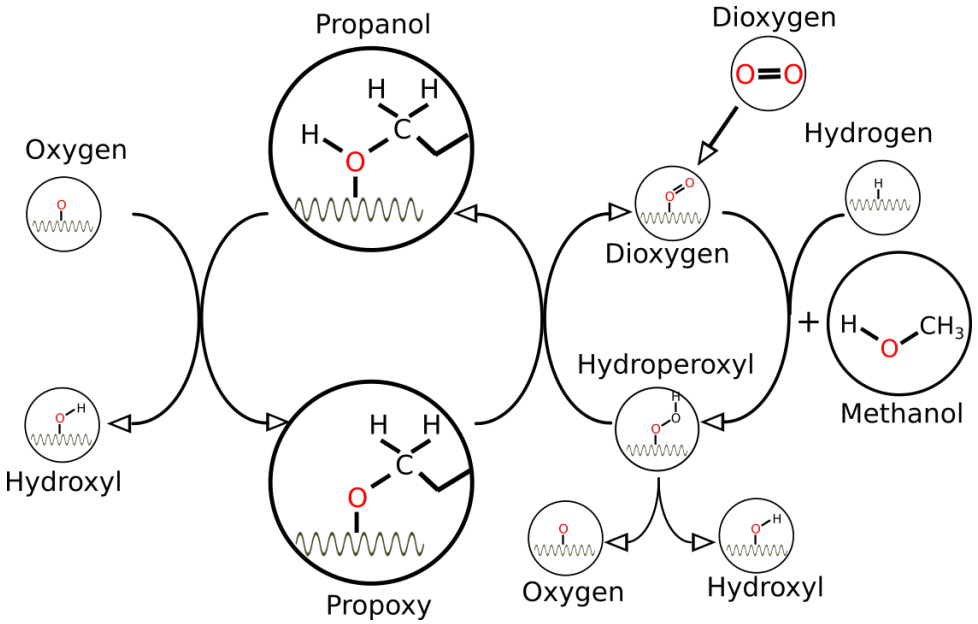

Figure 2.7: Pathway for reducing O_2 with the unpromoted catalyst

scribed in Hermes et al.)[60] ensures that on surface electron-electron repulsion is accounted for. While on a pristine surface, adsorption of charge species is more energetically favorable, this is not necessarily true at steady-state, due to electron-electron repulsion. At zero coverage, propoxide binds by -1.97 eV compared to -0.35 eV for propanol. However, at steady state, propoxide only binds by -0.25 eV, weaker than propanol. Thus, it is more energetically favorable to bind propanol than propoxide at steady state and since there is also a much higher concentration of propanol in solution than propoxide, there is a net flux of propanol *to* the surface compared to a very small net flux of propoxide *from* the surface. We see the same scenario for methoxide. The methoxide binding energy changes from -1.52 eV on the pristine surface to 0.19 eV on the steady state surface (while methanol binding is -0.13 eV). As there is no net flux of charged reactants to the surface, there cannot, therefore, be a net flux of charged products away from the surface. Thus OH* must be reduced on the surface to form H_2O*, which then desorbs as a benign side product.

Overall, the unpromoted esterification reaction over Pd(111) is limited both by how quickly the first C-H bond can be broken and how quickly OOH* can decompose to O* and OH*. The surface is poisoned by the reactants, propanol and methanol, leaving precious few sites open. Promoters could change the energetics of these two reactions to reduce their barriers or increase the concentrations of reactants in order to increase reaction flux. The promoter could also modify the relative binding energies of species so that the coverage of propanol and/or methanol is reduced.

2.3.2 Te Promoter Effects

PdTe Model Catalyst

We model tellurium as incorporated in the palladium surface as an alloy. While some studies have found ordered Pd-Te intermetallics as active phases[190,175], in general, higher catalytic activity is seen at lower concentrations of tellurium.[55] Promotion also occurs when catalysts are prepared without annealing at high temperatures required to form stable Pd-Te intermetallic phases.[140,178,89] Under these mild conditions, tellurium is found preferentially near the surface of palladium nanoparticles.[89] This indicates that tellurium is most likely incorporated into the system not as an ordered intermetallic or bulk disordered alloy but as a surface alloy. We performed a series of calculations on the interactions of tellurium atoms and the palladium surface. Tellurium atoms are preferentially found in the top layer of the Pd(111) surface over the subsurface layer or adsorption to a surface hollow. Aggregation of tellurium atoms are strongly disfavored, with a 0.4 eV energy penalty to forming Te-Te neighbor contact in the surface layer. We model the Pd-Te alloy as a surface-only alloy. While sub-surface tellurium would form in the next few layers as well, we find that these subsurface tellurium have a much smaller effect on adsorption energies compared to surface tellurium atoms. Therefore we only

include surface tellurium, which reduces the number of unique adsorption sites relative to the tellurium atoms. As seen in figure 2.8, we created a (4x2) supercell of the (1x$\sqrt{3}$) surface unit cell to allow for the dispersed arrangement of tellurium atoms at 1:8 surface concentrations where no palladium atom is a nearest neighbor to two tellurium atoms. This 12.5% tellurium concentration matches the bulk solubility.[45,18]

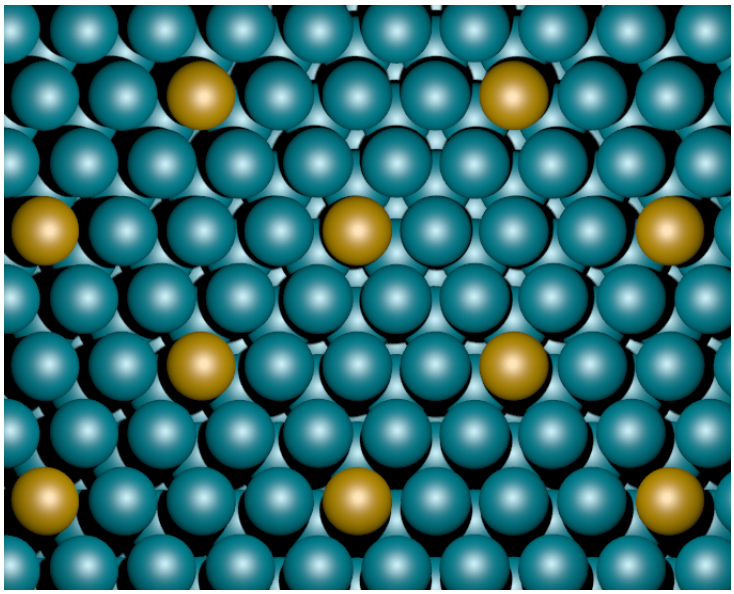

Figure 2.8: Top down view of the Pd(111)-Te surface alloy. This surface is a (4x2) supercell of the (1x$\sqrt{3}$) surface unit cell and has a Pd:Te ratio of 8:1, the solubility limit of tellurium in palladium. Palladium atoms are blue, tellurium atoms are gold.

PdTe Microkinetic Model

We calculated the adsorption energy of every species described above on both palladium and tellurium sites and found that the lowest energetic binding site for all species was on palladium atoms. Additionally, the binding geometry on palladium atoms in the PdTe(111) was very similar to that on the Pd(111) surface. This can be seen in figures 2.4 and 2.5. For each reaction, we considered the reaction occurring with reactants and products on both tellurium and palla-

dium atoms. This allows us to account for promotional effects due to unique active sites created by Pd-Te neighbors. However, we find that for all reactions except the splitting O_2* bound to a tellurium site to two O* atoms, one bound to tellurium and one to palladium, the reaction barrier is lowest when all reactants/products are on palladium atoms, indicating that any species bound to tellurium diffuse from tellurium to palladium before undergoing a reaction except for the splitting of O_2*. Therefore, the total number of reactions are the 36 considered in the unpromoted model, the splitting of $O_2\cdot$ bound to a Te site, as well as diffusion reactions for all species between Te and Pd sites.

Two Site PdTe model results

We created a microkinetic model with two distinct binding sites, Te and Pd that allows for adsorption to both types of sites, diffusion between sites and the one reaction that involves Pd-Te neighbors for the active site, as well as all the reactions that occur on the palladium atoms. This model will capture promotional effects due to the difference in electronics between PdTe(111) and Pd(111) as well as effects due to site blocking and bi-functional catalysis.

Table 2.5: Free energies of reaction and forward and reverse free energy barriers for the all reactions considered in the PdTe(111) microkinetic model under pristine conditions. Missing values for $\Delta G^{\ddagger}_{\text{for}}$ and $\Delta G^{\ddagger}_{\text{rev}}$ indicate that the reaction is barrierless.

Reaction	ΔG (eV)	$\Delta G^{\ddagger}_{\text{for}}$ (eV)	$\Delta G^{\ddagger}_{\text{rev}}$ (eV)
$RCH_2OH_{(sol'n)} + * \longleftrightarrow RCH_2OH*$	−0.17		
$RCH_2O^-_{(sol'n)} + * \longleftrightarrow RCH_2O* + e^-$	−1.83		
$CH_3O^-_{(sol'n)} + * \longleftrightarrow CH_3O* + e^-$	−1.96		
$O_{2(g)} + * \longleftrightarrow O_2*$	−0.02		
$RCH_2OH* + * \longleftrightarrow RCH_2O* + H*$	0.50	1.25	0.75

Table 2.5 (continued)

$RCH_2OH* + O* \leftrightarrow RCH_2O* + OH*$	0.18	0.76	0.94
$RCH_2OH* + OH* \leftrightarrow RCH_2O* + H_2O*$	0.05		
$RCH_2OH* + O_2* \leftrightarrow RCH_2O* + OOH*$	0.44		
$RCH_2OH* + * \leftrightarrow RCHOH* + H*$	−0.11	0.60	0.71
$RCH_2OH* + O* \leftrightarrow RCHOH* + OH*$	−0.43	0.86	1.29
$RCH_2OH* + OH* \leftrightarrow RCHOH* + H_2O*$	−0.56	0.94	1.50
$RCH_2O* + * \leftrightarrow RCHO* + H*$	−0.80	0.30	1.10
$RCH_2O* + O* \leftrightarrow RCHO* + OH*$	−1.12	0.65	1.77
$RCH_2O* + OH* \leftrightarrow RCHO* + H_2O*$	−1.25	0.83	2.08
$RCHOH* + * \leftrightarrow RCHO* + H*$	−0.19	1.02	1.21
$RCHOH* + O* \leftrightarrow RCHO* + OH*$	−0.51		
$RCHOH* + OH* \leftrightarrow RCHO* + H_2O*$	−0.64		
$RCHOH* + O_2* \leftrightarrow RCHO* + OOH*$	−0.25		
$RCHO* \leftrightarrow RCHO_{(sol'n)} + *$	0.16		
$RCHO* + * \leftrightarrow RCO* + H*$	−0.76		
$RCO* + CH_3O* \leftrightarrow RCOOCH_3* + *$	−0.58	0.80	1.38
$RCHO_{(sol'n)} + CH_3O^-_{(sol'n)} \leftrightarrow RCHOOCH^-_{3(sol'n)}$	−0.20		
$RCHOOCH^-_{3(sol'n)} + * \leftrightarrow RCHOOCH_3* + e^-$	−1.16		
$RCHOOCH_3* + * \leftrightarrow RCOOCH_3* + H*$	−2.10		
$RCHOOCH_3* + O* \leftrightarrow RCOOCH_3* + OH*$	−1.49	0.69	2.18
$RCOOCH_3* \leftrightarrow RCOOCH_{3(sol'n)} + *$	0.43		
$O_2* + * \leftrightarrow 2\,O*$	−1.59	0.94	2.53
$O_2* + H* \leftrightarrow OOH* + *$	−0.12	0.79	0.91

Table 2.5 (continued)

$OOH* + * \longleftrightarrow O* + OH*$	−1.85	0.10	1.95
$O* + H* \longleftrightarrow OH* + *$	−0.32	0.58	0.90
$OH* + H* \longleftrightarrow H_2O* + *$	−0.45	0.88	1.33
$2\,OH* \longleftrightarrow H_2O* + O*$	0.12	0.47	0.59
$OH* + e^- \longleftrightarrow OH^-_{(sol'n)} + *$	1.55		
$H_2O* \longleftrightarrow H_2O_{(sol'n)} + *$	−0.15		
$CH_3O* + H* \longleftrightarrow CH_3OH* + *$	−0.14	0.95	1.09
$CH_3OH* + O* \longleftrightarrow CH_3O* + OH*$	−0.19	0.33	0.52
$CH_3OH* + OH* \longleftrightarrow CH_3O* + H_2O*$	−0.31		
$CH_3OH* + O_2* \longleftrightarrow CH_3O* + OOH*$	0.07		
$CH_3OH* \longleftrightarrow CH_3OH_{(l)} + *$	−0.04		
$2\,H* \longleftrightarrow H_{2(sol'n)} + 2*$	0.94		
$H* + O_2* + CH_3OH_{(l)} \longleftrightarrow OOH* + CH_3OH$	−0.06	0.46	−0.52
$RCHOOCH_3*^{Te} + * \longleftrightarrow RCHOOCH_3* + *^{Te}$	−0.65	0.26	0.91
$RCHOOCH^-_{3(sol'n)} + *^{Te} \longleftrightarrow RCHOOCH_3*^{Te} + e^-$	−1.44		
$RCHOH*^{Te} + * \longleftrightarrow RCHOH* + *^{Te}$	−0.84	0.04	0.88
$CH_3OH*^{Te} + * \longleftrightarrow CH_3OH* + *^{Te}$	−0.16		
$RCH_3OH_{(sol'n)} + *^{Te} \longleftrightarrow RCH_3OH*^{Te}$	0.21		
$CH_3O*^{Te} + * \longleftrightarrow CH_3O* + *^{Te}$	−0.74	0.21	0.85
$RCH_3O^-_{(sol'n)} + *^{Te} \longleftrightarrow RCH_3O*^{Te} + e^-$	−1.22		
$O_2*^{Te} + * \longleftrightarrow O_2* + *^{Te}$	−0.89		
$O_{2(g)} + *^{Te} \longleftrightarrow O_2*^{T}e$	0.86		
$O*^{Te} + * \longleftrightarrow O* + *^{Te}$	−0.78	0.21	0.99

Table 2.5 (continued)

$O_2*^{Te} + * \longleftrightarrow O* + O*^{Te}$	−1.70	0.59	2.29
$OH*^{Te} + * \longleftrightarrow OH* + *^{Te}$	−0.54	0.29	0.83
$OH^-_{(sol'n)} + *^{Te} \longleftrightarrow OH*^{Te} \equiv e^-$	−1.01		
$OOH*^{Te} + * \longleftrightarrow OOH* + *^{Te}$	−0.52	0.12	0.64
$RCHO*^{Te} + * \longleftrightarrow RCHO* + *^{Te}$	−0.18		
$RCHO(sol'n) + *^{te} \longleftrightarrow RCHO*^{Te}$	0.02		
$RCH_2OH*^{Te} + * \longleftrightarrow RCH_2OH* + *^{Te}$	−0.25		
$RCH_2OH(sol'n) + *^{Te} \longleftrightarrow RCH_2OH*^{Te}$	0.08		
$RCO*^{Te} + * \longleftrightarrow RCO* + *^{Te}$	−1.36		
$RCH_2O*^{Te} + * \longleftrightarrow RCH_2O* + *^{Te}$	−0.39		
$RCH_2O^-(sol'n) + *^{Te} \longleftrightarrow RCH_2O*^{Te}$	−1.44		

Table 2.6: Free energies of reaction and forward and reverse free energy barriers for the all reactions considered in the PdTe(111) microkinetic model under steady state conditions. Missing values for $\Delta G^{\ddagger}_{for}$ and $\Delta G^{\ddagger}_{rev}$ indicate that the reaction is barrierless.

Reaction	ΔG (eV)	$\Delta G^{\ddagger}_{for}$ (eV)	$\Delta G^{\ddagger}_{rev}$ (eV)
$RCH_2OH_{(sol'n)} + * \longleftrightarrow RCH_2OH*$	0.06		
$RCH_2O^-_{(sol'n)} + * \longleftrightarrow RCH_2O* + e^-$	0.03		
$CH_3O^-_{(sol'n)} + * \longleftrightarrow CH_3O* + e^-$	−0.06		
$O_{2(g)} + * \longleftrightarrow O_2*$	−0.02		
$RCH_2OH* + * \longleftrightarrow RCH_2O* + H*$	0.56	1.28	1.84
$RCH_2OH* + O* \longleftrightarrow RCH_2O* + OH*$	0.18	0.76	0.94
$RCH_2OH* + OH* \longleftrightarrow RCH_2O* + H_2O*$	0.05		

Table 2.6 (continued)

$RCH_2OH* + O_2* \leftrightarrow RCH_2O* + OOH*$	0.44		
$RCH_2OH* + * \leftrightarrow RCHOH* + H*$	−0.05	0.63	0.58
$RCH_2OH* + O* \leftrightarrow RCHOH* + OH*$	−0.43	0.86	1.29
$RCH_2OH* + OH* \leftrightarrow RCHOH* + H_2O*$	−0.56	0.94	1.50
$RCH_2O* + * \leftrightarrow RCHO* + H*$	−0.75	0.31	1.06
$RCH_2O* + O* \leftrightarrow RCHO* + OH*$	−1.13	0.65	1.78
$RCH_2O* + OH* \leftrightarrow RCHO* + H_2O*$	−1.25	0.83	2.08
$RCHOH* + * \leftrightarrow RCHO* + H*$	−0.14	1.04	1.18
$RCHOH* + O* \leftrightarrow RCHO* + OH*$	−0.52		
$RCHOH* + OH* \leftrightarrow RCHO* + H_2O*$	−0.64		
$RCHOH* + O_2* \leftrightarrow RCHO* + OOH*$	−0.26		
$RCHO* \leftrightarrow RCHO_{(sol'n)} + *$	−0.07		
$RCHO* + * \leftrightarrow RCO* + H*$	−0.30		
$RCO* + CH_3O* \leftrightarrow RCOOCH_3* + *$	−1.27	0.55	1.82
$RCHO_{(sol'n)} + CH_3O^-_{(sol'n)} \leftrightarrow RCHOOCH^-_{3(sol'n)}$	−0.20		
$RCHOOCH^-_{3(sol'n)} + * \leftrightarrow RCHOOCH_3* + e^-$	−0.24		
$RCHOOCH_3* + * \leftrightarrow RCOOCH_3* + H*$	−1.11		
$RCHOOCH_3* + O* \leftrightarrow RCOOCH_3* + OH*$	−1.49	0.69	2.18
$RCOOCH_3* \leftrightarrow RCOOCH_{3(sol'n)} + *$	0.20		
$O_2* + * \leftrightarrow 2\,O*$	−1.59	0.94	2.53
$O_2* + H* \leftrightarrow OOH* + *$	−0.12	0.79	0.91
$OOH* + * \leftrightarrow O* + OH*$	−1.85	0.10	1.95
$O* + H* \leftrightarrow OH* + *$	−0.38	0.55	0.93

Table 2.6 (continued)

$OH* + H* \leftrightarrow H_2O* + *$	−0.51	0.86	1.37
$2\,OH* \leftrightarrow H_2O* + O*$	0.12	0.47	0.59
$OH* + e^- \leftrightarrow OH^-_{(sol'n)} + *$	−0.08		
$H_2O* \leftrightarrow H_2O_{(sol'n)} + *$	−0.15		
$CH_3O* + H* \leftrightarrow CH_3OH* + *$	−0.47	0.80	1.27
$CH_3OH* + O* \leftrightarrow CH_3O* + OH*$	0.09	0.44	0.35
$CH_3OH* + OH* \leftrightarrow CH_3O* + H_2O*$	−0.03		
$CH_3OH* + O_2* \leftrightarrow CH_3O* + OOH*$	0.41		
$CH_3OH* \leftrightarrow CH_3OH_{(l)} + *$	−0.04		
$2\,H* \leftrightarrow H_{2(sol'n)} + 2*$	0.82		
$H* + O_2* + CH_3OH_{(l)} \leftrightarrow OOH* + CH_3OH$	−0.12	0.43	0.55
$RCHOOCH_3*^{Te} + * \leftrightarrow RCHOOCH_3* + *^{Te}$	−0.42	0.37	0.79
$RCHOOCH^-_{3(sol'n)} + *^{Te} \leftrightarrow RCHOOCH_3*^{Te} + e^-$	0.19		
$RCHOH*^{Te} + * \leftrightarrow RCHOH* + *^{Te}$	−0.61	0.16	0.77
$CH_3OH*^{Te} + * \leftrightarrow CH_3OH* + *^{Te}$	−0.16		
$CH_3OH_{(sol'n)} + *^{Te} \leftrightarrow CH_3OH*^{Te}$	0.21		
$CH_3O*^{Te} + * \leftrightarrow CH_3O* + *^{Te}$	−0.46	0.26	0.62
$RCH_3O^-_{(sol'n)} + *^{Te} \leftrightarrow RCH_3O*^{Te} + e^-$	0.41		
$O_2*^{Te} + * \leftrightarrow O_2* + *^{Te}$	−0.88		
$O_{2(g)} + *^{Te} \leftrightarrow O_2*^{Te}$	0.86		
$O*^{Te} + * \leftrightarrow O* + *^{Te}$	−0.79	0.21	1.00
$O_2*^{Te} + * \leftrightarrow O* + O*^{Te}$	−1.69	0.59	2.28
$OH*^{Te} + * \leftrightarrow OH* + *^{Te}$	−0.54	0.29	0.83

Table 2.6 (continued)

$OH^-_{(sol'n)} + *^{Te} \longleftrightarrow OH*^{Te} + e^-$	0.86		
$OOH*^{Te} + * \longleftrightarrow OOH* + *^{Te}$	−0.52	0.12	0.64
$RCHO*^{Te} + * \longleftrightarrow RCHO* + *^{Te}$	0.05		
$RCHO(sol'n) + *^{Te} \longleftrightarrow RCHO*^{Te}$	0.07		
$RCH_2OH*^{Te} + * \longleftrightarrow RCH_2OH* + *^{Te}$	−0.02		
$RCH_2OH(sol'n) + *^{Te} \longleftrightarrow RCH_2OH*^{Te}$	0.08		
$RCO*^{te} + * \longleftrightarrow RCO* + *^{Te}$	−0.73		
$RCH_2O*^{te} + * \longleftrightarrow RCH_2O* + *^{Te}$	−0.17		
$RCH_2O^-(sol'n) + *^{Te} \longleftrightarrow RCH_2O*^{Te}$	0.19		

Table 2.7: Steady state rate and Campbell's degree of rate control for all reactions considered in our model.

Reaction	Rate (s^{-1})	χ_{RC}
$RCH_2OH_{(sol'n)} + * \longleftrightarrow RCH_2OH*$	87.6	0.020
$RCH_2O^-_{(sol'n)} + * \longleftrightarrow RCH_2O* + e^-$	0.6	0.000
$CH_3O^-_{(sol'n)} + * \longleftrightarrow CH_3O* + e^-$	2.6	0.000
$O_{2(g)} + * \longleftrightarrow O_2*$	175.7	0.000
$RCH_2OH* + * \longleftrightarrow RCH_2O* + H*$	0.0	0.000
$RCH_2OH* + O* \longleftrightarrow RCH_2O* + OH*$	0.0	0.000
$RCH_2OH* + OH* \longleftrightarrow RCH_2O* + H_2O*$	175.2	0.002
$RCH_2OH* + O_2* \longleftrightarrow RCH_2O* + OOH*$	−0.1	0.000
$RCH_2OH* + * \longleftrightarrow RCHOH* + H*$	0.2	0.000
$RCH_2OH* + O* \longleftrightarrow RCHOH* + OH*$	0.0	0.000

Table 2.7 (continued)

$RCH_2OH* + OH* \leftrightarrow RCHOH* + H_2O*$	0.0	0.000
$RCH_2O* + * \leftrightarrow RCHO* + H*$	175.6	0.307
$RCH_2O* + O* \leftrightarrow RCHO* + OH*$	0.0	0.000
$RCH_2O* + OH* \leftrightarrow RCHO* + H_2O*$	0.0	0.000
$RCHOH* + * \leftrightarrow RCHO* + H*$	0.0	0.000
$RCHOH* + O* \leftrightarrow RCHO* + OH*$	0.1	0.000
$RCHOH* + OH* \leftrightarrow RCHO* + H_2O*$	0.0	0.000
$RCHOH* + O_2* \leftrightarrow RCHO* + OOH*$	0.1	0.000
$RCHO* \leftrightarrow RCHO_{(sol'n)} + *$	0.1	0.000
$RCHO* + * \leftrightarrow RCO* + H*$	175.5	0.000
$RCO* + CH_3O* \leftrightarrow RCOOCH_3* + *$	175.5	−0.259
$RCHO_{(sol'n)} + CH_3O^-_{(sol'n)} \leftrightarrow RCHOOCH^-_{3(sol'n)}$	0.0	0.000
$RCHOOCH^-_{3(sol'n)} + * \leftrightarrow RCHOOCH_3* + e^-$	0.0	0.000
$RCHOOCH_3* + * \leftrightarrow RCOOCH_3* + H*$	0.0	0.000
$RCHOOCH_3* + O* \leftrightarrow RCOOCH_3* + OH*$	0.0	0.000
$RCOOCH_3* \leftrightarrow RCOOCH_{3(sol'n)} + *$	175.5	0.326
$O_2* + * \leftrightarrow 2\,O*$	0.0	0.000
$O_2* + H* \leftrightarrow OOH* + *$	0.0	0.000
$OOH* + * \leftrightarrow O* + OH*$	175.7	0.283
$O* + H* \leftrightarrow OH* + *$	0.1	0.000
$OH* + H* \leftrightarrow H_2O* + *$	0.0	0.000
$2\,OH* \leftrightarrow H_2O* + O*$	0.0	0.000
$OH* + e^- \leftrightarrow OH^-_{(sol'n)} + *$	3.2	0.000

Table 2.7 (continued)

$H_2O* \longleftrightarrow H_2O_{(sol'n)} + *$	348.1	0.002
$CH_3O* + H* \longleftrightarrow CH_3OH* + *$	0.0	0.000
$CH_3OH* + O* \longleftrightarrow CH_3O* + OH*$	175.5	0.004
$CH_3OH* + OH* \longleftrightarrow CH_3O* + H_2O*$	172.9	0.000
$CH_3OH* + O_2* \longleftrightarrow CH_3O* + OOH*$	−175.6	−0.005
$CH_3OH* \longleftrightarrow CH_3OH_{(l)} + *$	−86.4	0.001
$2\,H* \longleftrightarrow H_{2(sol'n)} + 2* $	0.0	0.000
$H* + O_2* + CH_3OH_{(l)} \longleftrightarrow OOH* + CH_3OH$	351.2	0.079
$RCHOOCH_3*^{Te} + * \longleftrightarrow RCHOOCH_3* + *^{Te}$	0.0	0.000
$RCHOOCH^-_{3(sol'n)} + *^{Te} \longleftrightarrow RCHOOCH_3*^{Te} + e^-$	0.0	0.000
$RCHOH*^{Te} + * \longleftrightarrow RCHOH* + *^{Te}$	0.0	0.000
$CH_3OH*^{Te} + * \longleftrightarrow CH_3OH* + *^{Te}$	86.4	0.000
$CH_3OH_{(sol'n)} + *^{Te} \longleftrightarrow RCH_3OH*^{Te}$	86.4	0.000
$CH_3O*^{Te} + * \longleftrightarrow CH_3O* + *^{Te}$	0.0	0.000
$RCH_3O^-_{(sol'n)} + *^{Te} \longleftrightarrow RCH_3O*^{Te} + e^-$	0.0	0.000
$O_2*^{Te} + * \longleftrightarrow O_2* + *^{Te}$	0.0	0.000
$O_{2(g)} + *^{Te} \longleftrightarrow O_2*^{Te}$	0.0	0.000
$O*^{Te} + * \longleftrightarrow O* + *^{Te}$	0.0	0.000
$O_2*^{Te} + * \longleftrightarrow O* + O*^{Te}$	0.0	0.000
$OH*^{Te} + * \longleftrightarrow OH* + *^{Te}$	0.0	0.000
$OH^-_{(sol'n)} + *^{Te} \longleftrightarrow OH*^{Te} + e^-$	0.0	0.000
$OOH*^{Te} + * \longleftrightarrow OOH* + *^{Te}$	0.0	0.000
$RCHO*^{Te} + * \longleftrightarrow RCHO* + *^{Te}$	−0.14	0.000

Table 2.7 (continued)

$RCHO(sol'n) + *^{Te} \leftrightarrow RCHO*^{Te}$	−0.14	0.000
$RCH_2OH*^{Te} + * \leftrightarrow RCH_2OH* + *^{Te}$	87.6	0.020
$RCH_2OH(sol'n) + *^{Te} \leftrightarrow RCH_2OH*^{T}e$	87.6	0.000
$RCO*^{Te} + * \leftrightarrow RCO* + *^{Te}$	0.0	0.000
$RCH_2O*^{Te} + * \leftrightarrow RCH_2O* + *^{Te}$	0.0	0.000
$RCH_2O^{-}(sol'n) + *^{Te} \leftrightarrow RCH_2O*^{Te}$	0.0	0.000

In table 2.5 and table 2.6 are the free energies of reactions and barriers for all reaction in the two site PdTe(111) microkinetic model on a pristine surface and at steady state, respectively. In table 2.7, are the rates of each reaction at steady state and Campbell's degree of rate control. In table 2.8 are the surface concentrations and thermodynamic rate control of all species. The microkinetic model has a TOF of 175.5 s^{-1}.

The microkinetic model for the two site PdTe(111) promoted catalyst shows increase activity compared to the unpromoted Pd(111) catalyst. The TOF increased 12.9 times (from 13.6 s^{-1} to 175.5 s^{-1}). The main reaction pathway, depicted in figure 2.3, remains the same. Flux through the reaction network is significantly increased, as seen in table 2.7.

The pathway to reduce O_2* has changed. Instead of propanol and propoxy participating in the cycle to reform O_2*, methanol and methoxy perform this function, as shown in figure 2.9. This can be attributed to the change in energetics of the reaction of methanol* and O* to form methoxy* and OH*, which is an important step in the oxygen reduction cycle. On the unpromoted Pd(111) catalyst, this reaction is uphill by 0.54 eV at steady state coverage. However, on the one-site PdTe(111) promoted catalyst, this reaction is only uphill by 0.09 eV. Lowering the barrier to form methoxy from methanol on the surface allows the O_2 re-

Table 2.8: Steady state concentrations and degree of thermodynamic rate control for all adsorbates considered in our PdTe(111) model.

Species	Coverage	χ_{TRC}
H	0.0038	0.070
RCH_2OH	0.0036	0.013
$RCOOCH_3$	0.5026	−0.669
CH_3OH	0.1520	−0.971
CH_3O	0.0500	−0.050
RCO	0.1302	0.018
O_2	0.0023	0.065
RCHO	< 0.0001	0.142
$RCHOOCH_3$	< 0.0001	0.000
RCHOH	< 0.0001	0.000
H_2O	0.0001	0.003
O	0.0011	0.020
RCH_2O	0.0001	0.484
OOH	< 0.0001	0.602
OH	< 0.0001	0.031
$*$	0.0292	
$RCHOOCH_3{}^{*\mathrm{Te}}$	< 0.0001	0.000
$RCHOH^{*\mathrm{Te}}$	< 0.0001	0.000
$CH_3OH^{*\mathrm{Te}}$	0.0020	0.000
$RCO^{*\mathrm{Te}}$	< 0.0001	0.000
$O^{*\mathrm{Te}}$	< 0.0001	0.000
$O_2{}^{*\mathrm{Te}}$	< 0.0001	0.000
$*$ Te	0.116	

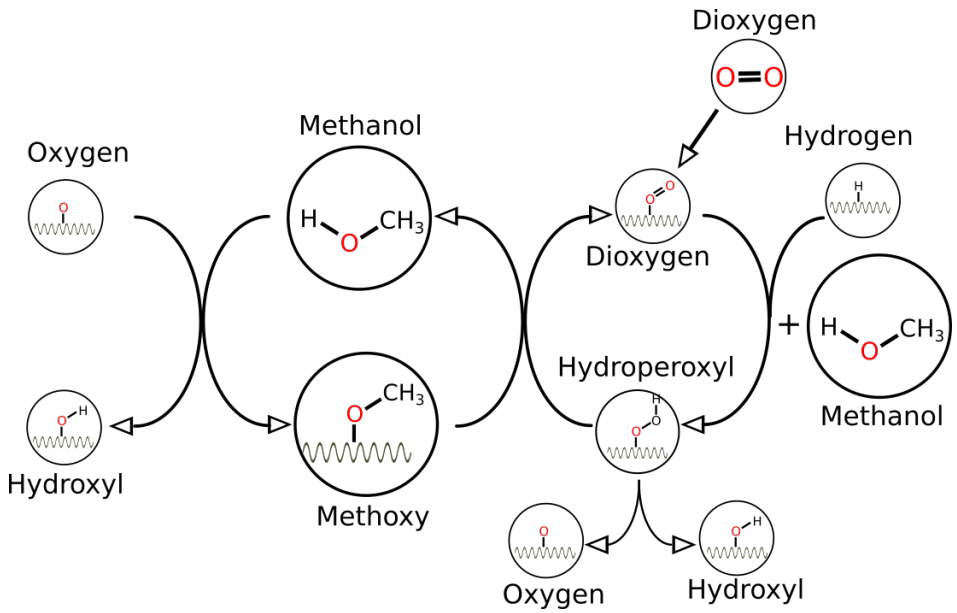

Figure 2.9: Pathway for O_2 reduction on the PdTe one site model catalyst

duction cycle to occur more quickly and thus increase the speed of the reaction. Even though the barrier to solvent-assisted h-shuttling increased from 0.21 to 0.43 eV, the shift to using methanol/methoxy instead of propanol/propoxy still allows this cycle to be more active. The degree of rate control for decomposition of OOH* to O* and OH* decreased in degree of rate control from 0.50 to 0.28, even though this barrier increased modestly by 0.03 eV.

C-H bond scission to form propanal* and H* from propoxy* is still the reaction on the main reaction pathway with the highest degree of rate control. However, the degree of rate control decreased from 0.48 to 0.31 and the barrier for this reaction at steady state decreased from 0.37 eV on the unpromoted catalyst to 0.31 eV on the Te promoted catalyst.

While the mechanism is largely unchanged, the PdTe(111) promoted catalyst has a very different surface coverage. Instead of being poisoned by the reactants methanol and propanol, the promoted catalyst is covered by methanol (15.2%), methyl propionate (50.3%) and propanoyl (13.0%). Note, that since each methyl propionate occupies two sites, buildup of this high a

concentration (above the 40% build up allowed by the dE_{bulky} parameter defined in Equation 2.7). Additionally instead of less than 0.1% sites open, 2.3% of palladium sites and 11.6% of tellurium sites are now open.

We see no reaction flux through the only reaction that broke a bond across a Te and a Pd site, the breaking of O_2*^{Te} to form O bound to palladium and O bound to tellurium, which indicates that the formation of unique reaction sites (ensemble effect) by alloying the Pd with Te is not likely to be the mechanism of promotion.

Additionally, while we see adsorption of CH_3OH (methanol) and RCH_3OH (propanol) onto tellurium sites, we see 100% of the flux through these tellurium sites immediately diffuse to palladium sites. There is no buildup on tellurium sites and neither the adsorption or diffusion reactions have any degree of rate control. This indicates that this is not a bi-functional catalyst, with distinct reactions occur on distinct sites.

Finally, we do not see the poisoning of the surface due to a side reaction (such as accumulation of RCHOH (hydroxypropyl) or H atoms that the Te atoms could break up). Therefore, we conclude that the most likely promotion effect is the electronic effect, where the formation of an alloy changes the relative energetics of the possible pathways such that the overall reaction flux is faster.

One Site PdTe model results

If the main mechanism of promotion is an electronic effect, building a model with the reaction free energies and reaction barriers calculated for the PdTe(111) two site model but with only *one* binding site, i.e. no distinction between Te or Pd sites, we should capture the same pathway and TOF as the PdTe(111) two-site model. As the palladium site is the more energetically favorable adsorption site for all species, the two-site model reduces to the one-site model in the limit of infinitely fast diffusion and zero flux through reactions involving both Te and Pd

sites.

Reaction free energies and barriers for reactions in the PdTe(111) one-site model at steady state are found in Table 2.9. Reaction free energies and barriers in pristine conditions for the one-site model are the same as for the two-site model and can be found in Table 2.5. Reaction rates and degree of rate control can be found in Table 2.10. Species coverage and thermodynamic degree of rate control can be found in Table 2.11.

Table 2.9: Free energies of reaction and forward and reverse free energy barriers for the all reactions considered in the PdTe(111) one-site microkinetic model under steady state conditions. Missing values for $\Delta G^{\ddagger}_{\text{for}}$ and $\Delta G^{\ddagger}_{\text{rev}}$ indicate that the reaction is barrierless.

Reaction	ΔG (eV)	$\Delta G^{\ddagger}_{\text{for}}$ (eV)	$\Delta G^{\ddagger}_{\text{rev}}$ (eV)
$RCH_2OH_{(sol'n)} + * \leftrightarrow RCH_2OH*$	0.09		
$RCH_2O^-_{(sol'n)} + * \leftrightarrow RCH_2O* + e^-$	0.04		
$CH_3O^-_{(sol'n)} + * \leftrightarrow CH_3O* + e^-$	−0.04		
$O_{2(g)} + * \leftrightarrow O_2*$	−0.02		
$RCH_2OH* + * \leftrightarrow RCH_2O* + H*$	0.57	1.29	0.72
$RCH_2OH* + O* \leftrightarrow RCH_2O* + OH*$	0.18	0.75	0.57
$RCH_2OH* + OH* \leftrightarrow RCH_2O* + H_2O*$	0.05		
$RCH_2OH* + O_2* \leftrightarrow RCH_2O* + OOH*$	0.44		
$RCH_2OH* + * \leftrightarrow RCHOH* + H*$	−0.04	0.63	0.67
$RCH_2OH* + O* \leftrightarrow RCHOH* + OH*$	−0.44	0.86	1.20
$RCH_2OH* + OH* \leftrightarrow RCHOH* + H_2O*$	−0.56	0.94	1.50
$RCH_2O* + * \leftrightarrow RCHO* + H*$	−0.74	0.32	0.96
$RCH_2O* + O* \leftrightarrow RCHO* + OH*$	−1.13	0.65	1.78
$RCH_2O* + OH* \leftrightarrow RCHO* + H_2O*$	−1.25	0.83	2.08
$RCHOH* + * \leftrightarrow RCHO* + H*$	−0.12	1.04	1.16

Table 2.9 (continued)

$RCHOH* + O* \leftrightarrow RCHO* + OH*$	−0.51		
$RCHOH* + OH* \leftrightarrow RCHO* + H_2O*$	−0.64		
$RCHOH* + O_2* \leftrightarrow RCHO* + OOH*$	−0.26		
$RCHO* \leftrightarrow RCHO_{(sol'n)} + *$	−0.10		
$RCHO* + * \leftrightarrow RCO* + H*$	−0.30		
$RCO* + CH_3O* \leftrightarrow RCOOCH_3* + *$	−1.28	0.56	1.84
$RCHO_{(sol'n)} + CH_3O^-_{(sol'n)} \leftrightarrow RCHOOCH^-_{3(sol'n)}$	−0.20		
$RCHOOCH^-_{3(sol'n)} + * \leftrightarrow RCHOOCH_3* + e^-$	−0.22		
$RCHOOCH_3* + * \leftrightarrow RCOOCH_3* + H*$	−1.11		
$RCHOOCH_3* + O* \leftrightarrow RCOOCH_3* + OH*$	−1.49	0.69	2.18
$RCOOCH_3* \leftrightarrow RCOOCH_{3(sol'n)} + *$	0.17		
$O_2* + * \leftrightarrow 2\,O*$	−1.59	0.94	2.53
$O_2* + H* \leftrightarrow OOH* + *$	−0.14	0.77	0.91
$OOH* + * \leftrightarrow O* + OH*$	−1.85	0.10	1.95
$O* + H* \leftrightarrow OH* + *$	−0.40	0.54	0.94
$OH* + H* \leftrightarrow H_2O* + *$	−0.52	0.86	1.38
$2\,OH* \leftrightarrow H_2O* + O*$	0.12	0.71	0.59
$OH* + e^- \leftrightarrow OH^-_{(sol'n)} + *$	−0.05		
$H_2O* \leftrightarrow H_2O_{(sol'n)} + *$	0.15		
$CH_3O* + H* \leftrightarrow CH_3OH* + *$	−0.52	0.77	1.29
$CH_3OH* + O* \leftrightarrow CH_3O* + OH*$	0.12	0.45	0.33
$CH_3OH* + OH* \leftrightarrow CH_3O* + H_2O*$	0.00		
$CH_3OH* + O_2* \leftrightarrow CH_3O* + OOH*$	0.38		

Table 2.9 (continued)

$CH_3OH* \longleftrightarrow CH_3OH_{(l)} + *$	-0.04		
$2\,H* \longleftrightarrow H_{2(sol'n)} + 2*$	0.80		
$H* + O_2* + CH_3OH_{(l)} \longleftrightarrow OOH* + CH_3OH$	-0.14	0.43	0.57

Table 2.10: Steady state rate and Campbell's degree of rate control for all reactions considered in our one site PdTe(111) model.

Reaction	Rate (s^{-1})	χ_{RC}
$RCH_2OH_{(sol'n)} + * \longleftrightarrow RCH_2OH*$	225.7	0.116
$RCH_2O^-_{(sol'n)} + * \longleftrightarrow RCH_2O* + e^-$	1.3	0.001
$CH_3O^-_{(sol'n)} + * \longleftrightarrow CH_3O* + e^-$	2.9	0.000
$O_{2(g)} + * \longleftrightarrow O_2*$	227.0	0.000
$RCH_2OH* + * \longleftrightarrow RCH_2O* + H*$	0.0	0.000
$RCH_2OH* + O* \longleftrightarrow RCH_2O* + OH*$	0.0	0.000
$RCH_2OH* + OH* \longleftrightarrow RCH_2O* + H_2O*$	175.2	0.002
$RCH_2OH* + O_2* \longleftrightarrow RCH_2O* + OOH*$	-0.2	0.000
$RCH_2OH* + * \longleftrightarrow RCHOH* + H*$	0.1	0.000
$RCH_2OH* + O* \longleftrightarrow RCHOH* + OH*$	0.0	0.000
$RCH_2OH* + OH* \longleftrightarrow RCHOH* + H_2O*$	0.0	0.000
$RCH_2O* + * \longleftrightarrow RCHO* + H*$	226.9	0.288
$RCH_2O* + O* \longleftrightarrow RCHO* + OH*$	0.0	0.000
$RCH_2O* + OH* \longleftrightarrow RCHO* + H_2O*$	0.0	0.000
$RCHOH* + * \longleftrightarrow RCHO* + H*$	0.0	0.000
$RCHOH* + O* \longleftrightarrow RCHO* + OH*$	0.1	0.000

Table 2.10 (continued)

$RCHOH* + OH* \leftrightarrow RCHO* + H_2O*$	0.0	0.000
$RCHOH* + O_2* \leftrightarrow RCHO* + OOH*$	0.1	0.000
$RCHO* \leftrightarrow RCHO_{(sol'n)} + *$	0.1	0.000
$RCHO* + * \leftrightarrow RCO* + H*$	226.9	0.000
$RCO* + CH_3O* \leftrightarrow RCOOCH_3* + *$	226.9	−0.082
$RCHO_{(sol'n)} + CH_3O^-_{(sol'n)} \leftrightarrow RCHOOCH^-_{3(sol'n)}$	0.0	0.000
$RCHOOCH^-_{3(sol'n)} + * \leftrightarrow RCHOOCH_3* + e^-$	0.0	0.000
$RCHOOCH_3* + * \leftrightarrow RCOOCH_3* + H*$	0.0	0.000
$RCHOOCH_3* + O* \leftrightarrow RCOOCH_3* + OH*$	0.0	0.000
$RCOOCH_3* \leftrightarrow RCOOCH_{3(sol'n)} + *$	226.9	−0.296
$O_2* + * \leftrightarrow 2\,O*$	0.0	0.000
$O_2* + H* \leftrightarrow OOH* + *$	0.0	0.000
$OOH* + * \leftrightarrow O* + OH*$	227	0.276
$O* + H* \leftrightarrow OH* + *$	0.1	0.000
$OH* + H* \leftrightarrow H_2O* + *$	0.0	0.000
$2\,OH* \leftrightarrow H_2O* + O*$	0.0	0.000
$OH* + e^- \leftrightarrow OH^-_{(sol'n)} + *$	4.2	0.000
$H_2O* \leftrightarrow H_2O_{(sol'n)} + *$	449.8	0.001
$CH_3O* + H* \leftrightarrow CH_3OH* + *$	0.0	0.000
$CH_3OH* + O* \leftrightarrow CH_3O* + OH*$	226.8	0.003
$CH_3OH* + OH* \leftrightarrow CH_3O* + H_2O*$	224.0	0.000
$CH_3OH* + O_2* \leftrightarrow CH_3O* + OOH*$	−226.7	−0.007
$CH_3OH* \leftrightarrow CH_3OH_{(l)} + *$	−224	−0.006

Table 2.10 (continued)

$2\,H* \longleftrightarrow H_{2(sol'n)} + 2*$	0.0	0.000
$H* + O_2* + CH_3OH_{(l)} \longleftrightarrow OOH* + CH_3OH$	453.8	0.043

Table 2.11: Steady state concentrations and degree of thermodynamic rate control for all adsorbates considered in our one-site PdTe(111) model.

Species	Coverage	χ_{TRC}
H	0.0024	0.096
RCH_2OH	0.0014	0.002
$RCOOCH_3$	0.5210	−0.597
CH_3OH	0.2424	−0.931
CH_3O	0.0558	−0.032
RCO	0.1247	0.006
O_2	0.0036	0.029
RCHO	$<$ 0.0001	0.134
$RCHOOCH_3$	$<$ 0.0001	0.000
RCHOH	$<$ 0.0001	0.000
H_2O	0.0002	0.002
O	0.0018	0.017
RCH_2O	0.0000	0.494
OOH	$<$ 0.0001	0.549
OH	$<$ 0.0001	0.029
*	0.0467	

We find a TOF of 226.9 s^{-1}. While this is faster than the two-site model, since we are now treating every site the same, and thus Te sites are treated as if they are Pd sites, we have notionally increased the total number of sites by 14.3% (87.5% of the sites on the two-site model were considered Pd binding sites). The main reaction pathway as well as the oxygen oxidation pathway are the same as the two-site model. The rate limiting steps remain ester desorption, breaking the O-O bond in bound OOH and breaking the C-H bond in bond propoxy to form

the aldehyde propanal. The flux through the adsorption of methanol and propanol onto Te sites and subsequent diffusion to Pd sites simply shifted to direct adsorption onto the Pd site. We conclude that the one-site model that only accounts for electronic effects captures all the promotional effects seen in the two-site model compared to the unpromoted model.

Modify Three Binding Energies to capture main electronic effect

In order to identify which energetic changes are most responsible for the electronic promotional effect of alloyed tellurium, we look at which species and reactions have the highest χ_{TRC} and χ_{RC} respectively.

The species with both the largest χ_{TRC} *and* the largest *change* in TRC was methanol (changing from -2.93 to -0.92). Additionally, the reaction with the largest changes in χ_{RC} along the main reaction pathway is the reaction of RCH_2O (propoxy) forming RCHO (propanal) and H. Therefore, we modified the binding energies of methanol, propoxide and propanal on the Pd(111) surface to match that of the promoted PdTe(111) surface at zero coverage. The binding energy of propoxy was weakened by 0.13 eV, propanal by 0.11 eV and methanol by 0.17 eV. As any changes in energetics to reactants or products are propagated to the transition state through Brønsted-Evans-Polanyi relations (see Chapter 1.4.2) the transition state energies for any reactions involving methanol, propoxy and propanal will change accordingly. All other energetics were left unchanged.

The reaction free energies and reaction barriers at steady state for the modified unpromoted model are in Table 2.12. The energetics on the pristine surface are the same as for the unpromoted microkinetic model listed in Table 2.2 except for any reaction involving propanal, methanol or propoxy which will be weakened by 0.11 eV, 0.17 eV and 0.13 eV respectively. The rates of reactions and degree of rate control are in Table 2.13. Species coverage and thermodynamic degree of rate control are in Table 2.14.

Table 2.12: Free energies of reaction and forward and reverse free energy barriers for the all reactions considered in the PdTe(111) one-site microkinetic model under steady state conditions. Missing values for $\Delta G^{\ddagger}_{\text{for}}$ and $\Delta G^{\ddagger}_{\text{rev}}$ indicate that the reaction is barrierless.

Reaction	ΔG (eV)	$\Delta G^{\ddagger}_{\text{for}}$ (eV)	$\Delta G^{\ddagger}_{\text{rev}}$ (eV)
$RCH_2OH_{(sol'n)} + * \longleftrightarrow RCH_2OH*$	0.27		
$RCH_2O^-_{(sol'n)} + * \longleftrightarrow RCH_2O* + e^-$	0.02		
$CH_3O^-_{(sol'n)} + * \longleftrightarrow CH_3O* + e^-$	−0.10		
$O_{2(g)} + * \longleftrightarrow O_2*$	0.06		
$RCH_2OH* + * \longleftrightarrow RCH_2O* + H*$	0.73	1.38	0.65
$RCH_2OH* + O* \longleftrightarrow RCH_2O* + OH*$	0.15		
$RCH_2OH* + OH* \longleftrightarrow RCH_2O* + H_2O*$	0.12		
$RCH_2OH* + O_2* \longleftrightarrow RCH_2O* + OOH*$	0.35		
$RCH_2OH* + * \longleftrightarrow RCHOH* + H*$	0.01	0.67	0.66
$RCH_2OH* + O* \longleftrightarrow RCHOH* + OH*$	−0.57	0.77	1.34
$RCH_2O* + * \longleftrightarrow RCHO* + H*$	−0.75	0.31	1.56
$RCH_2O* + O* \longleftrightarrow RCHO* + OH*$	−1.33	0.64	1.97
$RCH_2O* + OH* \longleftrightarrow RCHO* + H_2O*$	−1.36	0.60	1.96
$RCHOH* + * \longleftrightarrow RCHO* + H*$	−0.03	0.69	0.72
$RCHOH* + O* \longleftrightarrow RCHO* + OH*$	−0.61		
$RCHOH* + OH* \longleftrightarrow RCHO* + H_2O*$	−0.65		
$RCHOH* + O_2* \longleftrightarrow RCHO* + OOH*$	−0.42		
$RCHO* \longleftrightarrow RCHO_{(sol'n)} + *$	−0.27		
$RCHO* + * \longleftrightarrow RCO* + H*$	−0.82	0.10	0.92
$RCO* + CH_3O* \longleftrightarrow RCOOCH_3* + *$	−1.09	0.16	1.25

Table 2.12 (continued)

$RCHO_{(sol'n)} + CH_3O^-_{(sol'n)} \leftrightarrow RCHOOCH^-_{3(sol'n)}$	−0.20		
$RCHOOCH^-_{3(sol'n)} + * \leftrightarrow RCHOOCH_3* + e^-$	−0.41		
$RCHOOCH_3* + * \leftrightarrow RCOOCH_3* + H*$	−1.12	0.43	−1.55
$RCHOOCH_3* + O* \leftrightarrow RCOOCH_3* + OH*$	−1.74	1.11	2.85
$RCOOCH_3* \leftrightarrow RCOOCH_{3(sol'n)} + *$	0.19		
$O_2* + * \leftrightarrow 2\,O*$	−1.26	1.02	2.28
$O_2* + H* \leftrightarrow OOH* + *$	−0.39	0.37	1.02
$OOH* + * \leftrightarrow O* + OH*$	−1.46	0.08	1.54
$O* + H* \leftrightarrow OH* + *$	−0.58	0.73	1.31
$OH* + H* \leftrightarrow H_2O* + *$	−0.61	0.77	1.38
$2\,OH* \leftrightarrow H_2O* + O*$	0.03	0.66	0.63
$OH* + e^- \leftrightarrow OH^-_{(sol'n)} + *$	0.13		
$H_2O* \leftrightarrow H_2O_{(sol'n)} + *$	−0.03		
$CH_3O* + H* \leftrightarrow CH_3OH* + *$	−0.63	0.83	1.16
$CH_3OH* + O* \leftrightarrow CH_3O* + OH*$	0.05		
$CH_3OH* + OH* \leftrightarrow CH_3O* + H_2O*$	0.01		
$CH_3OH* + O_2* \leftrightarrow CH_3O* + OOH*$	0.38		
$CH_3OH* \leftrightarrow CH_3OH_{(l)} + *$	0.24		
$_2H* \leftrightarrow H_{2(sol'n)} + {}_2*$	0.83		
$H* + O_2* + CH_3OH_{(l)} \leftrightarrow OOH* + CH_3OH$	−0.39	0.30	0.69

Table 2.13: Steady state rate and Campbell's degree of rate control for all reactions considered in our one modified unpromoted microkinetic model.

Reaction	Rate (s^{-1})	χ_{RC}
$RCH_2OH_{(sol'n)} + * \longleftrightarrow RCH_2OH*$	225.5	0.132
$RCH_2O^-_{(sol'n)} + * \longleftrightarrow RCH_2O* + e^-$	1.1	0.001
$CH_3O^-_{(sol'n)} + * \longleftrightarrow CH_3O* + e^-$	−5.5	0.000
$O_{2(g)} + * \longleftrightarrow O_2*$	226.6	0.000
$RCH_2OH* + * \longleftrightarrow RCH_2O* + H*$	0.0	0.000
$RCH_2OH* + O* \longleftrightarrow RCH_2O* + OH*$	162.6	0.000
$RCH_2OH* + OH* \longleftrightarrow RCH_2O* + H_2O*$	63.0	0.000
$RCH_2OH* + O_2* \longleftrightarrow RCH_2O* + OOH*$	0.0	0.000
$RCH_2OH* + * \longleftrightarrow RCHOH* + H*$	0.0	0.000
$RCH_2OH* + O* \longleftrightarrow RCHOH* + OH*$	0.0	0.000
$RCH_2O* + * \longleftrightarrow RCHO* + H*$	226.6	0.344
$RCH_2O* + O* \longleftrightarrow RCHO* + OH*$	0.0	0.000
$RCH_2O* + OH* \longleftrightarrow RCHO* + H_2O*$	0.0	0.000
$RCHOH* + * \longleftrightarrow RCHO* + H*$	0.0	0.000
$RCHOH* + O* \longleftrightarrow RCHO* + OH*$	0.0	0.000
$RCHOH* + OH* \longleftrightarrow RCHO* + H_2O*$	0.0	0.000
$RCHOH* + O_2* \longleftrightarrow RCHO* + OOH*$	0.0	0.000
$RCHO* \longleftrightarrow RCHO_{(sol'n)} + *$	8.7	0.000
$RCHO* + * \longleftrightarrow RCO* + H*$	217.9	0.000
$RCO* + CH_3O* \longleftrightarrow RCOOCH_3* + *$	217.9	0.000
$RCHO_{(sol'n)} + CH_3O^-_{(sol'n)} \longleftrightarrow RCHOOCH^-_{3(sol'n)}$	8.7	0.000

Table 2.13 (continued)

$RCHOOCH^-_{3(sol'n)} + * \longleftrightarrow RCHOOCH_3* + e^-$	8.7	0.000
$RCHOOCH_3* + * \longleftrightarrow RCOOCH_3* + H*$	1.6	0.000
$RCHOOCH_3* + O* \longleftrightarrow RCOOCH_3* + OH*$	7.2	0.000
$RCOOCH_3* \longleftrightarrow RCOOCH_{3(sol'n)} + *$	226.6	−0.332
$O_2* + * \longleftrightarrow 2\,O*$	0.0	0.000
$O_2* + H* \longleftrightarrow OOH* + *$	0.0	0.000
$OOH* + * \longleftrightarrow O* + OH*$	226.6	0.183
$O* + H* \longleftrightarrow OH* + *$	0.0	0.000
$OH* + H* \longleftrightarrow H_2O* + *$	0.0	0.000
$2\,OH* \longleftrightarrow H_2O* + O*$	0.0	0.000
$OH* + e^- \longleftrightarrow OH^-_{(sol'n)} + *$	4.3	0.000
$H_2O* \longleftrightarrow H_2O_{(sol'n)} + *$	448.9	0.021
$CH_3O* + H* \longleftrightarrow CH_3OH* + *$	9.5	0.000
$CH_3OH* + O* \longleftrightarrow CH_3O* + OH*$	56.9	0.000
$CH_3OH* + OH* \longleftrightarrow CH_3O* + H_2O*$	386.0	0.000
$CH_3OH* + O_2* \longleftrightarrow CH_3O* + OOH*$	−209.9	−0.001
$CH_3OH* \longleftrightarrow CH_3OH_{(l)} + *$	−223.4	−0.004
$_2H* \longleftrightarrow H_{2(sol'n)} + {}_2*$	0.0	0.000
$H* + O_2* + CH_3OH_{(l)} \longleftrightarrow OOH* + CH_3OH$	436.6	0.006

Running the microkinetic model for the modified Pd(111) surface, we find that the TOF is 226.6 s^{-1} or a 16.7x speedup compared to the Pd(111) unpromoted model simply by changing three binding energies. This is also almost exactly the same TOF as the PdTe(111) one-site

Table 2.14: Steady state concentrations and degree of thermodynamic rate control for all adsorbates considered in our modified unpromoted Pd(111) model.

Species	Coverage	χ_{TRC}
H	0.0006	0.143
RCH_2OH	0.0015	−0.004
$RCOOCH_3$	0.3898	−0.597
CH_3OH	0.1657	−0.399
CH_3O	0.2650	−0.257
RCO	0.0000	0.000
O_2	0.000 01	0.007
RCHO	< 0.0001	0.147
$RCHOOCH_3$	< 0.0001	0.000
RCHOH	< 0.0001	0.000
H_2O	0.0060	−0.006
O	0.1238	−0.007
RCH_2O	0.0001	0.522
OOH	< 0.0001	0.344
OH	0.0153	0.000
$*$	0.0319	

model, which has a TOF of 226.9 s^{-1}

The major reaction pathway is the same, as expected. We find that the reaction of methanol* with O* to form methoxy* and OH* has a barrier of 0.05 eV (more similar to the PdTe(111) promoted system barrier of 0.150 than the unpromoted system of 0.54 eV). Therefore, the O_2 reduction cycle occurs with methanol and methoxy instead of propanol and propoxy. Additionally the barrier for C-H bond scission (the major rate limiting step) is 0.31 eV (closer to the 0.32 eV of the promoted PdTe(111) catalyst than the 0.37 eV barrier of the unpromoted Pd(111) catalyst). The surface coverage of the modified unpromoted surface is also more similar to the PdTe(111) one-site model than the unpromoted model. While the promoted model is poisoned with RCH_3OH and CH_3OH (61.84% of the surface), with almost no free sites to undergo the reaction (0.03% sites available), the PdTe(111) one-site model found no buildup of RCH_3OH, a significantly lower buildup of CH_3OH (24.24%), a minor buildup of the intermediate RCO and a high buildup of the final product along with 4.67% free sites. The modified unpromoted model had minor buildup of CH_3OH (16.57%) along with high buildup of the final product and minor buildup of methoxy. Finally the modified unpromoted model had 3.10% of free sites available, mirroring the PdTe(111) one-site promoted model rather than the unpromoted Pd(111) model.

Capturing these three energetic changes accounts for the majority of the changes between the unpromoted Pd(111) catalyst and the promoted PdTe(111) catalyst, including the increase in TOF, the change of mechanism and the surface coverage and is consistent with our conclusion that the effect of Te is electronic.

2.4 Conclusion

Utilizing our microkinetic modeling package Micki (described in Chapter 1) and high level DFT calculations, we built four microkinetic models to describe the aerobic esterification of primary alcohols to form methyl esters over a Pd(111) catalyst with and without Te promoters. These models account for important (and often neglected) factors, such as lateral surface interactions, solvent effects, charge buildup and diffusion-limited adsorption. The first microkinetic model, detailing the unpromoted Pd(111) reaction found that the reaction proceeds by first adsorping RCH_3OH (propanol), breaking first the O-H bond and then two C-H bonds to form RCO, which reacts with CH_3O on the surface to form the desired product. The surface is highly covered with propanol and methanol, with almost no free sites. The two major reaction limiting steps are breaking the first C-H bond and reducing O_2, which occurs through an O-assisted bond breaking of the O-H bond in propanol.

The second microkinetic model, a PdTe(111) two-site model, an alloy that described Pd and Te sites discretely and included all the reactions considered above on both Pd sites, Te sites and a mixture of the two. It concluded that the major reaction pathway is the same as described by the unpromoted model, but that the reaction proceeded 12.9 times faster. This is a due to a shift in the O_2 reduction mechanism from propanol and propoxy to methanol and methoxy. Additionally, the surface is no longer covered by the reactant propanol and the solvent methanol but rather by necessary reaction intermediates, such as propanoyl, or the final product, the methyl ester and a significant increase in free sites. As reactions directly including Te atoms are involved in the major reaction pathway, nor do they have any rate control, we conclude that the most likely mechanism of promotion is an electronic effect.

To test the electronic effect, we build a third microkinetic model, with all the energetics calculated on the PdTe(111) surface, but we do not considered the Pd and Te atoms to be distinct

binding sites, called the PdTe(111) one-site model. We find the same reaction pathway as well as the same mechanism for O_2 reduction as on the PdTe(111) two-site model. Additionally, while we find that the TOF is slightly faster than the PdTe(111) two-site model, this is because the number of active sites in nominally increased since the reaction was not proceeding on the distinct Te sites in the two-site model. This model upheld our conclusion that the electronic effect is responsible for Te promotion.

Finally, in order to pinpoint which specific electronic changes are most important for promotion we built a fourth microkinetic model that modified the binding energies of three species (RCHO, CH_3OH, and RCH_2O) in the unpromoted model. These three species had the highest degree of thermodynamic rate control and RCH_2O and RCHO are a reactant and a product, respectively, of the major rate controlling C-H bond scission step. The modified unpromoted microkinetic model had the same reaction pathway, O_2 reduction pathway, TOF and similar surface coverage (including the number of free sites) to the PdTe(111) one-site model.

In conclusion, the reaction pathway for the aerobic esterification of primary alcohols to methyl esters proceeds through the adsorption of RCH_3OH followed by the breaking of the O-H bond and then 2 C-H bonds and then a reaction with CH_3O to form the methyl ester ($RCOOCH_3$. The reaction rate is controlled by both the rate of breaking the first C-H bond and the pathway used for reducing O_2. The role of Te promoters is to modify the energetics of the reactions, specifically the energies of bound RCHO, CH_3OH, and RCH_2O.

3

Stable and Selective Electrosynthesis of H_2O_2 on Earth Abundant CoS_2 and $CoSe_2$ Catalysts

Reproduced in part with permission from Sheng, H., Janes, A. N., Ross, R. D., Kaiman, D., Huang, J., Song, B., Schmidt, J. R., Jin, S. (2020). *Stable and selective electrosynthesis of hydrogen peroxide and the electro-Fenton process on $CoSe_2$ polymorph catalysts*. Energy & Environmental Science. 2020, **13**, 4189-4203.

ANJ performed all theoretical modeling. Electrochemical experiments was performed by HS and RDR.

3.1 Introduction

Hydrogen peroxide (H_2O_2) is a versatile and green oxidant with a myriad of applications in industrial, environmental, healthcare, and household settings. It is among the list of disinfectants for use against SARS-CoV-2, a novel coronavirus that causes the COVID-19 pandemic.[179] The annual global production of H_2O_2 reached over 5 million tons in 2015 and has been steadily growing,[23] the majority of which is produced via the indirect anthraquinone process.[17]This energy- and waste-intensive multistep process relies on centralized chemical plants and produces up to 70 wt% concentrated solutions of H_2O_2, which are both hazardous and expensive to store and transport to end-users.[17] Although such centralized H_2O_2 production may benefit largescale industrial applications,[23] many distributed applications including water treatment, medical disinfection, and household sanitation require only very low concentrations of H_2O_2. For example, a concentration less than 1000 ppm (29 mM) is sufficient for water treatment.[196] This motivates alternative approaches to the direct and decentralized production of dilute H_2O_2 at the point of use.[196,71,137,141] While direct chemical synthesis of H_2O_2 from H_2 and O_2 gases could be a potential alternative production method, it still needs H_2 gas and must operate under large quantities of inert carrier gas and solvent due to flammability concerns, and very few noble metal alloy catalysts show satisfactory selectivity toward H_2O_2 production

as opposed to decomposition and/or further reduction to H_2O.[29,35]

Direct electrochemical synthesis of H_2O_2 from the two electron oxygen reduction reaction ($2e^-$ ORR) offers a more sustainable solution to decentralized manufacturing.[196,71,137,141] It can be driven by increasingly affordable renewable electricity[22,152] and eliminates the need for H_2 gas (which requires significant energy to produce from steam methane reforming and has a large carbon footprint[119]). The key challenge here is to develop robust electrocatalysts featuring high activity and selectivity toward the $2e^-$ (vs. the competing $4e^-$) ORR pathway. Defective[96,80,192] and heteroatom-doped[54,174,67] carbon materials have shown promise for the selective $2e^-$ ORR in alkaline solution ($O_2 + H_2O + 2\,e^- \longrightarrow HO_2^- + OH^-$, E = 0.76 V vs. RHE); however, H_2O_2 is unstable in base, especially at pH > 9.[141] The $2e^-$ ORR activities of carbon materials under acidic and neutral conditions are inferior to those under alkaline conditions, which is still the case after introducing transition metal single-atom coordination motifs into the carbon matrices.[72,173,74,177,41]

The electrosynthesis of H_2O_2 in acidic solution ($O_2 + 2\,H^+ + 2\,e^- \longrightarrow H_2O_2$, E^o = 0.69 V vs. RHE) would also be advantageous for on-site water disinfection and environmental treatment applications.[141] For example, the electro-Fenton process operates at an optimal pH of 3, where the electrogenerated H_2O_2 at the cathode reacts with Fe_2^+ and produces hydroxyl radicals ($^\bullet$OH) as an even more potent oxidant for the removal of a wide variety of persistent organic pollutants. Compared to the conventional chemical Fenton process, the electro-Fenton process not only avoids the transportation and storage of hazardous H_2O_2 but also features significantly enhanced $^\bullet$OH production rates and organic mineralization capabilities because of the rapid regeneration of Fe_2^+ at the cathode.[13] However, the cathode used for the electro-Fenton process has been almost exclusively carbon materials to date,[12] which suffer from insufficient catalytic activity for H_2O_2 production in acidic solution. The state-of the-art $2e^-$ ORR electrocatalysts under acidic conditions are based on noble metal alloys,[161,181] which are

not commercially viable as they involve expensive and/or toxic metals (such as Hg). Therefore, developing efficient and cost-effective $2e^-$ ORR catalysts for the electrosynthesis of H_2O_2 in acidic solution remains an important, but relatively underexplored target.

Theoretical modeling plays an important role in both identifying new potential catalysts as well as elucidating key physical principles to explain *why* these certain catalyst show superior performance in order to guide further experimental investigation.[125,47,199,169,78,48,172,147]

We utilize computational modeling to study a family of earth abundant electrocatalysts, CoX_2, where X is either sulfur or selenium. Cobalt is well known as a metal that can catalyze $2e^-$ ORR, either as part of a heterogeous catalysis, homogeous catalysis or an anchored single atom.[188,51,193,196,145,74,143,148,94,165,75,202] Sulfur and Selenium offer a cheap, earth abundant element that each pair with cobalt to form simple, easily synthesizable and phase pure compounds. $CoSe_2$ can exist in two structural polymorphs with different crystal structures, the cubic pyritetype (c-$CoSe_2$) and the orthorhombic marcasite-type (o-$CoSe_2$), whereas CoS_2 always exists as the cubic pyrite-type (c-CoS_2). These distinct structures of $CoSe_2$ polymorphs vs. CoS_2 can influence not only the catalyst activity and selectivity but also the catalyst stability under acidic electrochemical operations, which is critical from a practical perspective.

In this chapter, we use density functional theory (DFT) to explore three key metrics of catalyst performance: stability, activity, and selectivity. Creating surface Pourbaix diagrams, we interrogate the stability of the catalyst at reaction conditions. Utilizing the computational hydrogen electrode, we calculate the theoretical overpotential, which is directly related to catalyst activity. Finally, with transition state theory, we calculate the reaction barrier that determines if the reaction proceeds to the undesired thermodynamic product, water or to the desired kinetic product, H_2O_2. Finally, through these three performance metrics, we predict that o-$CoSe_2$ is the superior $2e^-$ catalyst and after confirmation with our experimental colleagues, conclude that o-$CoSe_2$ is the best performing $2e^-$ ORR investigated in acidic medium to date.

3.2 Methods

Spin polarized electronic structure calculations were performed using the Vienna Ab initio Simulation package (VASP)[85,86,83,84] interfaced with the Atomic Simulation Environment (ASE).[6] Projector augmented wave (PAW) pseudopotentials[10,87] with a cutoff of 450 eV were used to treat core electrons, and the Perdew–Burke–Ernzerhof (PBE) functional[135,136] was used to treat exchange and correlation. Dispersion was treated using Grimme's D3(ABC) method.[49] To better describe the Co 3d electrons in *c*-$CoSe_2$, a Hubbard U parameter,[4] U_{eff} = 2.0 eV, was taken from a previous report.[191] A variety of Hubbard U parameters were tested for *c*-CoS_2 and *o*-$CoSe_2$, and were found to have little to no effect on the geometries or energies; therefore, no Hubbard U parameter was used for these two catalysts. Solvation effects were treated using the continuum solvent method VASPsol.[107,106] The Brillouin zone was sampled using a (10, 10, 10) and (10, 10, 1) Γ-centered Monkhorst–Pack mesh[131] for bulk and surface calculations, respectively. Lattice constants were determined by fitting to an equation of state (EOS).[3]

The (100) surfaces of *c*-CoS_2 and *c*-$CoSe_2$ and the (101) surface of *o*-$CoSe_2$ were modelled as a 1 x 1 unit cell slab with two repeats in the z-direction, leading to a total of 8 Co atoms and 16 S/Se atoms and a vacuum gap of at least 15 Å. The top half of the slabs was allowed to relax while the bottom half was frozen to simulate the bulk. For each ionic configuration, the electronic energy was converged below 10^{-6} eV. Both the clean slab and adsorbates were allowed to relax until the forces were converged below 0.005 eV/Å^2. Transition states were located using the nudged elastic band (NEB) method[58,56] and were refined using the dimer method.[57,64,77] All transition states were confirmed saddle points with one imaginary frequency corresponding to bond breaking.

Binding energies were calculated with respect to $O_{2(g)}$ and $H^+_{(aq)}$ and e^-. The energy of

$H^+_{(aq)}$ and e^- was calculated using the computational hydrogen electrode (CHE) method,[126] where $H^+_{(aq)}$ is assumed to be in thermodynamic equilibrium with $H_{2(g)}$. In order to avoid well-known errors in the DFT treatment of $O_{2(g)}$, the free energy of $H_{2(g)}$ was determined by matching the experimental standard equilibrium potential (1.229 V) of the reaction $\frac{1}{2}O_{2(g)}$ + $2H^+_{(aq)}$ + $2e^- \rightarrow H_2O_{(l)}$. The free energies of species were calculated using $G = H - TS$, where H is the enthalpy including zero-point energy (ZPE) and thermal corrections, and S is either the total experimental entropy at 298 K and 1 bar (for gas phase species) or calculated under the harmonic approximation (for surface bound species). The free energy of $H_2O_{(l)}$ was calculated using the experimental free energy of formation for $H_2O_{(l)}$ and $H_2O_{(g)}$.The solvation free energy of $H_2O_{2(aq)}$ was calculated using the experimental Henry's law constant.[122] The calculated standard equilibrium potential of the $2e^-$ ORR reaction $O_{2(g)}$ + $2\,H^+_{(aq)}$ + $2e^-$ $\rightarrow H_2O_{2(aq)}$ is 0.81 V, while the experimental standard equilibrium potential is 0.69 V.

3.3 Results and Discussion

3.3.1 Bulk Pourbaix diagrams and electrochemical stability of $CoSe_2$ polymorphs

Practical electrochemical H_2O_2 production necessitates stable electrocatalysts for the selective $2e^-$ ORR. The crystal structures of both $CoSe_2$ polymorphs in comparison with *c*-CoS_2 are shown in Figure 3.2a–c. According to the calculated bulk Pourbaix diagrams available from the Materials Project,[69,163] the electrochemical stability window of *c*-CoS_2 is limited (Figure 3.1a), in agreement with a recent report.[200] In contrast, both $CoSe_2$ polymorphs exhibit much wider electrochemical stability windows that cover the entire potential range of interest for the acidic $2e^-$ ORR (Figure 3.1b and c). As such, $CoSe_2$ polymorphs are anticipated to better retain their structural integrity under acidic electrochemical operations, whereas *c*-CoS_2 is more prone to catalyst degradation due to surface oxidation and Co^{2+} dissolution. Therefore,

the enhanced electrochemical stability of $CoSe_2$ polymorphs could make them more practical $2e^-$ ORR catalysts in acidic solution for on-site water treatment applications, *inter alia*.

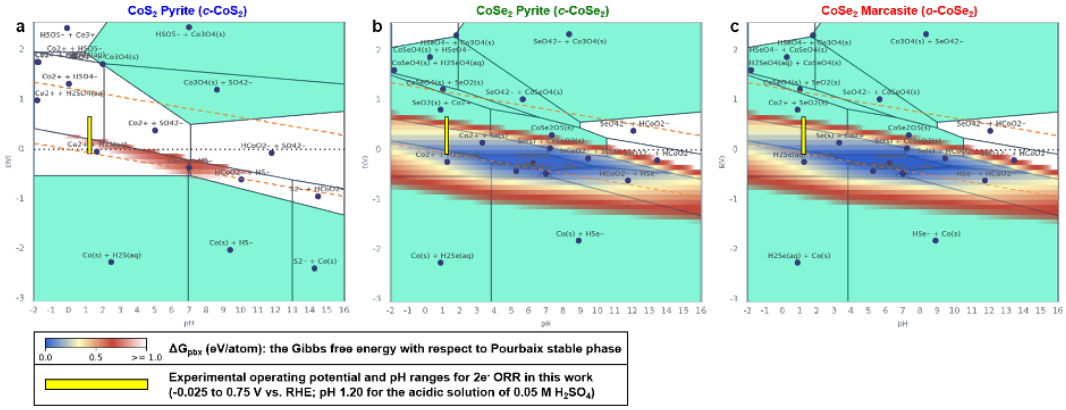

Figure 3.1: Calculated bulk Pourbaix diagrams of (a) *c*-CoS_2, (b) *c*-$CoSe_2$, and (c) *o*-$CoSe_2$ assuming an ionic concentration of 10^{-6} mol/kg for each element of interest (59 ppb Co, 32 ppb S, and 79 ppb Se, which are reasonably low concentrations that can fairly reflect the acidic electrolyte solution of 0.05 M H_2SO_4 used in our experiments). These diagrams are adapted from the Materials Project.[69] The multicolor gradient indicates the Gibbs free energy of the compound at a given set of potential and pH conditions with respect to its Pourbaix stable phase (ΔG_{pbx}), reflecting the electrochemical stability window of the compound. It was surmised in a previous report that materials with ΔG_{pbx} up to high values as much as 0.5 eV/atom can persist in electrochemical environments because of the energy barriers for the dissociation reactions.[163] The electrochemical stability windows of both *c*-$CoSe_2$ (b) and *o*-$CoSe_2$ (c) are clearly much wider than that of *c*-CoS_2 (a) and, more importantly, cover the entire potential range of interest for $2e^-$ ORR in acidic solution (indicated by the yellow color bars).

3.3.2 Mechanistic insights from surface Pourbaix diagrams of $CoSe_2$ polymorphs

To understand these differences in the electrochemical stability of $CoSe_2$ polymorphs vs. *c*-CoS_2 and to gain general mechanistic insights, we constructed calculated surface Pourbaix diagrams to predict the most thermodynamically stable surface termination of each catalyst for a given set of potential and pH conditions under the assumption that the surfaces can be approximated in equilibrium with $H_2O_{(l)}$.[183,52] The equilibrated proton-coupled electron transfer

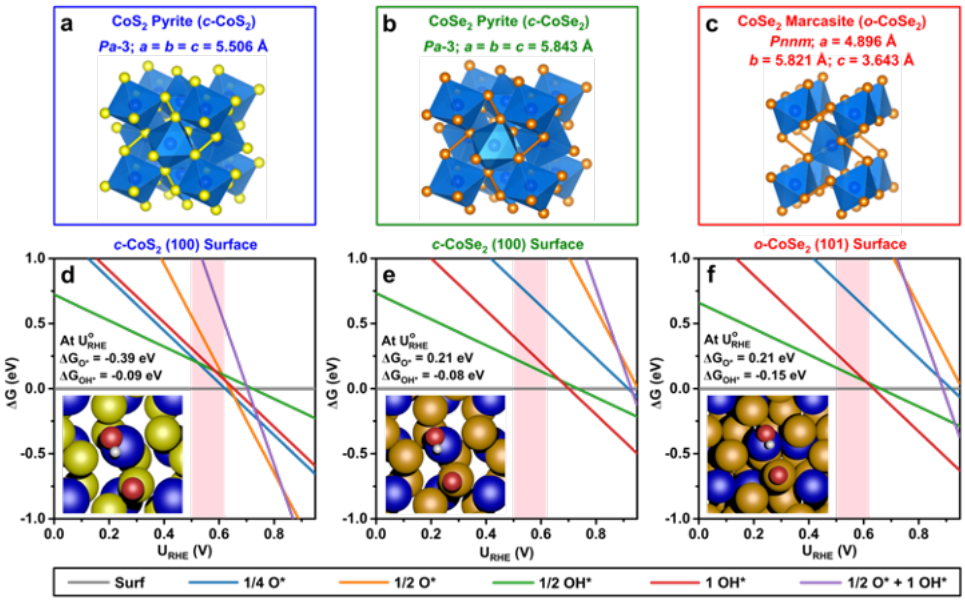

Figure 3.2: Crystal structures and surface Pourbaix diagrams. (a–c) Crystal structures, space groups, and lattice constants of (a) *c*-CoS_2, (b) *c*-$CoSe_2$, and (c) *o*-$CoSe_2$. The Co, S, and Se atoms are displayed in blue, yellow, and orange, respectively. (d–f) Calculated surface Pourbaix diagrams (ΔG vs. U_{RHE}) of (d) *c*-CoS_2 (100), (e) *c*-$CoSe_2$ (100), and (f) *o*-$CoSe_2$ (101) surfaces. Co and S/Se sites are the preferential binding sites for OH* and O*, respectively. A wide variety of surface coverages (from clean surface to $\frac{3}{4}$ ML O* + 1 ML OH*) are examined. For the sake of clarity, only the most stable surface coverages in the potential range of 0 to 1 V are shown here, and all the modelled surface coverages are shown in Figure 3.3). Surface free energies are assumed to be in equilibrium with $H_2O_{(l)}$. The unit cell has two Co binding sites and four S/Se binding sites. Binding energies of O* and OH* (ΔG_{O^*} and ΔG_{OH^*}) at the calculated standard equilibrium potential of $2e^-$ ORR (U^o_{RHE}) and top views of the catalyst surfaces with O* and OH* bound to their preferential binding sites are shown as insets. The Co, S, Se, O, and H atoms are displayed in blue, yellow, orange, red, and white, respectively. The highlighted regions in light red represent the experimentally relevant potential range where the optimal H_2O_2 production performances are achieved.

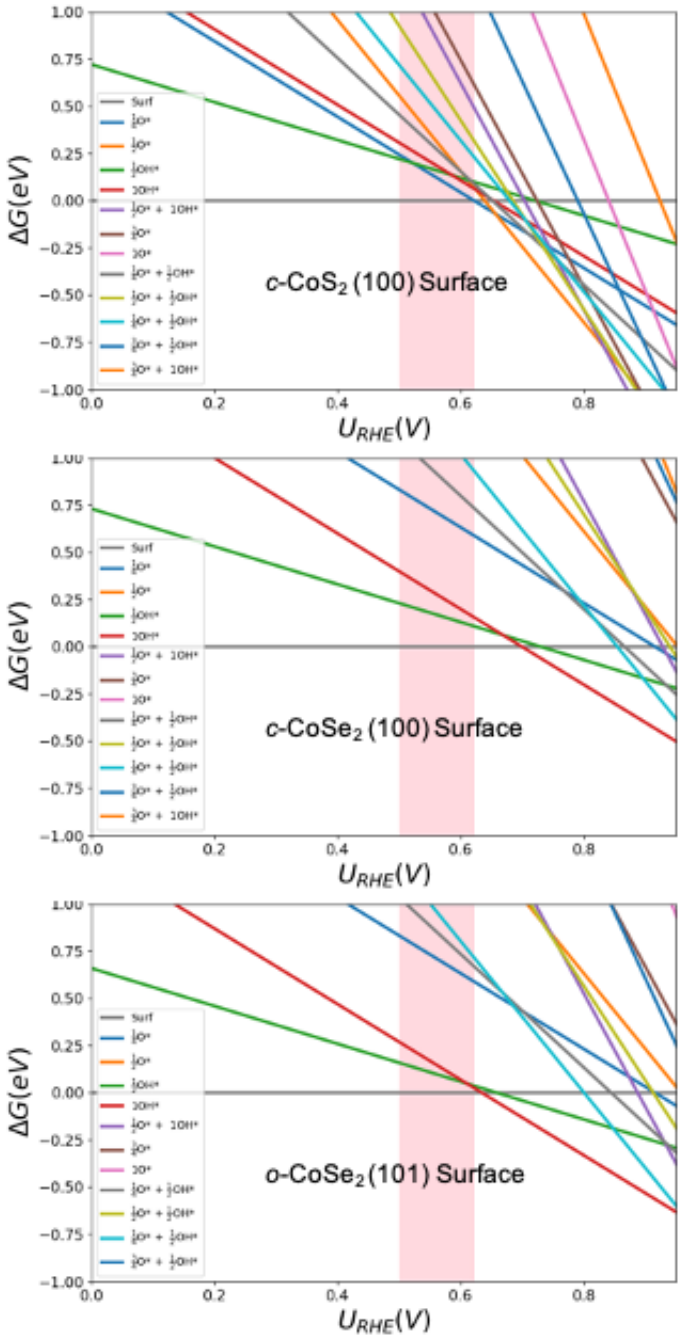

Figure 3.3: Surface Pourbaix diagrams (ΔG vs. U_{RHE}) of (a) *c*-CoS_2 (100), (b) *c*-$CoSe_2$ (100), and (c) *o*-$CoSe_2$ (101) surfaces showing all the modeled surface coverages (from clean surface to $\frac{3}{4}$ ML O* + 1 ML OH*). The highlight regions in light red represent the experimental relevant potential range where the optimal H_2O_2 production performances are achieved. In comparison, Figure 3.2 shows only the most stable surface coverages in the potential range of 0 to 1 V.

(PCET) reaction for a general surface intermediate can then be written as:

$$\text{X-O}_m\text{H}_n^* + (2m-n)(\text{H}^+ + \text{e}^-) \rightleftharpoons \text{X}^* + m\text{H}_2\text{O} \tag{3.1}$$

where X is the surface binding site, m is the number of oxygen atoms, and n is the number of hydrogen atoms. The free energy of this reaction can be written as:

$$\Delta G(U, pH) = G_{\text{S}*} + mG_{\text{H}_2\text{O}} - G_{\text{X-O}_m\text{H}_n^*} - (2m-n)(G_{e^-} + G_{H^+}) \tag{3.2}$$

Using the computational hydrogen electrode (CHE) method[126,184,88,34] ($G_{e^-} + G_{H^+} = \frac{1}{2}G_{\text{H}_2} - U_{SHE} - 2.303k_bT\text{pH}$) and converting the standard hydrogen electrode to the reversible hydrogen electrode ($U_{RHE} = U_{SHE} + 2.303k_BT\text{pH}$), the free energy can be rewritten as a function of U_{RHE}:

$$\Delta G(U_{RHE}) = G_{S*} + mG_{\text{H}_2\text{O}} - G_{\text{X-O}_m\text{H}_n^*} - (2m-n)(\frac{1}{2}G_{\text{H}_2} - U_{RHE}) \tag{3.3}$$

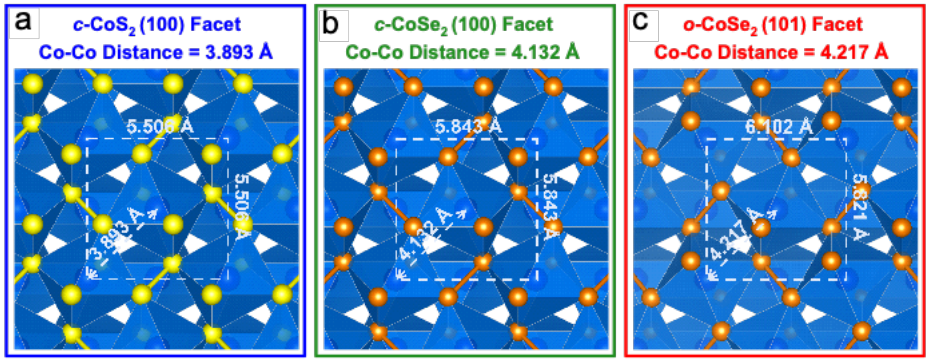

Figure 3.4: Top views and Co-Co interatomic distances of (a) *c*-CoS_2 (100), (b) *c*-$CoSe_2$ (100), and (c) *o*-$CoSe_2$ (101) surfaces. The *o*-$CoSe_2$ (101) surface mostly resembles the (100) surface of *c*-$CoSe_2$.

We used density functional theory (DFT) and the CHE method[126,184,88,34] to construct calculated surface Pourbaix diagrams of all three catalysts on their most thermodynamically sta-

ble facets. We found that the (100) facet of cubic c-$CoSe_2$ has the lowest surface energy, in agreement with cubic c-CoS_2 (see Table 3.1). For orthorhombic o-$CoSe_2$, we investigate the (101) facet because it is not only the facet with the lowest surface energy, (see Table 3.2) but it also keeps the Se_2^{2-} dumbbells intact and it is structurally similar to the (100) facets of cubic c-CoS_2 and c-$CoSe_2$ (see Figure 3.4a-c). We utilized a 1 x 1 unit cell slab of the catalyst surface that has two Co binding sites and four S/Se binding sites to model intermediate surface coverages as a function of potential (Figure 3.2d-f). The preferential binding sites for OH* and O* are Co and S/Se sites, respectively (see the insets of Figure 3.2d–f). Therefore, we investigated $\frac{1}{4}$, $\frac{1}{2}$, $\frac{3}{4}$ and 1 monolayer (ML) O* coverages, $\frac{1}{2}$ and 1 ML OH* coverages, and any combinations thereof. For example, the co-adsorption of $\frac{1}{4}$ ML O* and $\frac{1}{2}$ ML OH* on $CoSe_2$ polymorphs and c-CoS_2 in equilibrium with their clean surfaces can be written respectively as:

$$\text{Co-OH}^* + \text{Se-O}^* + 3(\text{H}^+ + \text{e}^-) \rightleftharpoons \text{Co}^* + \text{Se}^* + 2\text{H}_2\text{O} \tag{3.4}$$

$$\text{Co-OH}^* + \text{S-O}^* + 3(\text{H}^+ + \text{e}^-) \rightleftharpoons \text{Co}^* + \text{S}^* + 2\text{H}_2\text{O} \tag{3.5}$$

Table 3.1: Surface energies of the most thermodynamically stable facets of cubic c-CoS_2 and c-$CoSe_2$. Data on c-CoS_2 are calculated without a dispersion correction and data c-$CoSe_2$ are calculated with Grimme's D3(ABC) dispersion correction as detailed in the methods section.

Facet	Surface Energy (ev/Å^2)	
	c-CoS_2	c-$CoSe_2$
(100)	0.032	0.044
(110)	0.060	0.064
(111)	0.057	0.069

where OH* and O* are bound to their preferential binding site of Co and S/Se, respectively (see Equation 3.1 for the general form of these equations). For the sake of clarity, Figure 3.2d–f only show the most thermodynamically stable surface coverages in the potential (U_{RHE})

Table 3.2: Surface energies of the most thermodynamically stable facets of orthorhombic *o*-$CoSe_2$

Facet	Surface Energy (ev/Å^2)
	o-$CoSe_2$
(001)	0.060
(010)	0.044
(100)	0.070
(110)	0.041
(111)	0.060

range of 0 to 1 V, while all the modelled surface coverages are shown in Figure 3.3. We note that the calculated standard equilibrium potential of the 2e$^-$ ORR (U^o_{RHE}) is 0.81 V, slightly higher than the experimental value (E^o) of 0.69 V. Since our experimental results show that the optimal H_2O_2 production performances are achieved at 0.5 V vs. RHE (vide infra), the experimentally relevant potential range between 0.5 and 0.62 V is highlighted in Figure 3.2. At 0.5 V, all surfaces are predicted to be mostly free of adsorbates. However, at the most important 0.62 V, we predict $\frac{1}{4}$ ML O* coverage on *c*-CoS_2 (Figure 3.2d), a clean *c*-$CoSe_2$ surface (Figure 3.2e), and 1 ML OH* coverage on *o*-$CoSe_2$ (Figure 3.2f). The differences in the surface terminations of all three catalysts under equilibrium conditions with $H_2O_{(l)}$ can be explained by the relative differences in the O* and OH* binding strengths. O* binds 0.59 eV more strongly to S sites of *c*-CoS_2 than to Se sites of $CoSe_2$ polymorphs (see the ΔG^{O^*} values in Figure 3.2d-f). Therefore, we predict a moderate O* coverage on *c*-CoS_2 at low overpotentials (Figure 3.2d), which will likely lead to surface oxidation, the formation of $SO_4{}^{2-}$, and the subsequent leaching of Co^{2+}. In contrast, O* coverage is not the most stable surface termination on $CoSe_2$ polymorphs at low overpotentials (Figure 3.2e and f) because of the weak O* binding to Se sites, suggesting that $CoSe_2$ polymorphs should be more resistant to surface oxidation and catalyst degradation, consistent with their wide electrochemical stability windows in the bulk Pourbaix diagrams (Figure 3.1b and c).

While changing the nature of the anion in the catalyst modifies the binding strength of O* and leads to increased stability of $CoSe_2$ polymorphs, switching from the cubic to the orthorhombic crystal structure affects the binding strength of OH* to the preferential Co binding sites. The (101) surface of orthorhombic *o*-$CoSe_2$, which has a longer Co-Co interatomic distance than the (100) surfaces of both cubic structures (Figure 3.4), exhibits a slight increase in the OH* binding strength by 0.06 and 0.07 eV compared to the (100) surfaces of cubic *c*-CoS_2 and *c*-$CoSe_2$, respectively (see the ΔG_{OH^*} values in Figure 3.2d–f). At low overpotentials, we predict a moderate to high OH* coverage on both $CoSe_2$ polymorphs, which will slowly decrease as the overpotential increases. As OH* binds to Co sites, a higher OH* coverage decreases the number of Co site ensembles available to break the O–O bond in OOH*. Thus, OH* coverage on Co sites may increase the $2e^-$ ORR selectivity, suggesting that orthorhombic *o*-$CoSe_2$ could be more selective than cubic *c*-$CoSe_2$ and *c*-CoS_2. Overall, the surface and bulk Pourbaix diagrams predict that both $CoSe_2$ polymorphs are more electrochemically stable than *c*-CoS_2, while *o*-$CoSe_2$ could be the most intrinsically selective toward the $2e^-$ ORR among all three catalysts.

3.3.3 Computational prediction of the selective $2e^-$ ORR energetics on $CoSe_2$ polymorphs

We further calculated free energy diagrams of the $2e^-$ ORR vs. the competing $4e^-$ ORR pathway to elucidate the catalytic activity and selectivity of $CoSe_2$ polymorphs. The catalytic activity toward the $2e^-$ ORR is governed by the following PCET reactions:

$$O_{2(g)} + * + (H^+ + e^-) \rightarrow OOH^* \tag{3.6}$$

$$OOH^* + (H^+ + e^-) \rightarrow H_2O_{2(aq)} \tag{3.7}$$

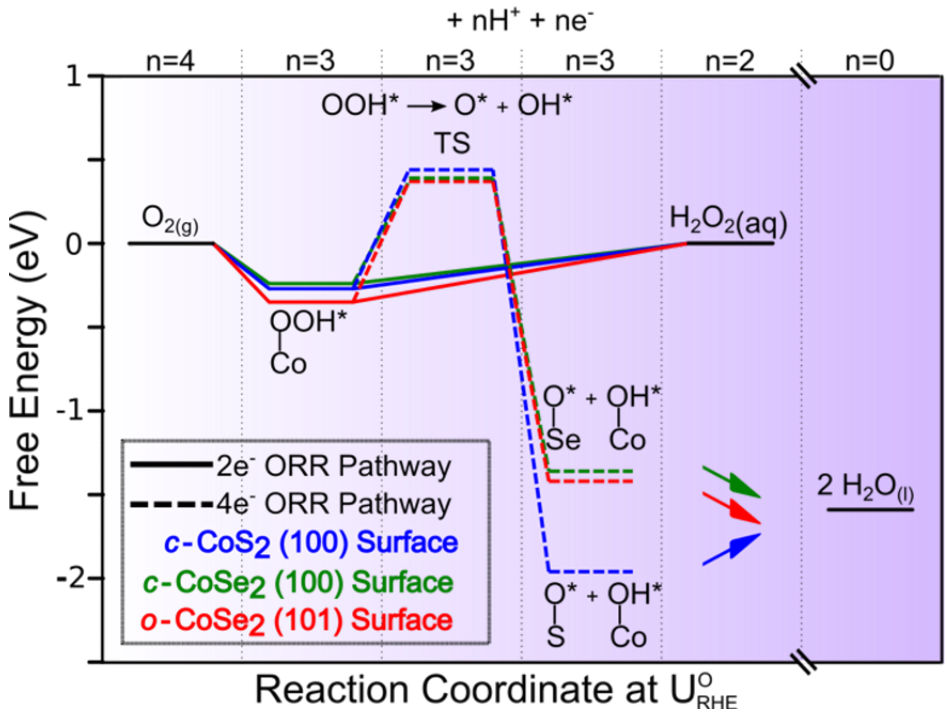

Figure 3.5: Calculated free energy diagrams of $2e^-$ and $4e^-$ ORR pathways. Calculated free energy diagrams were performed on *c*-CoS_2 (100), *c*-$CoSe_2$ (100), and *o*-$CoSe_2$ (101) surfaces at the calculated standard equilibrium potential of $2e^-$ ORR (U^o_{RHE}). Possible $2e^-$ and $4e^-$ ORR pathways are depicted in solid and dashed lines, respectively. The traces for *c*-CoS_2 (100), *c*-$CoSe_2$ (100), and *o*-$CoSe_2$ (101) surfaces are displayed in blue, green, and red, respectively. These calculations are performed on clean surfaces as the binding energies of OOH* are insensitive to other surface adsorbates present on *c*-CoS_2 and both $CoSe_2$ polymorphs at low overpotentials (see surface Pourbaix diagrams in Figure 3.2).

where the preferential binding sites for OOH* are Co sites on all three catalysts. At the calculated standard equilibrium potential of the 2e$^-$ ORR U_{RHE}, the first PCET step (Equation 3.6) is moderately downhill by 0.27, 0.24, and 0.35 eV on the *c*-CoS_2 (100), *c*-$CoSe_2$ (100), and *o*-$CoSe_2$ (101) surfaces, respectively (Figure 3.5), indicating that all three catalysts should be active toward the 2e$^-$ ORR, and *c*-$CoSe_2$ could be the most intrinsically active among all three catalysts. While the catalytic activity of the 2e$^-$ ORR is determined by Equations 3.6 and 3.7, the catalytic selectivity of the 2e$^-$ vs. 4e$^-$ ORR is set by the resistance to O–O bond scission in the OOH* adsorbate:

$$\mathrm{OOH}^* \rightarrow \mathrm{O}^* + \mathrm{OH}* \tag{3.8}$$

$$\mathrm{OOH}^* + * + (\mathrm{H}^+ + \mathrm{e}^-) \rightarrow \mathrm{O}^* + \mathrm{H_2O}_{(l)} \tag{3.9}$$

The cleavage of the O–O bond in OOH* will result in a buildup of O* and OH* on the catalyst surface (Equation 3.8). These species can either lead to oxidation/dissolution of the catalyst or be further reduced to $H_2O_{(l)}$. Breaking the O–O bond in OOH* requires an ensemble of neighboring Co sites to move toward each other, after which OOH* will dissociate into O* and OH* that are initially bound to Co sites.[157] O* can then easily migrate to S/Se sites, which are the preferential binding sites for O* on all three catalysts. Alternatively, the O–O bond in OOH* could be cleaved through reductive elimination (Equation 3.9) to form O* and $H_2O_{(l)}$. However, this is unlikely as only the proximal oxygen in OOH* interacts strongly with the catalyst surface. Therefore, PCET to the surface-bound oxygen to form H_2O_2 (Equation 3.7) will likely dominate over PCET to the distant oxygen to form $H_2O_{(l)}$ and O* (Equation 3.9).[157] The OOH* dissociation barriers on all three catalysts are fairly similar (Figure 3.5), in agreement with the similarity of their OOH* binding energies and surface structures. The (101) surface of *o*-$CoSe_2$ exhibits a slightly higher OOH* dissociation barrier of 0.72 eV than

the (100) surfaces of *c*-CoS_2 and *c*-$CoSe_2$, where the barrier is 0.71 and 0.63 eV, respectively (Figure 3.5. These barriers to O–O bond scission on $CoSe_2$ polymorphs and CoS_2 are significantly higher than those on close-packed metals such as Pd (0.06 eV), Pt (0.16 eV), and Cu (0.06 eV),[34] indicating that spatial separation of neighboring Co sites by S/Se anions (Figure 3.4) is critical to the selective $2e^-$ ORR pathway. Overall, the calculated free energy diagrams suggest that both $CoSe_2$ polymorphs are active and selective $2e^-$ ORR catalysts and that *c*-$CoSe_2$ could be more intrinsically active while *o*-$CoSe_2$ could be more intrinsically selective.

3.4 Experimental Validation and Interpretation

Experiments were done by Professor Song Jin's lab. Methods and further experimental details can be found in our recent publications, Reference 157 and Reference 158.

We systematically investigated the $2e^-$ ORR activity and selectivity of *c*-CoS_2, *c*-$CoSe_2$ and o-$CoSe_2$ catalysts to experimentally validate and further elaborate the mechanistic insights predicted by our calculated free energy diagrams and surface Pourbaix diagrams. As these catalyst samples may exhibit different specific surface areas, we performed RRDE measurements of each catalyst with various catalyst loadings for fair comparisons. In 0.05 M H2SO4 solution (pH 1.20), both $CoSe_2$ polymorph catalysts showed efficient and selective H_2O_2 production at low overpotentials (Figure 3.6a), consistent with the calculated free energy diagrams (Figure 3.5). The ORR catalytic onset on both $CoSe_2$ polymorphs took place at potentials slightly more positive than the standard equilibrium potential of $2e^-$ ORR (E^o = 0.69 V vs. RHE), which is due to the Nernstian shift in the $2e^-$ ORR equilibrium potential when the bulk concentration of H_2O_2 is very low.[74] We investigated the H_2O_2 selectivity of both $CoSe_2$ polymorphs as a function of overpotential and catalyst loading (Figure 3.5). In the low overpoten-

tial region, the overall ORR current density (delivered on the disk electrode) and the partial current density for H_2O_2 production ($j_{peroxide}$, detected on the ring electrode and further adjusted by the collection efficiency) steadily increased with higher catalyst loadings, while the H_2O_2 selectivity appeared to be very high (>80%) and fairly insensitive to the catalyst loading. In the high overpotential region, however, the H_2O_2 production was less selective as the catalyst loading increased. These observations can be rationalized by our calculated surface Pourbaix diagrams (Figure 3.2e,f). At low overpotentials, both $CoSe_2$ polymorphs feature high OH* coverages on surface Co sites and fewer unsaturated Co active sites for the undesired OOH* scission, explaining their intrinsic high selectivity toward $2e^-$ ORR across various catalyst loadings. As the overpotential increases, both $CoSe_2$ polymorphs form clean surfaces with many unsaturated Co sites, which may allow for the competing $4e^-$ ORR pathway via OOH* scission. As the catalyst loading increases, the total amount of unsaturated Co sites and the catalyst film thickness also increase, which may trigger more side reactions of H_2O_2 reduction and/or decomposition, and lower the H_2O_2 selectivity.[173] These RRDE results suggest that $CoSe_2$ polymorphs should operate at low overpotentials, where they are intrinsically selective toward $2e^-$ ORR, and with high catalyst loadings to achieve the optimal overall electrode performances for H_2O_2 production in acidic solution.

The catalytic properties of *c*-CoS_2 and *c*-$CoSe_2$ were directly compared at the same catalyst loading (76, 152, 229, or 305 $\mu g_{Co}/cm^2_{disk}$) because they delivered similar overall current densities (Figure 3.6a$_1$). *c*-$CoSe_2$ was clearly more selective toward $2e^-$ ORR than *c*-CoS_2 in the low overpotential region (Figure 3.6a), consistent with the calculated surface Pourbaix diagrams which predict that the undesired OOH* scission can be effectively suppressed on $CoSe_2$ due to high OH* coverages on surface Co sites. On the other hand, it was not straightforward to directly compare the catalytic properties of *c*-CoS_2 and *o*-$CoSe_2$ at the same catalyst loading because *o*-$CoSe_2$ delivered a much higher overall ORR current density than *c*-CoS_2;

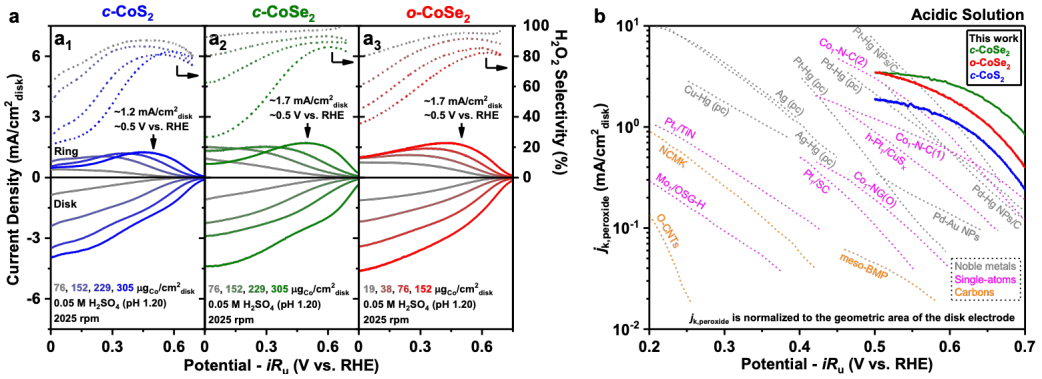

Figure 3.6: Electrochemical characterization of selective 2e$^-$ ORR on *c*-CoS_2, *c*-$CoSe_2$ and *o*-$CoSe_2$ catalysts. (a) RRDE voltammograms recorded at 2025 rpm and the corresponding H_2O_2 selectivity of (a_1) *c*-CoS_2, (a_2) *c*-$CoSe_2$ and (a_3) *o*-$CoSe_2$ catalyst with various catalyst loadings in O_2-saturated 0.05 M H_2SO_4 solution (pH 1.20). (b) Kinetic current densities for H_2O_2 production normalized to the geometric area of the disk electrode ($j_{k,peroxide}$) on *c*-CoS_2 (305 $\mu g_{Co}/cm^2_{disk}$), *c*-$CoSe_2$ (305 $\mu g_{Co}/cm^2_{disk}$) and *o*-$CoSe_2$ (152 $\mu g_{Co}/cm^2_{disk}$) catalysts, in comparison with previously reported 2e$^-$ ORR catalysts (noble metals, single-atom catalysts, and carbon materials) based on RRDE measurements in acidic solution. The traces for *c*-$CoSe_2$, *o*-$CoSe_2$, and *c*-CoS_2 catalysts are from this work, which are recorded at 1600 rpm and cut off at 0.5 V vs. RHE where $j_{peroxide}$ reaches its approximate maximum. Other traces are from previous reports: ref. 161 for Pt-Hg NPs/C and Pt-Hg (pc); ref. 181 for Pd-Hg NPs/C, Pd-Hg (pc), Ag (pc), Ag-Hg (pc), Cu-Hg (pc); ref. 138 for Pd-Au NPs; ref. 21 for Pt1/SC; ref. 195 for Pt1/TiN; ref. 156 for h-Pt1/CuSx; ref. 173 for Co1-N-C(1); ref. 74 for Co1-NG(O); ref. 41 for Co1-N-C(2); ref. 176 for Mo1-OSG-H; ref. 96 for O-CNTs; ref. 54 for meso-BMP; ref. 174 for NCMK.

this is perhaps not surprising given their very different nanoscale morphologies. Therefore, we performed fair comparisons between *c*-CoS_2 (76, 152, 229, or 305 $\mu g_{Co}/cm^2_{disk}$) and *o*-$CoSe_2$ (19, 38, 76, or 152 $\mu g_{Co}/cm^2_{disk}$) when they delivered similar overall ORR current densities at different catalyst loadings. Similar to the *c*-$CoSe_2$ polymorph and as expected from surface Pourbaix diagrams, *o*-$CoSe_2$ was also more selective toward $2e^-$ ORR than *c*-CoS_2 at low overpotentials. Moreover, compared to *c*-CoS_2 and *c*-$CoSe_2$, the H_2O_2 selectivity of *o*-$CoSe_2$ in the high overpotential region was slightly better retained as the catalyst loading increased. Since the binding strength of OH* to *o*-$CoSe_2$ is greater than that to *c*-CoS_2 and *c*-$CoSe_2$, it is less favorable to completely reduce OH* via PCET and form a clean surface of *o*-$CoSe_2$ at high overpotentials, which may result in its enhanced H_2O_2 selectivity in the high overpotential region.

These RRDE experiments confirm that two $CoSe_2$ polymorphs are highly active and selective $2e^-$ ORR electrocatalysts in acidic solution and outperform the CoS_2 catalyst. The optimal overall electrode performances for H_2O_2 production can be achieved at the highest catalyst loadings when $j_{peroxide}$ reached the maximum of 1.7 mA/cm^2_{disk} at 0.5 V vs. RHE on both catalysts (Figure 3.6), but *o*-$CoSe_2$ required a much lower catalyst loading (152 $\mu g_{Co}/cm^2_{disk}$) than *c*-$CoSe_2$ (305 $\mu g_{Co}/cm^2_{disk}$) to achieve a similar overall electrode performance, because the *o*-$CoSe_2$ sample exhibited a much higher double layer capacitance (Cdl) value and thus a larger electrochemically active surface area (ECSA) than the c-$CoSe_2$ sample. Therefore, the high-surface-area *o*-$CoSe_2$ catalyst is more advantageous for practical electrochemical H_2O_2 production because of the lower catalyst loadings and reduced catalyst cost.

To quantitatively compare the H_2O_2 production performances of all three catalysts with previously reported $2e^-$ ORR catalysts in acidic solution, we extracted kinetic current density for H_2O_2 production ($j_{k,peroxide}$) by correcting as-measured $j_{peroxide}$ for mass-transport loss using Koutecky-Levich (K-L) analysis based on RRDE voltammograms recorded at various

rotation rates. $j_{k,peroxide}$ is normalized by the geometric area of the disk electrode to reflect the overall yield of H_2O_2 product without mass-transport limitation, which clearly increased with higher catalyst loadings. Although this $j_{k,peroxide}$ normalized to the disk area can be affected by the catalyst loading and the catalyst surface area and thus does not reflect the intrinsic catalyst property, it is important for practical applications. Therefore, we chose the highest catalyst loadings of *c*-$CoSe_2$ (305 $\mu g_{Co}/cm^2_{disk}$) and *o*-$CoSe_2$ (152 $\mu g_{Co}/cm^2_{disk}$) for comparisons with previously reported $2e^-$ ORR catalysts in acidic solution (Figure 3.6b). Both *c*-$CoSe_2$ and *o*-$CoSe_2$ catalysts show clearly more efficient H_2O_2 production than *c*-CoS_2 and other reported single-atom[41] or carbon[174] catalysts, and display even better overall electrode performances than the state-of-the-art noble metal catalysts[161,181] in the more important low overpotential region. This comparison of $j_{k,peroxide}$ reveals that $CoSe_2$ polymorph catalysts are the best-performing $2e^-$ ORR electrocatalysts reported so far in acidic solution.

We examined the catalyst stability of both $CoSe_2$ polymorphs for electrochemical H_2O_2 production in 0.05 M H_2SO_4 solution by continuously applying RRDE scans while sequentially changing the rotation rate, analogous to the accelerated degradation tests typically applied to conventional $4e^-$ ORR catalysts.[198,79] These RRDE scans recorded at the highest rotation rate of 2025 rpm clearly revealed the enhanced catalyst stability of *c*-CoS_2 (305 $\mu g_{Co}/cm^2_{disk}$), *c*-$CoSe_2$ (305 $\mu g_{Co}/cm^2_{disk}$) and *o*-$CoSe_2$ (152 $\mu g_{Co}/cm^2_{disk}$) (Figure 3.7a). The disk currents and the ring currents of both $CoSe_2$ polymorphs were relatively stable during catalyst stability tests (Figure $3.7a_2$,a_3), whereas those of *c*-CoS_2 (305 $\mu g_{Co}/cm^2_{disk}$) evidently decreased over time (Figure $3.7a_1$). We further quantitatively compared the disk current and ring current retentions of all three catalysts at 0.5 V vs. RHE where $j_{peroxide}$ reached its approximate maximum (Figure 3.7b). Over the same time period of 2.5 h, the disk current of *c*-$CoSe_2$ was almost completely retained (100%), whereas *c*-CoS_2 only retained 62% of its initial disk current (Figure $3.7b_1$). Notably, the high-surface-area *o*-$CoSe_2$ displayed a near-unity disk current

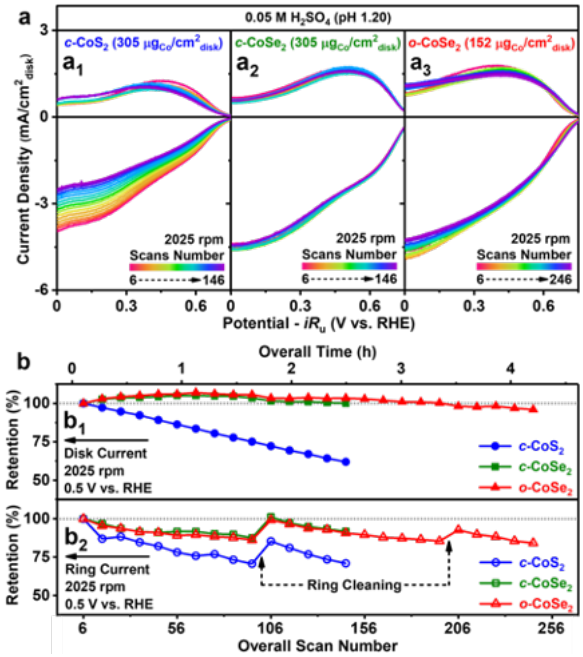

Figure 3.7: Enhanced stability of *c*-$CoSe_2$ and *o*-$CoSe_2$ catalysts from RRDE measurements. (a) RRDE voltammograms of (a_1) *c*-CoS_2 (305 $\mu g_{Co}/cm^2_{disk}$), (a_2) *c*-$CoSe_2$ (305 $\mu g_{Co}/cm^2_{disk}$), and (a_3) *o*-$CoSe_2$ (152 $\mu g_{Co}/cm^2_{disk}$) recorded at 2025 rpm during catalyst stability tests in O_2-saturated 0.05 M H2SO4 solution (pH 1.20). (b) Retention rates of (b1) disk current and (b2) ring current at 2025 rpm and 0.5 V vs. RHE (where $j_{peroxide}$ reaches its approximate maximum) during catalyst stability tests.

retention over a longer time period of 4.2 h (Figure 3.7b$_1$). Note that the slight decrease in the ring currents of both $CoSe_2$ polymorphs (Figure 3.7b$_2$) was mainly due to the formation of surface PtO_x on the ring electrode after its continuous operation at the high potential of 1.3 V vs. RHE.[96,72] After periodic electrochemical cleaning of the ring electrode, the ring currents of both $CoSe_2$ polymorphs were immediately recovered (Figure 3.7b$_2$), indicating that the electrochemical H_2O_2 production was stable on both $CoSe_2$ polymorphs.

Table 3.3: Average cobalt leaching rates of *c*-CoS_2, *c*-$CoSe_2$ and *o*-$CoSe_2$ during catalyst stability tests in 0.05 M H_2SO_4 solution from RRDE measurements.

Catalyst	Catalyst Loading	Stability Test Duration	[Co] in Tested Electrolyte	Ave. Cobalt Leaching Rate
c-CoS_2	305 $\mu g_{Co}/cm^2_{disk}$	2.5 h (151 scans)	36.6 μg_{Co}/L	0.66 μg_{Co}/h
c-$CoSe_2$	305 $\mu g_{Co}/cm^2_{disk}$	2.5 h (151 scans)	21.8 μg_{Co}/L	0.39 μg_{Co}/h
o-$CoSe_2$	152 $\mu g_{Co}/cm^2_{disk}$	4.2 h (251 scans)	28.5 μg_{Co}/L	0.31 μg_{Co}/h

To better understand the origin of the enhanced catalyst stability of $CoSe_2$ compared to CoS_2, we recovered all of the tested catalysts to examine their surface composition and structural integrity using Raman spectroscopy and XPS. Raman spectra suggested the crystal structures of all tested catalysts, including the apparently least stable *c*-CoS_2 catalyst, were well retained without the formation of crystalline or amorphous impurities. XPS spectra suggested their surface chemical states remained the same as the pristine catalysts. This is understandable because the bulk Pourbaix diagram (Figure 3.1a) suggests the degradation of *c*-CoS_2 via surface oxidation yields soluble species of Co^{2+} and $SO_4{}^{2-}$ that can readily leach into electrolyte solutions without being detected by XPS. The leaching of *c*-CoS_2 was also implied by the slight change in its surface composition after the catalyst stability test, whereas both $CoSe_2$ polymorphs appeared to be more stable with minimal changes in their surface compositions. Therefore, it is essential to quantify the Co^{2+} leaching rate by using inductively coupled plasma mass spectrometry (ICP-MS) to analyze the tested electrolyte solutions, so that the stability of these three catalysts can be differentiated based on the total amount of

Co^{2+} leached per hour (μg_{Co}/h). As summarized in Table 3.3, the more stable *o*-$CoSe_2$ (152 $\mu g_{Co}/cm^2_{disk}$) and *c*-$CoSe_2$ (305 $\mu g_{Co}/cm^2_{disk}$) exhibited similar leaching rates of 0.31 and 0.39 μg_{Co}/h, respectively, whereas the least stable *c*-CoS_2 (305 $\mu g_{Co}/cm^2_{disk}$) leached almost twice as fast (0.66 μg_{Co}/h). In fact, this Co^{2+} leaching from $CoSe_2$ could potentially be transient and take place mostly at the initial stage of electrochemical operations. These leaching results are consistent with our theoretical prediction that both $CoSe_2$ polymorphs are more resistant to surface oxidation than *c*-CoS_2, because the binding strength of O* to Se sites is substantially weaker than that to S sites by 0.59 eV, and display significantly enhanced catalyst stability for the electrosynthesis of H_2O_2 in acidic solution.

3.5 Conclusion

In conclusion, this study demonstrates stable and selective electrosynthesis of H_2O_2 on $CoSe_2$ polymorph catalysts in acidic solution, establishing new understandings on catalyst stability for $2e^-$ ORR and significantly advancing the practical production and utilization of H_2O_2 in acidic solution. Calculated surface Pourbaix diagrams reveal the weak binding of O* to Se sites and predict enhanced electrochemical stability for $CoSe_2$ than CoS_2. Additionally, all three catalysts are computationally predicted to be active and selective 2e- ORR electrocatalysts based on the theoretical overpotential and strength of the O-O bond in OOH*. RRDE experiments in 0.05 M H_2SO_4 show that $CoSe_2$ polymorphs are the best-performing $2e^-$ ORR electrocatalysts reported so far in acidic solution, delivering higher kinetic current densities for H_2O_2 production at low overpotentials than reported state-of-the-art noble metal or single-atom catalysts. Detailed structural characterization and ICP-MS analysis of tested $CoSe_2$ catalysts and electrolyte solutions confirm their enhanced catalyst stability and resistance to catalyst leaching during prolonged electrochemical operations. This integrated study not only

establishes $CoSe_2$ polymorphs as the new benchmark $2e^-$ ORR electrocatalysts in acidic solution and demonstrates effective on-site electrosynthesis of H_2O_2, but also reveals new mechanistic insights and introduces new design rules for stable and efficient earth-abundant transition metal compound electrocatalysts for decentralized production and utilization of H_2O_2.

4

Hydrogen Peroxide Synthesis on $NiSe_2$ and $(Co,Ni)Se_2$: Investigating the Entire Sabatier Curve

4.1 Introduction

Our recent investigation of cobalt dichalcogenide $2e^-$ ORR catalysts (see Ref. 157, 158 and Chapter 3) established $CoSe_2$ polymorph catalysts as the new benchmark for performance of $2e^-$ ORR catalysts in acidic media. In these works, We also developed a theoretical framework to evaluate three important catalyst metrics: stability, activity and selectivity. Evidence of stable catalysts include a wide electrochemical stability window in a bulk Pourbaix diagram, a clean surface at experimentally relevant potentials as predicted by surface Pourbaix diagrams and finally, weak adsorbate binding, particularly to chalcogen sites. Activity is predicted by the binding strength of OOH*. The most active catalyst will have an OOH* binding energy of 0 eV, which indicates a theoretical overpotential of 0 V. Selectivity is controlled by the strength of the O-O bond in OOH*. The stronger the bond, the higher the activation barrier towards bond scission and therefore, the lower the flux through the $4e^-$ pathway.

In this work, we apply this theoretical framework to evaluate the catalytic performance of the earth abundant metal compounds nickel diselenide ($NiSe_2$) and the cobalt nickel diselenide alloy ($(Co,Ni),Se_2$) for $2e^-$ ORR. Our choice of Ni is motivated by the Sabatier principle, which states that there exists an optimal binding strength that will balance the activation of the reactant and the desorption of the product. For 2 e^- ORR, this corresponds to optimizing the binding strength of OOH*. The ideal binding strength of OOH*, as stated above, is 0 eV. All three Co catalysts investigated[157,158] had OOH* overbound, falling on the left side of the Sabatier curve (see Figure 4.1).

To improve the catalyst activity, we investigate a catalyst that we believe will bind OOH* more weakly while maintaining or improving selectivity and stability. Ni based catalysts are successful $2e^-$ ORR catalysts, whether as part of metal compounds[98,5,194,120] or anchored single-atom catalysts.[173,187,168,92] Previous results from our group[59] indicate that OOH* is

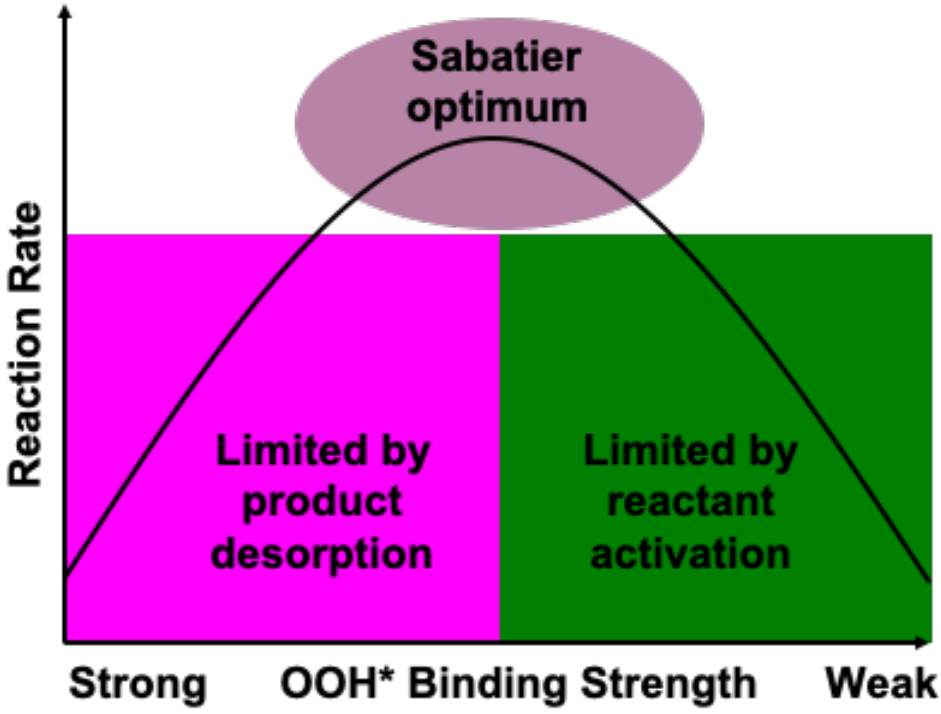

Figure 4.1: Graphical depiction of the Sabatier principle. On the left are catalysts that overbind OOH* (such as Co dichalcogenides) and on the right are catalysts that underbind OOH* (such as Ni dichalcogenides).

underbound on NiS_2. Our results from Chapter 3 indicate that diselenide pyrite catalysts are more stable than disulfide pyrite catalysts. Therefore, pyrite nickel diselenide (*c*-$NiSe_2$) is a candidate to explore the right side of the Sabatier $2e^-$ ORR curve. Once both sides of the Sabatier curve have been explored, one approach to reach the peak of the Sabatier curve (see Figure 4.1) is to tune the electronic properties of a material by alloying two materials on each side of the curve.

In this chapter, we apply the theoretical performance framework developed in chapter 3 to explore the stability, activity and selectivity of *c*-$NiSe_2$ and compare to *c*-$CoSe_2$. We find that *c*-$NiSe_2$ underbinds OOH* compared to Co dichalcogenides while maintaining the stability enhancement of pyrite diselenides over pyrite disulfides. All three metrics indicate that this catalyst is worth exploring synthetically. We then create an computational model of a *c*-(Co,Ni)Se2 ordered alloy and evaluate this alloy in the same framework. We find that this alloy does not tune the binding energy of OOH* effectively and therefore is not an improvement over the pure phases and should not be pursued synthetically.

4.2 Methods

Methods follow the progression as in Chapter 3 to facilitate comparison.

Spin polarized electronic structure calculations were performed using the Vienna Ab initio Simulation package (VASP)[85,86,83,84] interfaced with the Atomic Simulation Environment (ASE).[6] Projector augmented wave (PAW) pseudopotentials[10,87] with a cutoff of 450 eV were used to treat core electrons, and the Perdew–Burke–Ernzerhof (PBE) functional[135,136] was used to treat exchange and correlation. Dispersion was treated using Grimme's D3(ABC) method.[49] A variety of Hubbard U parameters were tested for *c*-NiS_2 and *c*-(Co,Ni)Se_2 and were found to have little to no effect on the geometries or energies; therefore, no Hubbard U

parameter was used for these catalysts. Solvation effects were treated using the continuum solvent method VASPsol.[107,106] The Brillouin zone was sampled using a (10, 10, 10) and (10, 10, 1) Γ-centered Monkhorst–Pack mesh[131] for bulk and surface calculations, respectively. Lattice constants were determined by fitting to an equation of state (EOS).[3]

The (100) surfaces of *c*-$NiSe_2$ was modelled as a 1 x 1 unit cell slab, leading to a total of 8 Ni atoms and 16 Se atoms. The *c*-(Co,Ni)Se_2 was created by replacing 4 of the Ni atoms in the unit cell with Co atoms and reoptimizing the lattice constant. Both had two repeats in the z-direction and a vacuum gap of at least 15 Å. The top half of the slabs was allowed to relax while the bottom half was frozen to simulate the bulk. For each ionic configuration, the electronic energy was converged below 10^{-6} eV. Both the clean slab and adsorbates were allowed to relax until the forces were converged below 0.005 eV/Å^2. Transition states were located using the nudged elastic band (NEB) method[58,56] and were refined using the dimer method.[57,64,77] All transition states were confirmed saddle points with one imaginary frequency corresponding to bond breaking.

Binding energies were calculated with respect to $O_{2(g)}$ and $H^+_{(aq)}$ and e^-. The energy of $H^+_{(aq)}$ and e^- was calculated using the computational hydrogen electrode (CHE) method,[126] where $H^+_{(aq)}$ is assumed to be in thermodynamic equilibrium with $H_{2(g)}$. In order to avoid well-known errors in the DFT treatment of $O_{2(g)}$, the free energy of $H_{2(g)}$ was determined by matching the experimental standard equilibrium potential (1.229 V) of the reaction $\frac{1}{2}O_{2(g)}$ + $2H^+_{(aq)}$ + $2e^- \rightarrow H_2O_{(l)}$. The free energies of species were calculated using $G = H - TS$, where H is the enthalpy including zero-point energy (ZPE) and thermal corrections, and S is either the total experimental entropy at 298 K and 1 bar (for gas phase species) or calculated under the harmonic approximation (for surface bound species). The free energy of $H_2O_{(l)}$ was calculated using the experimental free energy of formation for $H_2O_{(l)}$ and $H_2O_{(g)}$.The solvation free energy of $H_2O_{2(aq)}$ was calculated using the experimental Henry's law constant.[122]

The calculated standard equilibrium potential of the $2e^-$ ORR reaction $O_{2(g)} + 2\,H^+_{(aq)} + 2e^- \rightarrow H_2O_{2(aq)}$ is 0.81 V, while the experimental standard equilibrium potential is 0.69 V.

4.3 Results and Discussion

4.3.1 $NiSe_2$ Catalyst Performance

$NiSe_2$ exists as a phase pure pyrite structure.[38] Like $CoSe_2$, it is a metal (in contrast to NiS_2 which is a semiconductor and therefore not ideal for electrocatalysis). For a consistency, all results on *c*-$NiSe_2$ are compared to *c*-$CoSe_2$.

Catalyst Stability

According to the Materials Project,[69] (see Figure 4.2), the electrochemical window of stability for *c*-$NiSe_2$ is much wider than *c*-$CoSe_2$, including in both acidic and neutral media. This indicates that *c*-$NiSe_2$ would be more stable and less prone to degradation than the current state-of-the-art $2e^-$ ORR catalyst in acidic media. Additionally, *c*-$NiSe_2$'s wider window of stability in neutral media indicates it should be explored as a $2e^-$ ORR catalyst in neutral media, which is of particular interest for on-site water treatment applications.

Using the derivation for surface Pourbaix diagrams found in Chapter 3.3.2, we construct a surface Pourbaix diagram for *c*-$NiSe_2$ and compare it to that of *c*-$CoSe_2$ (see Figure 4.3. For both surfaces, we investigate the most thermodynamically stable (100) surface. We examine the surface at the experimentally relevant potential range of 0.5 V *vs.* RHE to 0.62 V *vs.* RHE. At 0.5 V, both surfaces are predicted to be clear of adsorbates. At 0.62 V, we expect to start seeing a buildup of OH* on Co sites for *c*-$CoSe_2$. However, on *c*-$NiSe_2$, we expect the surface to remain clear even at 0.62 V. This can be rationalized through large differences in the OH* binding energy to the metal centers. On *c*-$CoSe_2$, OH* has a binding energy to Co sites of -

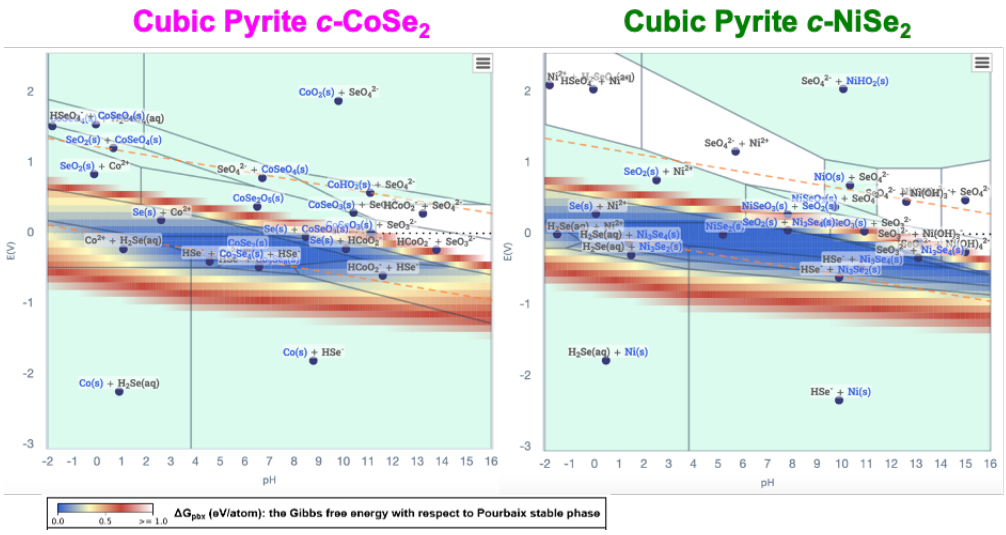

Figure 4.2: Calculated bulk Pourbaix diagrams of (a) *c*-$CoSe_2$ and (b) *c*-$NiSe_2$ assuming an ionic concentration of 10^{-6} mol/kg for each element of interest (which are reasonably low concentrations that can fairly reflect an acidic electrolyte solution of 0.05 M H_2SO_4). These diagrams are adapted from the Materials Project.[69] The multicolor gradient indicates the Gibbs free energy of the compound at a given set of potential and pH conditions with respect to its Pourbaix stable phase (ΔG_{pbx}), reflecting the electrochemical stability window of the compound. It was surmised in a previous report that materials with ΔG_{pbx} up to high values as much as 0.5 eV/atom can persist in electrochemical environments because of the energy barriers for the dissociation reactions.[163] The electrochemical stability windows of both *c*-$NiSe_2$ is much wider than that of *c*-$CoSe_2$.

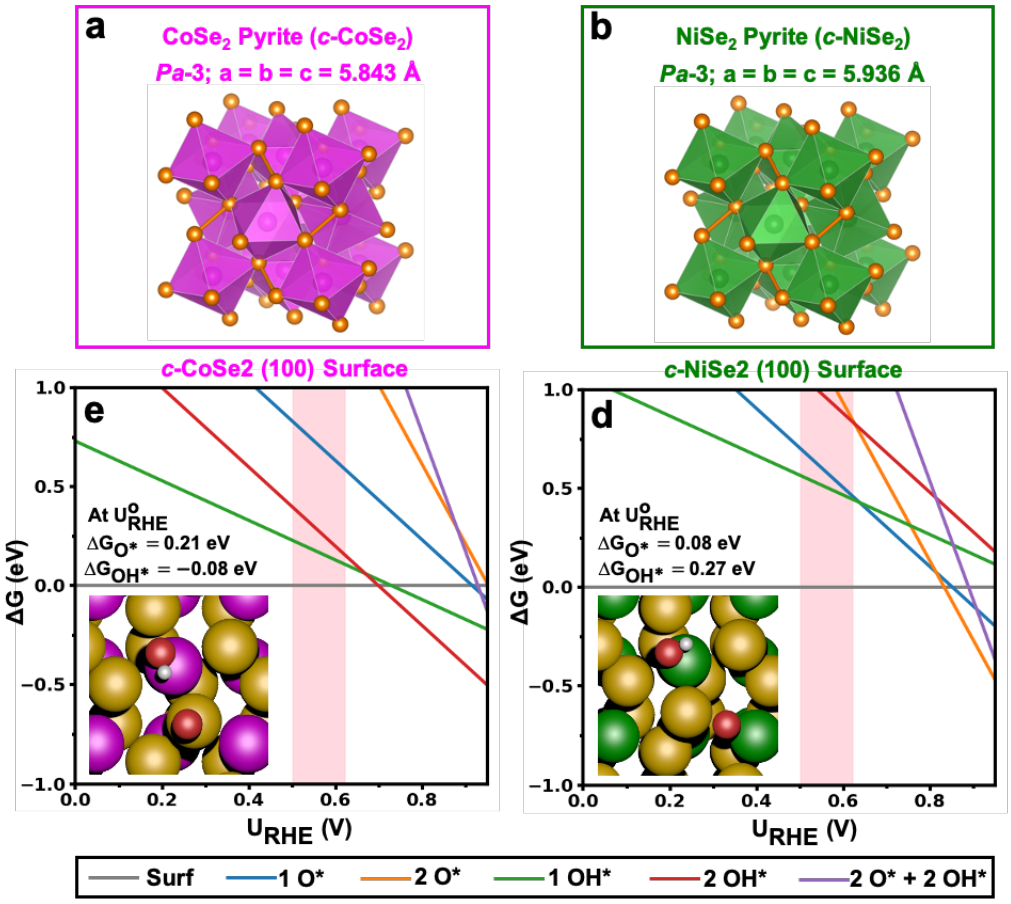

Figure 4.3: Crystal structures and surface Pourbaix diagrams. (a–b) Crystal structures, space groups, and lattice constants of (a) *c*-$CoSe_2$ and (b) *c*-$NiSe_2$. The Co, Ni, and Se atoms are displayed in pink, green, and orange, respectively. (c–d) Calculated surface Pourbaix diagrams (ΔG vs. U_{RHE}) of (c) *c*-$CoSe_2$ (100) and (d) *c*-$NiSe_2$ (100). On *c*-$CoSe_2$, Co and S/Se sites are the preferential binding sites for OH* and O*, respectively. On *c*-$NiSe_2$, Ni is the preferred binding site for both O* and OH*. The preferred binding configuration for 2O* and 2OH* on the surface is 1 O* on Ni and 1 OH* on Ni and the remaining O* and OH* on Se. A wide variety of surface coverages (from clean surface to $\frac{3}{4}$ ML O* + 1 ML OH*) are examined. For the sake of clarity, only the most stable surface coverages in the potential range of 0 to 1 V are shown here. Surface free energies are assumed to be in equilibrium with $H_2O_{(l)}$. The unit cell has two Co binding sites and four S/Se binding sites for a total of 6 binding sites. Binding energies of O* and OH* (ΔG_{O^*} and ΔG_{OH^*}) at the calculated standard equilibrium potential of $2e^-$ ORR (U^o_{RHE}) and top views of the catalyst surfaces with O* and OH* bound to their preferential binding sites are shown as insets. The Co, Ni, Se, O, and H atoms are displayed in pink, green, orange, red, and white, respectively. The highlighted regions in light red represent the experimentally relevant potential range where the optimal H_2O_2 production performances are achieved.

0.08 eV. In contrast, on *c*-$NiSe_2$, OH* has a binding energy to Ni sites of 0.27 eV, a difference of 0.35 eV. This much weaker, endothermic bonding of OH* leads to a cleaner surface at a wider range of potentials.

Another major difference between *c*-$NiSe_2$ and *c*-$CoSe_2$ is the binding site of O*. On *c*-$CoSe_2$, O* weakly binds preferentially to chalcogen sites. In contrast, on *c*-$NiSe_2$, O* preferentially binds to the Ni sites. While the O* binding energy on Ni sites on *c*-$NiSe_2$ is 0.13 eV stronger than on the Se sites of *c*-$CoSe_2$; on both surfaces, O* is very weakly, endothermically bound to the surface. Should O* build up on the surface during the reaction (the Pourbaix diagram predicts equilibrium in the presence of water, not during reaction conditions when $O_{2(g)}$ is present), coverage would have to reach a significant concentration before any species would bind to a chalcogen site on *c*-$NiSe_2$. In contrast, any presence of O* on *c*-$CoSe_2$ would create bonds to the chalogen site immediately. As degradation most likely occurs from the oxidation of selenium (see Figure 4.2), we predict that the change in preferential binding site of O* leads to an increased resistance to degradation for the *c*-$NiSe_2$ catalyst.

Overall, the weakening of the OH* bond to the metal center and the change in the preferential binding site for O* for *c*-$NiSe_2$ indicate a more degradation-resistant catalyst. Additionally, the extended window of electrochemical stability for neutral pHs indicates that the *c*-$NiSe_2$ catalyst should be explored for application of $2e^-$ ORR in neutral media.

Catalyst Activity and Selectivity

To compare the activity and selectivity of *c*-$NiSe_2$ with that of *c*-$CoSe_2$, we calculate the free energy diagrams of the $2e^-$ and competing $4e^-$ ORR pathways. The catalytic activity is controlled by the PCET Reaction in Equations 3.6 and 3.7. At the calculated equilibrium potential of $2e^-$ ORR (U^o_{RHE}), the first PCET step (3.6) on *c*-$CoSe_2$ is moderately downhill by 0.24 eV, indicating a theoretical overpotential of 0.24 V, an overbound OOH* intermediate and a cat-

alyst which fall on the left side of the Sabatier curve (see Figure 4.1). On *c*-$NiSe_2$, the first PCET step is uphill by 0.10 eV, indicating a theoretical overpotential of 0.10 V, an underbound OOH* intermediate and a catalyst on the right side of the Sabatier curve. These theoretical overpotentials indicate that *c*-$NiSe_2$ may have a modestly higher intrinsic activity than *c*-$CoSe_2$.

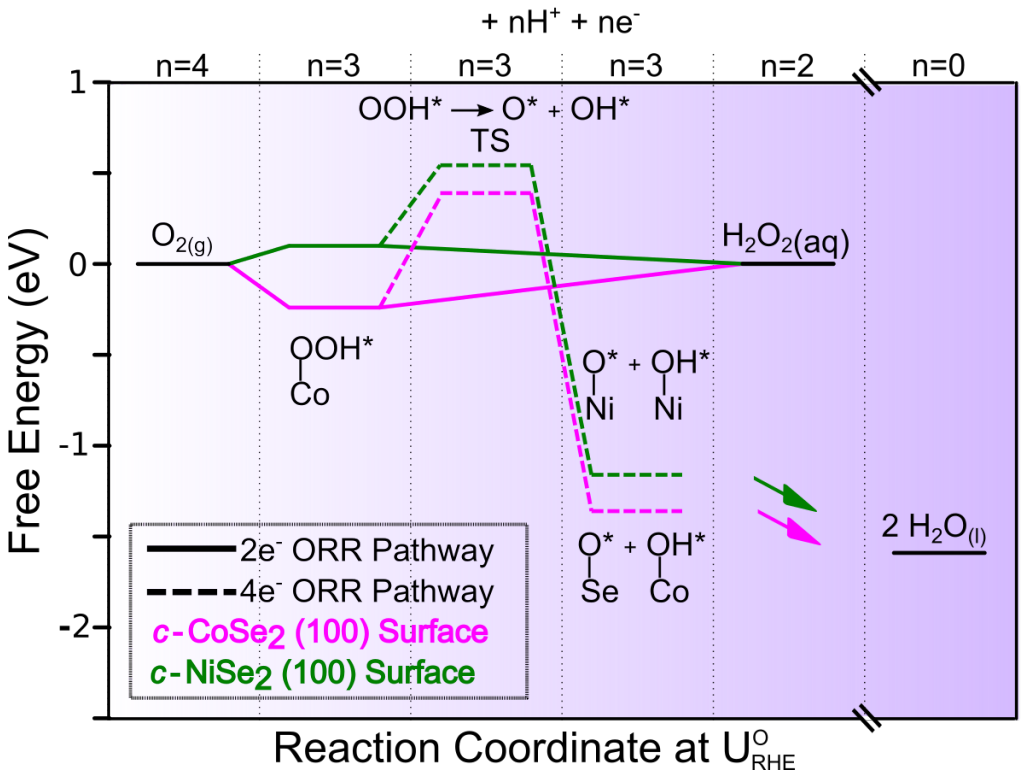

Figure 4.4: Calculated free energy diagrams of $2e^-$ and $4e^-$ ORR pathways. Calculated free energy diagrams were performed on *c*-$CoSe_2$ (100) and *c*-$NiSe_2$ (100) surfaces at the calculated standard equilibrium potential of $2e^-$ ORR (U^o_{RHE}). Possible $2e^-$ and $4e^-$ ORR pathways are depicted in solid and dashed lines, respectively. The traces for *c*-$CoSe_2$ (100) and *c*-$NiSe_2$ (100) surfaces are displayed in pink and green respectively. These calculations are performed on clean surfaces as the binding energies of OOH* are insensitive to other surface adsorbates present on *c*-$CoSe_2$ or *c*-$NiSe_2$ at low overpotentials (see surface Pourbaix diagrams in Figure 4.3).

The selectivity of the catalyst towards the desired $2e^-$ ORR product rather than the thermo-

dynamically more stable $4e^-$ ORR product is controlled by the strength of the O-O bond in OOH* (see Equation 3.8). The stronger the bond, the more resistant the catalyst is towards O-O bond scission. Cleaving the O-O bond in OOH* causes build up of O* and OH* on a catalyst surface, which can either degrade the catalyst or be further reduced to $H_2O_{(l)}$. A strong O-O bond allows OOH* to undergo the second PCET reaction step (see Equation 3.7) and form $H_2O_{2(aq)}$. On *c*-$CoSe_2$, the barrier towards O-O bond cleavage is 0.63 eV and on *c*-$NiSe_2$, this barrier is 0.61 eV. Both of these barriers are sufficiently higher than than those on close-packed metals such as Pd (0.06 eV), Pt (0.16 eV), and Cu (0.06 eV),[34] This is because breaking the O-O bond requires an ensemble of metal sites. For *c*-$CoSe_2$ and *c*-$NiSe_2$, this requires surface reconstruction to move metal centers towards each other which is not required on close-packed metal surfaces. We predict that both catalysts will show similar, high selectivity towards $2e^-$ ORR.

c-$NiSe_2$ demonstrates similar theoretical selectivity and a modest increase in activity compared to *c*-$CoSe_2$. Both these metrics indicate *c*-$NiSe_2$ will be an excellent $2e^-$ catalyst and should be explored experimentally.

4.3.2 (Co,Ni)Se_2 Alloy Catalyst Performance

We have analyzed two very good candidates for $2e^-$ ORR based on our theoretical framework, one (*c*-$CoSe_2$) that falls on the overbound side of the Sabatier curve and one (*c*-$NiSe_2$) that falls on the underbound side of the Sabatier curve (see Figure 4.1). One way to reach the peak of the curve, or the Sabatier optimum, is to alloy two very good catalysts to tune the binding energies and produce one excellent catalyst. As *c*-$CoSe_2$ and *c*-$NiSe_2$ have the same pyrite structure and similar lattice constants (see Figure 4.3), they are perfect materials to alloy together.

From a computational perspective, the simplest *c*-(Co,Ni)Se_2 alloy composition is a 50/50

mixture of Co and Ni. There is also experimental evidence that this structure is synthesizable.[53] Therefore, our theoretical model of *c*-(Co,Ni)Se_2 is a 50:50 *ordered* alloy.

There are three distinct (100) surface terminations created in a *c*-(Co,Ni)Se_2 ordered alloy; one that alternates Co and Ni metal centers on the surface, one that has only Co metal centers on the surface and one that has only Ni metal centers on the surface. These surfaces are depicted in Figure 4.5. All three terminations have very similar surface energies (see Table 4.1); therefore, we calculate binding energies on all three terminations.

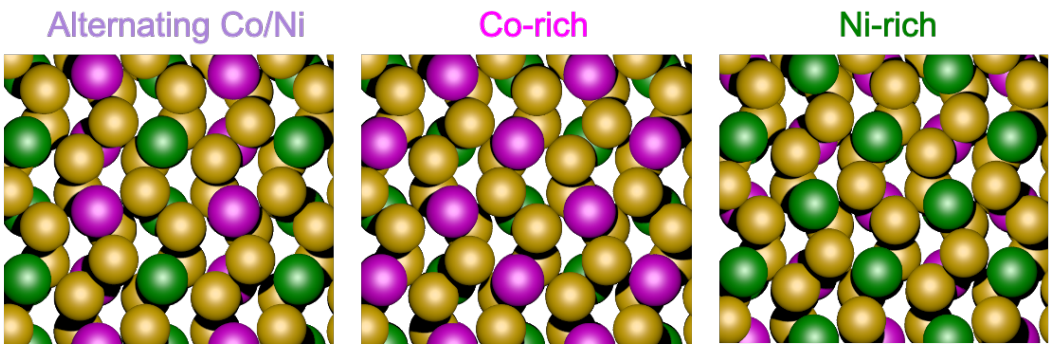

Figure 4.5: (100) surface terminations of the 50:50 *c*-(Co,Ni)Se_2 ordered alloy. (a) (100) surface with alternating Co and Ni metal centers on the surface. (b) (100) surface with only Co metal centers on the surface. (c) (100) surface with only Ni metal centers on the surface. The Co, Ni and Se atoms are displayed in pink, green and orange respectively.

Table 4.1: Surface energies of the three (100) surface terminations for the 50:50 *c*-(Co,Ni)Se_2 ordered alloy.

Termination	Surface Energy (ev/Å^2)
Alternating Co/Ni	0.0430
Co-rich	0.0426
Ni-rich	0.0429

Our previous analysis has concluded that stability can be predicted by the binding strength and binding site of O* and OH* and that activity can be controlled by the binding strength of OOH*. Based on Brønstead-Evans-Polanyi relations,[146] we predict that the O-O bond strength

in the alloy should be between the strength of the bond in *c*-$CoSe_2$ and *c*-$NiSe_2$. As both these alloys show similar resistance to O-O bond cleavage, we expect that the alloy will show similar selectivity trends. Therefore, we do not calculate the barrier to O-O bond cleavage of OOH* on the alloy but rather focus on the binding of O*, OH* and OOH* as it is with these binding energies and binding sites that we see dissimilarities in the catalysts and thus expect to find changes in the alloy.

Table 4.2: DFT calculated binding energies and binding sites of O*, OH* and OOH* on the three (100) surface terminations of the 50:50 *c*-(Co,Ni)Se_2 ordered alloy. Binding energies on the pure *c*-$CoSe_2$ and *c*-$NiSe_2$ are provided for reference.

	Alternating Co/Ni		Co-rich		Ni-rich		*c*-$CoSe_2$		*c*-$NiSe_2$	
Species	site	energy (eV)	site	energy (eV)	site	energy (eV)	site	energy (eV)	site	energy (eV)
O*	Ni	0.08	Se	0.30	Ni	0.04	Se	0.21	Ni	0.08
OH*	Co	-0.09	Co	-0.10	Se	0.51	Co	-0.08	Ni	0.27
OOH*	Co	-0.30	Co	-0.30	Ni	0.03	Co	-0.24	Ni	0.10

The calculated binding energies of O*, OH* and OOH* as well as their binding sites on all three surface terminations can be found in Table 4.2. OOH* binds preferentially to a Co site on both terminations with Co sites available with a binding energy of -0.30 eV. This over-bound binding energy is very similar to the OOH* binding energy of -0.24 eV on *c*-$CoSe_2$. On the Ni rich surface, OOH* binds to the Ni sites with a binding energy of 0.03 eV. This is a slight improvement over the binding energy of 0.10 eV on *c*-$NiSe_2$. Based on OOH* binding energies, the Ni-rich termination will show improved activity over *c*-$CoSe_2$ and *c*-$NiSe_2$ but the other two terminations will show lessened activity.

O* binds to Ni, its preferential binding site, when available. On the alternating Co/Ni and Ni-rich terminations, O* binds to Ni with a binding energy of 0.08 eV and 0.04 eV, respecitvely, similar to the binding energy of 0.08 eV on *c*-$NiSe_2$. When Ni sites are not available, as on the Co-rich termination, O* binds preferentially to Se with a binding energy of 0.30 eV, similar to *c*-$CoSe_2$ which has an O* binding energy of 0.21 eV on Se sites.

On terminations where Co sites are available, OH* preferentially binds to them, with a binding energy of -0.09 eV and -0.10 eV on the alternating Co/Ni and Co-rich terminations respectively. This is very similar to the (100) surface of *c*-$CoSe_2$ which binds OH* to Co sites with a binding energy of -0.08 eV. On the Ni-rich termination, OH* binds to Se sites with a binding energy of 0.51 eV. While this is a different binding site when compared to the (100) surface of *c*-$NiSe_2$ (which binds OH* to Ni sites with a binding energy of 0.27 eV), both the Ni-rich termination and *c*-$NiSe_2$ show such weak OH* binding that we expect little to no OH* buildup regardless of the binding site on both Ni catalysts.

Overall, we find that the Co-rich surface binds adsorbates in a similar manner to the *c*-$CoSe_2$ (100) surface and the Ni-rich surface binds adsorbates similarly to the *c*-$NiSe_2$ (100) surface. The alternating Co-Ni termination has preferential binding to the metal centers; OH* and OOH* on Co and O* on Ni, in accordance with their preferred binding sites on the non-alloyed (100) catalyst surfaces.

Very little of any species binds to the Ni-rich termination and the OOH* binding energy has shifted closer to 0 eV. This indicates that this termination would be very stable and active. However, the two other terminations have large OOH* binding energies and are more likely to suffer from buildup of O* and OH*, indicating a less active *and* less stable $2e^-$ ORR catalyst. Therefore, unless an experimentalist can control the surface termination (perhaps by degrading a Co-rich top layer and exposing a less reactive Ni-rich termination), this alloy will not lead to a better $2e^-$ ORR catalyst.

The absence of significant changes in binding energies when alloying Co and Ni dichalcogenides indicates that neighboring metal centers have little electronic influence on each other. Alloying metal centers, therefore, offers little as an avenue for rational catalyst design.

4.4 Conclusion

We investigated the *c*-$NiSe_2$ catalyst for $2e^-$ ORR using the theoretical framework developed in Chapter 3. We evaluated the catalyst for stability, activity and selectivity. We found weak binding of adsorbates to the catalyst surface in the experimentally relevant potential range. The O* binding site changes from the chalcogen to the metal center, leaving little adsorbate buildup on the chalcogen. As oxidation of the chalcogen is believed to lead to catalyst degradation, this indicates these changes in energetics and binding sites will lead to an improved catalyst. Additionally, the bulk Pourbaix diagram indicates that not only does the *c*-$NiSe_2$ exhibit a wide window of electrochemical stability in acidic pHs, it also has a wide range of stability in the neutral pH range. Therefore, this catalyst shows great promise for 2 e^- ORR in neutral media.

The OOH* binding energy shows that OOH* is slightly underbound, indicating that *c*-$NiSe_2$ lies on the other side of the Sabatier curve than *c*-$CoSe_2$. The OOH* binding energy is closer to 0 eV on *c*-$NiSe_2$, predicting a slight increase in intrinsic activity. The barrier towards cleaving the O-O bond in OOH* is sufficiently high at room temperature to predict a selective $2e^-$ ORR catalyst. Therefore, based on the stability, activity and selectivity, we recommend experimentally investigating *c*-$NiSe_2$ for $2e^-$ ORR in acidic and neutral media.

To improve two catalysts that are on opposite sides of the Sabatier optimum, we theoretically model a 50:50 ordered alloy of *c*-(Co,Ni)Se_2. We investigate three (100) surface terminations with similar surface energy: alternating Co/Ni, Co-rich and Ni-rich. We find that the metal centers have little electronic influence over neighboring metal centers and therefore binding energies of species on each metal site are similar to the binding energy of the species on the metal site in the pure compound, thus giving little catalytic improvement. The Ni-rich layer shows a slight activity improvement over *c*-$NiSe_2$, however the other two terminations

show worse activity and therefore we do not predict that the *c*-(Co,Ni)Se_2 ordered alloy is an improvement over the two separate pure compounds.

Although the metal centers are not influenced electronically by neighboring metal centers, perhaps the chalcogen could modulate the binding energy of the metal center. As pyrite disulfides are known to degrade more quickly than pyrite selenides, we anticipate alloying with sulfur will decrease stability. However, alloying with Te may create an electronic environment to maximize stability, activity and selectivity. Further investigations into *c*-Ni(Se,$Te)_2$ and *c*-Co(Se,$Te)_2$ alloys offer a fruitful avenue of further investigation.

5

Electrochemical Microkinetic Model of $2e^-$ ORR on Cobalt Dichalcogenide Catalysts

Reproduced in part with permission from Sheng, H., Janes, A. N., Ross, R. D., Kaiman, D., Huang, J., Song, B., Schmidt, J. R., Jin, S. (2020). *Stable and selective electrosynthesis of hydrogen peroxide and the electro-Fenton process on $CoSe_2$ polymorph catalysts*. Energy & Environmental Science. 2020, **13**, 4189-4203.

ANJ performed all theoretical modeling. Electrochemical experiments was performed by HS and RDR.

5.1 Introduction

Currently, H_2O_2 is produced through the anthroquinone process, a methodology that produces up to 70 wt% concentrated solutions of H_2O_2.[17] Not only is this concentration both hazardous to transport and store, but most industrial applications, such as water treatment, medical disinfection, and household sanitation require much lower concentrations of H_2O_2. For example, a concentration less than 1000 ppm (29 mM) is sufficient for water treatment.[196] The electrochemical synthesis of H_2O_2 offers an opportunity to efficiently produce H_2O_2 *in situ* on demand.

In Chapter 3, we investigated cobalt dichalcogenides and concluded that based on the activity, selectivty and stability parameters, *o*-$CoSe_2$ is the best $2e^-$ ORR catalyst in acid reported to date. However, both our selectivity metric and RRDE measurements implicitly assume that all H_2O_2 produced is usable for industrial applications and ignore the possible electrochemical side reactions of H_2O_2 at higher H_2O_2 concentrations that drive the reduction of H_2O_2 to H_2O. In order to fully understand catalyst performance for $2e^-$ ORR, we must evaluate if the catalyst can accumulate 29 mM $H_2O_{2(aq)}$ and if the catalyst is resistant to reduction of H_2O_2 to H_2O.

To evaluate our cobalt dichacogenide catalysts for these two additional metric, our experimental collaborators performed bulk electrolysis to produce H_2O_2 using integrated electrodes

of *o*-$CoSe_2$ and *c*-CoS_2 nanowires directly grown on three-dimensional carbon fiber paper substrates (CFP) and carried out chemical detection of the produced H_2O_2 via redox titration using cerium(IV) sulfate ($2\,Ce^{4+} + H_2O_2 \rightarrow 2\,Ce^{3+} + 2\,H^+ + O_2$) monitored by UV-Vis spectrophotometry.[96]

The bulk electrosynthesis of H_2O_2 on *o*-$CoSe_2$/CFP and *c*-CoS_2/CFP was carried out in O_2-saturated 0.05 M H_2SO_4 solution (4 mL) at the constant potential of 0.5 V vs. RHE, near the optimal potential where the maximum $j_{peroxide}$ was achieved from RRDE measurements, over long periods of time (5–6 h, see Figure 5.1). As the H_2O_2 product was accumulated in the solution, the overall catalytic current of *o*-$CoSe_2$/CFP displayed a Nernstian response (Figure 5.1a red curve). In contrast, the overall catalytic current of *c*-CoS_2/CFP only exhibited an initial Nernstian response immediately after the bulk electrolysis started and then gradually increased as the bulk electrolysis proceeded (Figure 5.1a blue curve). During the bulk electrolysis using *o*-$CoSe_2$/CFP, the cumulative H_2O_2 concentration kept increasing and reached a high concentration of 547 ppm after 6 h (Figure 5.1b red curve). As for *c*-CoS_2/CFP, despite delivering a larger overall catalytic current, the cumulative H_2O_2 concentration increased less steadily and reached a maximum of only 232 ppm over 3 h and then started decreasing afterwards (Figure 5.1b blue curve). We further calculated the cumulative H_2O_2 yield on both electrodes taking into account the evaporation of electrolyte solution during bulk electrolysis: the cumulative H_2O_2 yield on *o*-$CoSe_2$/CFP consistently increased to 33.7 μmol over 6 h, whereas that on *c*-CoS_2/CFP peaked at the 3 h mark with only 19.6 μmol (Figure 5.1c). As a result, the cumulative H_2O_2 selectivity on *o*-$CoSe_2$/CFP reached 83% during the first hour of bulk electrolysis and still remained 70% over the long period of 6 h, whereas the selectivity on *c*-CoS_2/CFP started off with a lower value of 60% and drastically decreased to 13% over 5 h (see Figure 5.1d). Moreover, ICP-MS analysis of the tested electrolyte solutions (see inset of Figure 5.1a) showed that *o*-$CoSe_2$/CFP exhibited an average cobalt leaching rate of

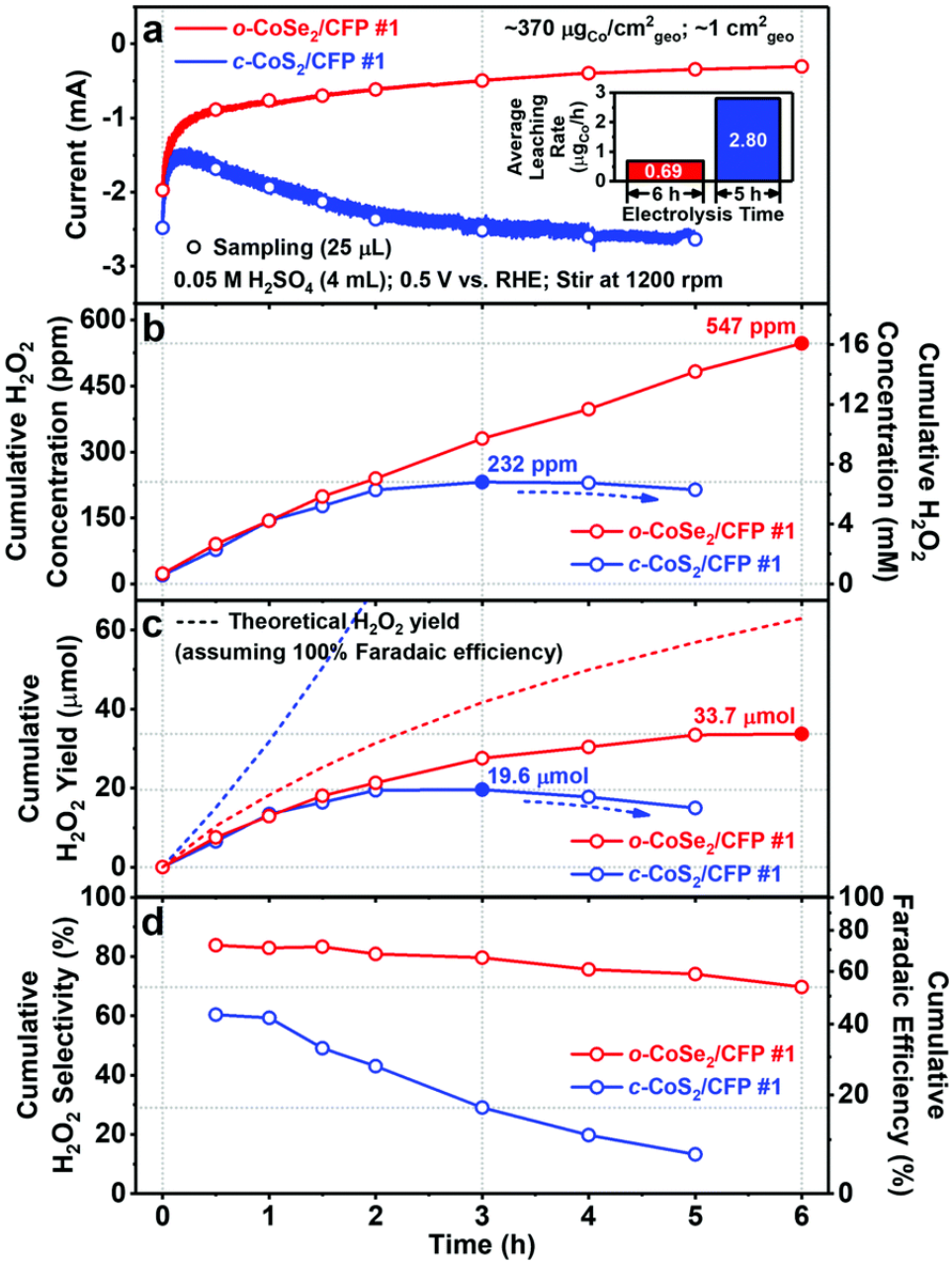

Figure 5.1: Bulk electrosynthesis and chemical detection of H_2O_2 produced on *o*-$CoSe_2$/CFP in comparison with *c*-CoS_2/CFP. (a) Chronoamperometry curves of *o*-$CoSe_2$/CFP and *c*-CoS_2/CFP (with the same catalyst loading of 370 $\mu g_{Co}/cm^2$geo and the same geometric area of 1 cm^2geo) at 0.5 V vs. RHE in O_2-saturated 0.05 M H_2SO_4 solution (pH 1.20) under vigorous stirring (1200 rpm). The average cobalt leaching rates (μg_{Co}/h) of *o*-$CoSe_2$/CFP and *c*-CoS_2/CFP during bulk electrolysis is shown as an inset. (b) Cumulative H_2O_2 concentration, (c) cumulative H_2O_2 yield, and (d) cumulative H_2O_2 selectivity and Faradaic efficiency during bulk electrolysis.

0.69 μg_{Co}/h over 6 h, much lower than that of *c*-CoS_2/CFP (2.80 μg_{Co}/h over 5 h). In fact, since the Co^{2+} leaching from $CoSe_2$ took place mostly at the initial stage of electrochemical operations, this average leaching rate of 0.69 μg_{Co}/h could be a lower bound estimate of the operational stability of *o*-$CoSe_2$/CFP. These observations also led us to suspect that electrochemical side reactions of H_2O_2 reduction and/or decomposition were much more pronounced on *c*-CoS_2/CFP and eventually out-competed the H_2O_2 production, which could account for the abnormal increase in the overall current (Figure 5.1a) and the significant decrease in the H_2O_2 selectivity (Figure 5.1d) during the bulk electrolysis using *c*-CoS_2/CFP.

Additional bulk electrolysis experiments were designed to prove that the electrochemical side reactions of H_2O_2 reduction and/or decomposition are indeed much less prone on *o*-$CoSe_2$/CFP. We reason that the additional catalytic current triggered by those side reactions should correlate with the H_2O_2 concentration. Therefore, after accumulating an appreciable concentration of H_2O_2 from the bulk electrolysis using *o*-$CoSe_2$/CFP, we reintroduced fresh H_2O_2-free electrolyte solution and performed another bulk electrolysis reusing the same *o*-$CoSe_2$/CFP electrode. The overall catalytic current of *o*-$CoSe_2$/CFP in the H_2O_2-free solution was identical to that in the H_2O_2-containing solution, suggesting *o*-$CoSe_2$/CFP is highly resistant to the electrochemical side reactions that consume the H_2O_2 product. In contrast, *c*-CoS_2/CFP behaved very differently in the analogous experiments. The overall catalytic current of *c*-CoS_2/CFP in the H_2O_2-containing solution was substantially greater than that in the fresh H_2O_2-free solution, resulting in the significant loss of H_2O_2 product due to the prevalence of side reactions. Therefore, *o*-$CoSe_2$/CFP is much more effective than *c*-CoS_2/CFP for the bulk electrosynthesis production of H_2O_2 at industrially relevant concentrations.

In this work, we use a theoretical microkinetic model to model the entire reaction network to understand the maximum H_2O_2 accumulation and the flux through the pathways that reduce H_2O_2. At steady state, the concentration of $H_2O_{2(aq)}$ is the theoretical maximum yield

of H_2O_2. $2e^-$ ORR catalysts prone to reduction of H_2O_2 will show high flux through reaction pathways that will lead to the decomposition of H_2O_2. We compare our theoretical results to the bulk electrolysis experiments detailed above. By modeling $2e^-$ ORR on these cobalt dichalcogenide catalysts and comparing the results to the bulk electrolysis study, we can both validate our theoretical methodology and create transferable physical principles for why *o*-$CoSe_2$ is a superior $2e^-$ ORR. This validated methodology and any transferable physical principles can then be used to screen new $2e^-$ ORR catalysts without labor intensive bulk electrolysis experiments.

We modify our microkinetic modeling code, Micki, (detailed in Chapter 1) to model electrochemical reactions. We then build microkinetic models of *c*-$CoS_2$and *o*-$CoSe_2$ and analyze both the steady state solution of the coupled differential rate equations and the initial rates of reactions. We find that both *c*-CoS_2 and *o*-$CoSe_2$ catalysts accumulate H_2O_2 at concentrations significantly higher than needed for industrial applications (>29mM) and are in agreement with the experimental result that *c*-CoS_2 undergoes further reduction of H_2O_2 while the selenide catalysts do not.

5.2 Methods

5.2.1 Density Functional Theory

Our DFT calculations are performed at the same level of theory as outlined in Chapter 3. Spin polarized electronic structure calculations were performed using the Vienna Ab initio Simulation package (VASP)[85,86,83,84] interfaced with the Atomic Simulation Environment (ASE).[6] Projector augmented wave (PAW) pseudopotentials[10,87] with a cutoff of 450 eV were used to treat core electrons, and the Perdew–Burke–Ernzerhof (PBE) functional[135,136] was used to treat exchange and correlation. Dispersion was treated using Grimme's D3(ABC) method.[49]

To better describe the Co 3d electrons in *c*-$CoSe_2$, a Hubbard U parameter,[4] U_{eff} = 2.0 eV, was taken from a previous report.[191] A variety of Hubbard U parameters were tested for *c*-CoS_2 and *o*-$CoSe_2$, and were found to have little to no effect on the geometries or energies; therefore, no Hubbard U parameter was used for these two catalysts. Solvation effects were treated using the continuum solvent method VASPsol.[107,106] The Brillouin zone was sampled using a (10, 10, 10) and (10, 10, 1) Γ-centered Monkhorst–Pack mesh[131] for bulk and surface calculations, respectively. Lattice constants were determined by fitting to an equation of state (EOS).[3]

The (100) surfaces of *c*-CoS_2 and *c*-$CoSe_2$ and the (101) surface of *o*-$CoSe_2$ were modelled as a 1 x 1 unit cell slab with two repeats in the z-direction, leading to a total of 8 Co atoms and 16 S/Se atoms and a vacuum gap of at least 15 Å. The top half of the slabs was allowed to relax while the bottom half was frozen to simulate the bulk. For each ionic configuration, the electronic energy was converged below 10^{-6} eV. Both the clean slab and adsorbates were allowed to relax until the forces were converged below 0.005 eV/Å^2. Transition states were located using the nudged elastic band (NEB) method[58,56] and were refined using the dimer method.[57,64,77] All transition states were confirmed saddle points with one imaginary frequency corresponding to bond breaking.

Binding energies were calculated with respect to $O_{2(g)}$ and $H^+_{(aq)}$ and e^-. The energy of $H^+_{(aq)}$ and e^- was calculated using the computational hydrogen electrode (CHE) method,[126] where $H^+_{(aq)}$ is assumed to be in thermodynamic equilibrium with $H_{2(g)}$. In order to avoid well-known errors in the DFT treatment of $O_{2(g)}$, the free energy of $H_{2(g)}$ was determined by matching the experimental standard equilibrium potential (1.229 V) of the reaction $\frac{1}{2}O_{2(g)}$ + $2H^+_{(aq)}$ + $2e^- \rightarrow H_2O_{(l)}$. The free energies of species were calculated using $G = H - TS$, where H is the enthalpy including zero-point energy (ZPE) and thermal corrections, and S is either the total experimental entropy at 298 K and 1 bar (for gas phase species) or calculated under the harmonic approximation (for surface bound species). The free energy of $H_2O_{(l)}$ was

calculated using the experimental free energy of formation for $H_2O_{(l)}$ and $H_2O_{(g)}$.The solvation free energy of $H_2O_{2(aq)}$ was calculated using the experimental Henry's law constant.[122] The calculated standard equilibrium potential of the $2e^-$ ORR reaction $O_{2(g)} + 2\,H^+_{(aq)} + 2e^- \rightarrow H_2O_{2(aq)}$ is 0.81 V, while the experimental standard equilibrium potential is 0.69 V.

We calculate proton coupled electron transfer (PCET) barriers using the methodology developed by Nie et. al. in reference 121. Briefly, for a given PCET reaction, first we use our normal DFT methods to calculate the barrier of the reaction:

$$A^* + H^* \longrightarrow AH^* + * \tag{5.1}$$

We define the barrier of this reaction as E^o_{act}. For the chemical reaction, $A^* + H^+ + e^- \longleftrightarrow AH^* + H^*$, the free energy of the reaction is defined as:

$$\Delta G = G_{AH^*} - G_{A^*} - \left(\frac{1}{2}G_{H_2} - eU\right) \tag{5.2}$$

When ΔG is 0, $eU = eU^o$. Then eU^o is

$$eU^o = G_{AH^*} - G_{A^*} - \frac{1}{2}G_{H_2} \tag{5.3}$$

Then, using the formalism of Butler-Volmer kinetics, we can extrapolate the reaction barrier as a function of potential:

$$E_{act}(U) = E^o_{act}(U^o) + \beta(U - U^o) \tag{5.4}$$

where β is the symmetry factor and predicts if a reaction is late or early. We will assume that β is 0.5 for all PCET reactions.

5.2.2 Microkinetic Model

In order to model electrochemical reactions, we create three new classes of thermodynamic objects in Micki. The first two, shomate gas and shomate liquid, add in the ability to calculate entropies of fluid phase species using experimental entropies and extrapolate those entropies from 298.15 K to a range of temperatures through the shomate equation. Shomate constants were taken from NIST.[122] The third class is the PCET class. Based on the computational hydrogen electrode (CHE),[127] this class takes the energy of H_2 gas as an input and calculates the energy of a PCET object as

$$G_{PCET} = 0.5G_{\mathrm{H}_{2(g)}} - U \tag{5.5}$$

where U is the potential in V *vs* RHE and can be set in the main script and varied to explore the potential dependence of the reaction.

The reactor was modeled as an idealized continuous stirred- tank reactor (CSTR) as described in 1.5.4 at 298.15 K, pH of 1 and a potential of 0.5 V *vs* RHE. The gas- and solution-phase concentrations of all reactants and products were fixed at their initial values except H_2O_2 which was allowed to accumulate in solution. For steady state analysis, the coupled differential equations were solved until the rates of change of all concentrations and coverages were less than $1 \times 10^{-6} s^{-1}$. For initial rates analysis, the coupled differential equations were solved with a time step of 0.216 seconds/step for 100,000 steps and a total time of 6 hours. Adsorbate-adsorbate interactions are treated as described in Chapter 2. Solution phase species are treated using the diffusion model derived in Chapter 1. Cobalt and sulfur sites are treated as distinct adsorption sites. All species are bound to cobalt sites except O*, which binds to sulfur or selenium sites. Rate constants for adsorption of fluid phase species are calculated using the diffusion model outline in Chapter 1 and depicted in Figure 1.2.

We estimate the concentration of active catalyst sites from experimentally determined electrochemically active surface area (ECSA). The ECSA is defined as

$$ECSA = \frac{C_{dl}}{C_s} \tag{5.6}$$

where C_{dl} (mF) is the experimentally determined double layer capacitance and C_s (mF cm^{-2}) is the specific capacitance. Because the specific capacitance is difficult to determine experimentally, we use the literature value, C_s = 0.035 mF cm^{-2} in 1M H_2SO_4.[109] As the experimental concentration of H_2SO_4 is lower than 1M, we expect the C_s is an overestimate.

Table 5.1: Steady state concentrations for all adsorbates considered in our model on the two cobalt dichalcogenide surfaces.

Sample	Catalyst Loading ($\mu g_{Co}/cm^2_{geo}$)	ECSA (cm^2)	Active Sites (μM)
c-CoS_2/CFP	370	15.8	4.39
o-$CoSe_2$/CFP	370	28.8	6.79

ECSA values are reported in Table 5.1. From ECSA measurements, we can calculate concentration of active sites in molarity by using the size of our computational unit cell, which has two cobalt active sites and the volume of solution used experimentally. This value of concentration of active sites sets the number of active sites in the microkinetic model.

5.3 Discussion and Results

Ten reactions, including two adsorption reactions, three thermal reactions and five PCET reactions are included in the reaction network. We do not consider H_2O adsorbed to the surface. As a closed shell species, H_2O is expected to weakly bind to the surface. However, because our methodology cannot capture the strength of the hydrogen bonding network that is broken

when H_2O desolvates and binds to the surface, our DFT calculations predict too large of H_2O binding energies. To alleviate this, we choose to model all H_2O as $H_2O_{(l)}$. DFT calculated PCET barriers and eU^o values are found in Table 5.2. Free energies of reaction and barriers on the pristine surface are found in Table 5.3. Steady state reaction free energies, barriers and rates are found in Table 5.4. Surface coverages for the catalysts are in Table 5.5.

Table 5.2: DFT forward free energy barriers for all PCET reactions considered in the microkinetic model calculated using Equation 5.1 and eU^o calculated using Equation 5.3 on the two cobalt dichalcogenide catalysts .

	c-CoS_2		o-$CoSe_2$	
Reaction	$\Delta G^{\ddagger}_{\text{for}}$ (eV)	eU^o (eV)	$\Delta G^{\ddagger}_{\text{for}}$ (eV)	eU^o (eV)
$O* + H* \leftrightarrow OH* + *$	1.48	0.49	1.14	1.18
$OH* + H* \leftrightarrow H_2O* + *$	0.99	0.71	1.13	0.70
$O_2* + H* \leftrightarrow OOH* + *$	0.72	0.68	0.78	0.69
$H_2O_2* + H* \leftrightarrow H_2O* + OH*$	0.44	2.47	0.36	3.00
$OOH* + H* \leftrightarrow H_2O_2* + *$	1.14	2.28	1.19	2.02

At steady state, c-CoS_2 has a surface highly covered in O^*, in agreement with surface Pourbaix diagrams (see Figure 3.2. $O_{2(g)}$ adsorbs and then immediately undergoes the first PCET reaction (Equation 3.6). More than 99% of the $O_{2(g)}$ that went through Equation 3.6 then reacts through the second PCET reaction (Equation 3.7) to form $H_2O_{2(aq)}$. However, the $H_2O_{2(aq)}$ readsorbs, the O-O bond is broken and $2OH^*$ are formed on the surface. The OH^* then undergo a PCET reaction to form $H_2O_{(l}$. In solution, 40.9 mM $H_2O_{2(aq)}$ has accumulated. We note here that our microkinetic model does not model degradation of the catalyst surface and previous experimental and theoretical evidence shows significant catalyst degradation for sulfur dichalcogenides; therefore this accumulation is the maximum theoretical accumulation

Table 5.3: Free energies of reaction and forward free energy barriers for all the reactions considered in the microkinetic model on the pristine catalyst on the two cobalt dichalcogenide catalysts. Missing values for $\Delta G^{\ddagger}_{\text{for}}$ indicate that the reaction is barrierless. PCET reactions without a barrier indicate that at a potential of 0.5 V vs RHE, the reaction is barrierless.

	c-CoS_2		*o*-$CoSe_2$	
Reaction	ΔG (eV)	$\Delta G^{\ddagger}_{\text{for}}$ (eV)	ΔG (eV)	$\Delta G^{\ddagger}_{\text{for}}$ (eV)
$O_{2(g)} + * \longleftrightarrow O_2*$	−0.29		−0.36	
$H_2O_{2(aq)} + * \longleftrightarrow H_2O_2*$	0.25		0.22	
$O_2* + * \longleftrightarrow 2\,O*$	−1.91	0.39	−0.59	0.84
$OOH* + * \longleftrightarrow O* + OH*$	−1.72	0.49	−1.08	1.00
$H_2O_2* + * \longleftrightarrow 2\,OH*$	−1.92		−2.02	
$O* + H^+ + e^- \longleftrightarrow OH*$	0.01	0.90	−0.68	0.53
$OH* + H^+ + e^- \longleftrightarrow H_2O_{(l)} + *$	−0.22		−0.16	0.89
$O_2* + H^+ + e^- \longleftrightarrow OOH*$	−0.18		−0.20	0.66
$H_2O_2* + H^+ + e^- \longleftrightarrow H_2O_{(l)} + OH*$	−2.14		−2.17	
$OOH* + H^+ + e^- \longleftrightarrow H_2O_{2(aq)} + *$	−0.04	0.49	0.04	

Table 5.4: Free energies of reaction, forward free energy barriers and reaction rates for all the reactions considered in the microkinetic model under steady state conditions on the two cobalt dichalcogenide catalysts. Missing values for $\Delta G^{\ddagger}_{\text{for}}$ indicate that the reaction is barrierless.

	c-CoS_2			o-$CoSe_2$		
Reaction	ΔG (eV)	$\Delta G^{\ddagger}_{\text{for}}$ (eV)	Rate (s^{-1})	ΔG (eV)	$\Delta G^{\ddagger}_{\text{for}}$	Rate (s^{-1}) (eV)
$O_{2(g)} + * \longleftrightarrow O_2*$	0.56		1.449	−0.36		0.005
$H_2O_{2(aq)} + * \longleftrightarrow H_2O_2*$	−0.02		1.449	0.22		0.003
$O_2* + * \longleftrightarrow 2\,O*$	−0.63	0.27	0.000	−0.55	0.87	0.000
$OOH* + * \longleftrightarrow O* + OH*$	−1.82	0.47	0.000	−1.05	1.01	0.000
$H_2O_2* + * \longleftrightarrow 2\,OH*$	−1.06		1.449	−2.00		0.000
$O* + H^+ + e^- \longleftrightarrow OH*$	0.30	1.18	0.000	−0.69	0.53	0.000
$OH* + H^+ + e^- \longleftrightarrow H_2O_{(l)}*$	−0.51		2.898	−0.17	0.87	0.003
$O_2* + H^+ + e^- \longleftrightarrow OOH*$	−0.63		1.449	−0.19	0.66	0.005
$H_2O_2* + H^+ + e^- \longleftrightarrow H_2O_{(l)} + OH*$	−1.57		0.000	−2.17		0.003
$OOH* + H^+ + e^- \longleftrightarrow H_2O_{2(aq)} + *$	−0.43		1.449	0.04		0.005

Table 5.5: Steady state concentrations as a percentage of surface sites for all adsorbates considered in our model on the two cobalt dichalcogenide surfaces.

	Coverage	
Species	c-CoS_2	o-$CoSe_2$
$O*$	0.659	0.006
O_2*	< 0.001	< 0.001
$OH*$	< 0.001	0.333
$OOH*$	< 0.001	< 0.001
H_2O_2*	< 0.0001	0.000
$*^{\text{Co}}$	0.3333	< 0.001
$*^{\text{S/Se}}$	0.007	0.661

assuming surface degradation does not occur. Our results are consistent with experimental evidence that reduction of H_2O_2 to H_2O is a problem for *c*-CoS_2. RRDE overpredicts the selectivity of *c*-CoS_2 and selectivity is controlled not only by the the strength of the O-O bond in OOH^* but also by the rate of H_2O_2 adsorption and subsequent reduction.

Consistent with the surface Pourbiax diagrams (see Figure 3.2), on *o*-$CoSe_2$ we see a high surface coverage of OH^* (33.30%) and a low coverage of O^* (0.60%). At steady state, we see an accumulation of $H_2O_{2(aq)}$ of 9.18 mM, the necessary order of magnitude of accumulation required for industrial applications. We also see very low rates of H_2O_2 reducing to H_2O, in agreement with experimental evidence that *o*-$CoSe_2$ is highly resistant to those electrochemical side reactions that consume the H_2O_2 product.

To validate that our results match experimental trends, we analyze both the consumption of electrons per site per second and the accumulation of H_2O_2 in solution over time and compare the results to experiment (see Figure 5.1 panels a and b). Our theoretical results are shown in Figure 5.2. We changed the sign of the theoretical rates of electron consumption to match the sign of the experimental current.

First, we must establish a relationship between experimental current in mA to the number of electrons produced per site per second (which is the sum of the rates of all PCET reactions). In one Ampere of current, there are 6.242×10^{18} electrons flowing per second. Based on experimental ECSA, there are 15.8 cm^2 of active sites. Using our theoretical unit cell, which has 2 active cobalt sites, we estimate that 1 mA of current is approximately 1 e^- per site per second and therefore compare the two numbers directly. We emphasize here that there are significant estimations for both the theoretical results and the experimental ECSA values and therefore we expect qualitative, not quantitative, comparisons.

Comparing rates over time, we see that the theoretical rate of consumption curve (see Figure 5.2a) matches the qualitative shape of the experimental curves (see Figure 5.1a). The rate

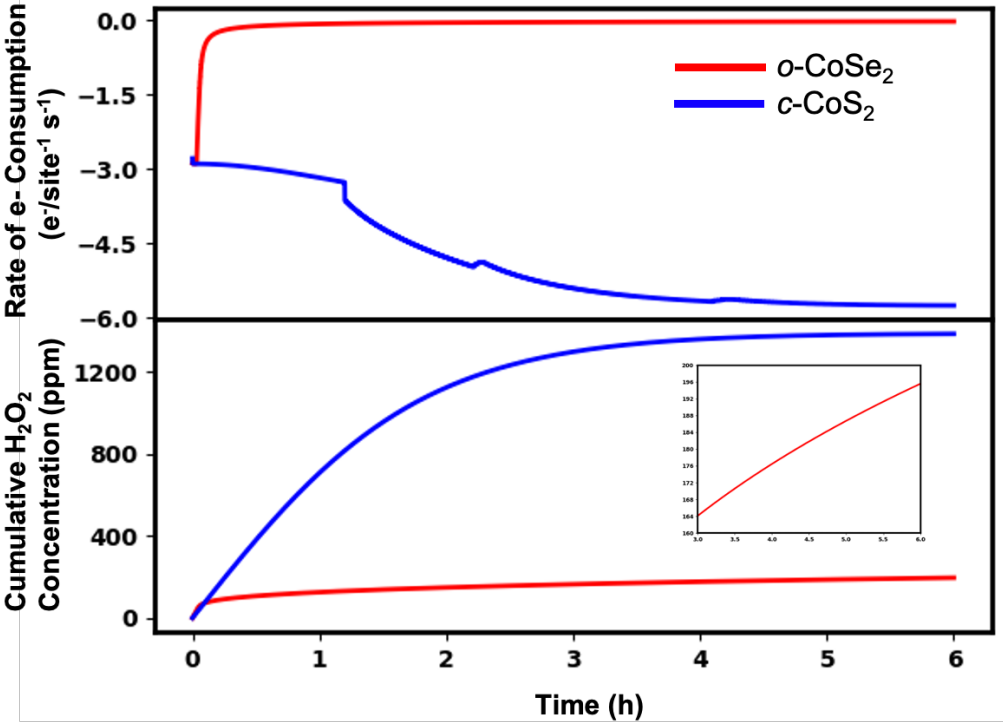

Figure 5.2: Theoretical microkinetic modeling results over time. a) Number of electrons consumed per site per second over 6 hours time. b) Accumulation of H_2O_2 in ppm over 6 hours time. Results comparable to Figure 5.1 panels a and b. Blue represents *c*-CoS_2 and red *o*-$CoSe_2$. Inset in panel b shows cumulative H_2O_2 in ppm for *o*-$CoSe_2$ from hour 3 to hour 6. While accumulation has stopped on *c*-CoS_2, the rate accumulation is still positive on *o*-$CoSe_2$.

on *o*-$CoSe_2$ decreases in a Nernstian fashion. On *c*-CoS_2, we see that it delivers a higher current than experiment and that it displays non-Nernstian behaviour, indicating further reduction of H_2O_2 which is confirmed by reaction flux through H_2O_2 reduction pathways. However, experimentally, *c*-CoS_2 initially shows Nernstian behaviour which we do not predict theoretically. More accurate physical descriptions of the beginning of the reaction, when there is no H_2O_2 in solution and thus infinite overpotential, must be added to accurately reproduce this phenomenon. We do, however, calculate the correct order of magnitude of current as seen experimentally, validating the foundation of our theoretical model.

Both catalysts can accumulate H_2O_2. *o*-$CoSe_2$ is steadily accumulating H_2O_2 and has not reached a maximum ppm of H_2O_2 at 6 hours (see Figure 5.2b). The inset shows clearly that the concentration of H_2O_2 in solution is still increasing, in agreement with the monotonic accumulation observed experimentally. In contrast, *c*-CoS_2 accumulates H_2O_2 more quickly but that the rate of accumulation approaches zero. While the microkinetic model does not predict the decrease in accumulation rate, it does predict that the accumulation rate reaches zero within 6 hours.

While the accumulation of 117 ppm of H_2O_2 on *o*-$CoSe_2$ is of the same order of magnitude as the experimental accumulation, on *c*-CoS_2, the theoretical model over predicts accumulation 6 fold and at a faster rate than on *o*-$CoSe_2$. One explanation for this discrepancy is the lack of representation of catalyst degradation. If *c*-CoS_2 degrades quickly, as seen experimentally, the number of sites should be decreasing throughout the reaction. Currently, the theoretical model has no mechanism to model catalyst degradation and will not represent any changes in the working catalyst due to degradation.

Overall, our results are in qualitative agreement with both previous experimental and theoretical investigations. Surface coverages are consistent with those predicted in surface Pourbaix diagrams. Both *c*-CoS_2 and *o*-$CoSe_2$ accumulate concentrations of $H_2O_{2(aq)}$ at the neces-

sary order of magnitude for industrial applications and within the same order of magnitude as seen experimentally. *c*-CoS_2 suffers from further reduction of H_2O_2 to H_2O, while *o*-$CoSe_2$ is highly resistant to these electrochemical side reactions, in alignment with bulk electrolysis experiments. Finally, the theoretical model can qualitatively reproduce H_2O_2 accumulation and rate of electron consumption.

We dig deeper into differences in energetics between the two models to develop transferable physical principles. Both catalysts show an ability to synthesize H_2O_2. While the DFT calculated barriers for PCET reactions are high (see Table 5.2), at a potential of 0.5 V *vs* RHE and at steady state coverage, barriers for PCET reactions necessary for H_2O_2 formation are moderate to low. The barrier of 0.66 eV on *o*-$CoSe_2$ for the first PCET reaction to form OOH* is the highest barrier on the $2e^-$ pathway on any of the three catalysts and does not limit H_2O_2 accumulation below industrial goals.

The pathway for reduction of $H_2O_{2(aq)}$ necessitates the adsorption of $H_2O_{2(aq)}$, then either thermal cleavage of $H_2O_2{}^*$ or the PCET to form $H_2O_{(l)}$ and OH^*. On *c*-CoS_2, this reaction is -0.02 eV and on *o*-$CoSe_2$ it is 0.22 eV (see Table 5.4). Only *c*-CoS_2 has cobalt sites free to adsorb H_2O_2. Both thermal cleavage of H_2O_2 and PCET reduction of H_2O_2 are very exothermic and barrierless. However, thermal cleavage requires an additional cobalt site. Finally, any OH^* accumulated must be reduced to $H_2O_{(l)}$ to complete the $4e^-$ pathway. While the DFT barrier for PCET reduction of OH^* is 0.99 eV or higher on both catalysts (see Table 5.2), we find that at steady state, this reaction on *c*-CoS_2 is barrierless while on *o*-$CoSe_2$, it has a barrier of 0.89 eV respectively (see Table 5.4). This difference in free energy barriers is due to adsorbate-adsorbate interactions with O^*. On *c*-CoS_2, the high O^* coverage increases the exothermicity of the reaction and stabilizes the transition state so significantly that the reaction becomes barrierless. On *o*-$CoSe_2$, we do not see the same accumulation of O^* due to the weaker O-Se bond and therefore do not see the lowering of the barrier. While *o*-$CoSe_2$ has a high surface

coverage of OH*,OH* has weaker interactions with other adsorbates and therefore has less effect on steady state reaction energetics. We re-calculate the microkinetic model steady state solution on *c*-CoS_2 but change the barrier of PCET reduction of OH to match the 0.89 eV barrier on *o*-$CoSe_2$. We find no flux in H_2O_2 reduction pathways and no free Co sites for H_2O_2 adsorption, indicating that the Co sites were saturated with OH* that could not be completely reduced to $H_2O_{(l)}$. We conclude that the height of the activation barrier for reduction of OH to H_2O is significantly reduced due to the high coverage of O* on *c*-CoS_2, allowing for flux through electrochemical side reactions that consume the H_2O_2 product.

5.4 Conclusion

We built two microkinetic models of $2e^-$ ORR on two different catalysts; *c*-CoS_2 and *o*-$CoSe_2$ to understand the maximum theoretical accumulation of $H_2O_{2(aq)}$ and of the catalysts are resistant to electrochemical side reactions that consume the H_2O_2 product. Our microkinetic modeling code, Micki, was modified to allow for electrochemical reactions. We found that *c*-CoS_2 can accumulate up to 40.9 mM $H_2O_{2(aq)}$ if catalyst degradation cannot occur and *o*-$CoSe_2$ can accumulate up to 9.18 mM of $H_2O_{2(aq)}$. Both of the theoretical maximum yields are the necessary order of magnitude for industrial applications and in qualitative agreement with experiment. Both catalysts showed coverages in agreement with theoretical surface Pourbaix diagrams with *c*-CoS_2 having high O* coverage and the selenide catalyst with high OH*. *c*-CoS_2 showed high flux through electrochemical side reactions that consume the H_2O_2 product while *o*-$CoSe_2$ did not. The barrier to PCET reduction of OH* to complete the $4e^-$ pathway to form water is greatly reduced by the lateral interactions with on surface O* on *c*-CoS_2. On the selenide catalyst, this barrier remains high, causing OH* to accumulate on the surface until no cobalt sites remain. Qualitative trends for electron consumption and H_2O_2 accumulation

measured through bulk electrolysis were reproduced by our microkinetic models, including the monotonic increase in H_2O_2 accumulation on *o*-$CoSe_2$ and lack of increased accumulation on *c*-CoS_2. The microkinetic models also predicted the Nernstian decrease in current over time seen on *o*-$CoSe_2$ and the non-Nernstian increase in current seen on *c*-CoS_2 and is in agreement that the shape of this curve is due to flux through H_2O_2 electrochemical reduction pathways.

While we are still far from quantitative accuracy (both because of missing complexity in the theoretical model and estimates in the experimental values of ECSA), further work can be done to increase agreement between theory and experiment and make these electrochemical microkinetic models predictive of $2e^-$ ORR behaviour. The model for PCET is a first order attempt to account for the effects of potential on reaction barriers. More sophisticated approaches should be attempted, especially as the barrier heights are important to understand flux through the reduction pathways. Attempts to represent catalyst degradation could allow for better prediction of H_2O_2 accumulation rates. However, current qualitative agreement is very encouraging that microkinetic models can offer predictive information for electrocatalysis.

In conclusion, our microkinetic modeling results are in qualitative agreement with previous theory and experiment. They show that *o*-$CoSe_2$ remains the best $2e^-$ catalyst because it can accumulate industrially relevant $H_2O_{2(aq)}$ concentrations and is resistant to further H_2O_2 reduction. High O^* coverage is responsible for the flux through electrochemical side reactions that consume the H_2O_2 product on *c*-CoS_2.

6

Conclusions and Future Directions

In summary this dissertation provided physical, molecular level insight into reactions occurring at the liquid solid interface through computational modeling. These insights provide transferable principles to apply towards rational design of new, better performing catalysts.

In Chapter 1, the microkinetic modeling code was presented. Not only does the code create an easy-to-use platform for the standard statistical mechanical formalisms and analysis tools for theoretical microkinetic modeling, it also provides novel derivations for important

physical process such as mass-transport limited adsorption, multidentate binding and a many body expansion derivation of lateral interactions. The modularity of the Micki code makes it a good building block for innumerable chemical reactions and catalyst systems. Future work on Micki could be done to build linear scaling modules to reduce the computational complexity for building a new model for a reaction network.

In Chapter 2, we utilized Micki to model the aerobic esterification of primary alcohols on promoted palladium catalysts to disentangle the mechanism of P block promoters such as tellurium. Microkinetic models were built for the unpromoted Pd(111) surface, a two-site model of a PdTe ordered alloy and a one-site model of the PdTe ordered alloy. Reactions energetics from the primary alcohol to the methyl ester, including side reactions were calculated using high level DFT. Solvation effects were treated using implicit solvent models. Our diffusion based adsorption model was used to treat solution phase adsorption. Our PdTe(111) model provided a 12.9x speedup over the unpromoted Pd(111) catalyst, but did not change the major reaction pathway. However, the mechanism for reducing O_2 did change between the models. Additionally, no reactions involving an ensemble of Te and Pd atoms was found to influence the reaction network. Based on these results, we concluded that the major effect of Te promoters is to modulate the electronic energy of the system which reduces the barrier of the rate limiting C-H bond scission and changing the pathway of O_2 reduction. Future directions can look towards understanding the role of other P block promoters, such as bismuth. As bismuth likely exists as adatoms on the palladium surface instead of as a surface alloy, the mechanistic pathway is likely very different. The current microkinetic modeling methodology can be applied directly to a Pd(111) system with Bi adatoms and compared to the model presented in this dissertation.

In Chapter 3, we investigate three cobalt dichalcogenides for performance as $2e^-$ ORR catalysts for the electrochemical synthesis of H_2O_2. Theoretically, we evaluate the catalysts based

on activity, selectivity and stability. Activity is controlled by the binding energy of OOH*, where any deviation from a binding energy of 0 eV is considered the theoretical overpotential. Selectivity is governed by the strength of the O-O bond in the OOH* intermediate. Stability is determined by the O* binding energy and surface Pourbaix diagrams. Using DFT and the computational hydrogen electrode, we calculated these energetics on *c*-CoS_2, *c*-$CoSe_2$ and *o*-$CoSe_2$. We determined that the weak binding of O* to Se as compared to S led to the increased stability of selenide catalysts over sulfide catalysts. Together with experimental collaborators, we discovered the best $2e^-$ ORR catalyst in acidic solution to date and developed transferable physical principles to screen new $2e^-$ ORR catalysts.

We applied these transferable principles to screen nickel dichalogenide catalysts in Chapter 4. We found that the *c*-$NiSe_2$ catalyst had weak binding to all species and preferentially bound O* to the nickel metal center instead of the chalocogen, predicting increased stability for *c*-$NiSe_2$. We also calculated a very low theoretical overpotential and strong O-O bond in OOH*, indicating that *c*-$NiSe_2$ could be an excellent $2e^-$ ORR catalyst and should be investigated experimentally. As *c*-$NiSe_2$ underbinds OOH* and *c*-$CoSe_2$ overbinds OOH*, the ideal catalyst should have an OOH* binding energy between the these two catalysts. One way to access this intermediate binding energy is to alloy two compounds together. We built a model of a 50-50 *c*-(Co,Ni)Se_2 alloy. Three different surface terminations of the (100) surface termination were investigated computationally. None of the surfaces gave performances better than the parent material based on our three measures of activity, selectivity and stability. We conclude that the metal centers must not have much electronic influence on neighboring metal centers and that instead alloying the dichalogen, perhaps with tellurium, would be a better alloying approach.

Future directions should focus on developing methods to incorporate important physics for electrochemistry. Current DFT methods require constant electron calculations, while the ex-

periment is done at constant potential. Recent work has been done to adapt current quantum DFT codes to perform constant potential calculations.[19] Improvements to the continuum solvent models and attempts to depict the electrochemical double layer would also add important physics into the theoretical model of the working catalyst, leading to better predictive power of the models.

In Chapter 5, we modified Micki to build electrochemical microkinetic model of two cobalt dichalcogenide catalysts investigated in Chapter 3 in order to understand maximum theoretical H_2O_2 accumulation and the flux through H_2O_2 reduction pathways that lead to loss of product. We estimated PCET barriers using a model that extrapolated barrier using Butler-Volmer kinetics. Results were compared to bulk electrolysis experiments. Qualitative agreement was found between experiment and theory for functional form of current over time and order of magnitude agreement of reaction rates. The theoretical model agreed with experiment that the non-Nernstian behaviour of the *c*-H_2O_2 was due to high flux through the H_2O_2 reduction pathways. While theory captured the monotonic increase in H_2O_2 accumulation over the 6 hours investigated and accurately predicted that the rate of accumulation of H_2O_2 on *c*-CoS_2, it incorrectly predicted that *c*-CoS_2 has a higher initial rate of H_2O_2 accumulation than *o*-$CoSe_2$. One reason for this discrepancy is the lack of pathways for catalyst degradation which *c*-CoS_2 is known to suffer from. However, the model does predict the correct order of magnitude accumulation of H_2O_2 on both catalysts. These results are encouraging that microkinetic models can be applied to electrochemical systems to provide qualitative trends and order of magnitude predictions. Future directions include utilizing the strategies described for improvements to work in Chapter 3 and Chapter 4. Additionally, better descriptions of PCET would improve the theoretical model. Also, a pathway to describe the most important effects of catalyst degradation, perhaps benchmarked to experimental leaching rates would greatly improve the prediction abilities of electrochemical microkinetic models.

Overall, in this dissertation, we developed methodologies for kinetic modeling and frameworks based on transferable physical principles to evaluate electrochemical catalyst performance. This has lead to better understanding of promoters in aerobic oxidation of primary alcohols and the discovery of the best to date $2e^-$ ORR catalyst in acidic media. These principles can be applied to evaluate other catalyst systems for similar reactions, providing directions for rational catalyst design based on physical laws.

References

[1] Abild-Pedersen, F., Greeley, J., Studt, F., Rossmeisl, J., Munter, T. R., Moses, P. G., Skúlason, E., Bligaard, T., & Nørskov, J. K. (2007). Scaling properties of adsorption energies for hydrogen-containing molecules on transition-metal surfaces. *Physical Review Letters*, 99(1), 4–7.

[2] Adkin, H. & Broderick, A. E. (1928). Hemiacetal Formation and the Refractive Indices and Densities of Mixtures of Certain Alcohols and Aldehydes. *Journal of American Chemical Society*, 50, 499–503.

[3] Alchagirov, A. B., Perdew, J. P., Boettger, J. C., Albers, R. C., & Fiolhais, C. (2001). Energy and pressure versus volume: Equations of state motivated by the stabilized jellium model. *Physical Review B - Condensed Matter and Materials Physics*, 63(22), 2241151–22411516.

[4] Anisimov, V. I., Zaanen, J., & Andersen, O. K. (1991). Band theory and Mott insulators: Hubbard U instead of Stoner I. *Physical Review B*, 44(3), 943–954.

[5] Antonin, V. S., Assumpcao, M. H., Silva, J. C., Parreira, L. S., Lanza, M. R., & Santos, M. C. (2013). Synthesis and characterization of nanostructured electrocatalystsbased on nickel and tin for hydrogen peroxide electrogeneration. *Electrochimica Acta*, 109, 245–251.

[6] Bahn, S. R. & Jacobsen, K. W. (2002). An Object-Oriented Scripting Interface to a Legacy Electronic Structure Code. *Computing in Science & Engineering*, 4(3), 56–66.

[7] Behtash, S., Lu, J., & Heyden, A. (2014). Theoretical investigation of the hydrodeoxygenation of methyl propionate over Pd (111) model surfaces. *Catal. Sci. Technol.*, 4(11), 3981–3992.

[8] Bender, T. A., Dabrowski, J. A., & Gagné, M. R. (2018). Homogeneous catalysis for the production of low-volume, high-value chemicals from biomass. *Nature Reviews Chemistry*, 2(5), 35–46.

[9] Besson, M. & Gallezot, P. (2000). Selective oxidation of alcohols and aldehydes on metal catalysts. *Catalysis Today*, 57(1-2), 127–141.

[10] Blöchl, P. E. (1994). Projector augmented-wave method. *Physical Review B*, 50(24), 17953–17979.

[11] Boudart, M. (1985). Heterogeneous catalysis by metals. *Journal of Molecular Catalysis*, 30(1-2), 27–38.

[12] Brillas, E. & Garcia-Segura, S. (2020). Benchmarking recent advances and innovative technology approaches of Fenton, photo-Fenton, electro-Fenton, and related processes: A review on the relevance of phenol as model molecule. *Separation and Purification Technology*, 237(November 2019), 116337.

[13] Brillas, E., Sirés, I., & Oturan, M. A. (2009). Electro-fenton process and related electrochemical technologies based on fenton's reaction chemistry. *Chemical Reviews*, 109(12), 6570–6631.

[14] Bronsted, J. N. (1928). Acid and Basic Catalysis. *Chemical Reviews*, 5(3), 213–227.

[15] Campbell, C. T. (1994). Future Directions and Industrial Perspectives Micro- and macro-kinetics: Their relationship in heterogeneous catalysis. *Topics in Catalysis*, 1(3-4), 353–366.

[16] Campbell, C. T. (2017). The degree of rate control: a powerful tool for catalysis research. *ACS Catalysis*, 7, 2770–2779.

[17] Campos-Martin, J. M., Blanco-Brieva, G., & Fierro, J. L. (2006). Hydrogen peroxide synthesis: An outlook beyond the anthraquinone process. *Angewandte Chemie - International Edition*, 45(42), 6962–6984.

[18] Chattopadhyay, G., Bhatt, J., & Khera, S. K. (1986). Phase Diagram of the Pd-Te System. *Journal of the Less-Common Metals*, 123, 251–266.

[19] Chen, M. F., Chao, T. H., Shen, M. H., Lu, Q., & Cheng, M. J. (2020). Evaluating Potential Catalytic Active Sites on Nitrogen-Doped Graphene for the Oxygen Reduction Reaction: An Approach Based on Constant Electrode Potential Density Functional Theory Calculations. *Journal of Physical Chemistry C*.

[20] Chen, Z., Mao, Y., Chen, J., Wang, H., Li, Y., & Hu, P. (2017). Understanding the Dual Active Sites of the FeO / Pt (111) Interface and Reaction Kinetics : Density Functional Theory Study on Methanol Oxidation to Formaldehyde. *ACS Catalysis*, 7(111), 4281–4290.

[21] Choi, C. H., Kim, M., Kwon, H. C., Cho, S. J., Yun, S., Kim, H. T., Mayrhofer, K. J., Kim, H., & Choi, M. (2016). Tuning selectivity of electrochemical reactions by atomically dispersed platinum catalyst. *Nature Communications*, 7, 1–9.

[22] Chu, S., Cui, Y., & Liu, N. (2016). The path towards sustainable energy. *Nature Materials*, 16(1), 16–22.

[23] Ciriminna, R., Albanese, L., Meneguzzo, F., & Pagliaro, M. (2016). Hydrogen Peroxide: A Key Chemical for Today's Sustainable Development. *ChemSusChem*, 9(24), 3374–3381.

[24] Cole-Hamilton, D. J. (2003). Homogeneous catalysis - New approaches to catalyst separation, recovery, and recycling. *Science*, 299(5613), 1702–1706.

[25] DiCosimo, R. & Whitesides, G. M. (1989). Oxidation of 2-Propanol to Acetone by Dioxygen on Platinized Electrode under. *Journal of Physical Chemistry*, 93, 768–775.

[26] Dijkgraaf, P. (1989). *Oxidation of Glucose to Glucaric Acid by Pt/C Catalysts*. Ph.d. thesis, Technische Universiteit Eindhoven.

[27] Dumesic, J. A., Rudd, D. F., Aparicio, L. M., Rekoske, J. E., & Trevino, A. A. (1993). *The Microkinetics of Heterogeneous Catalysis*. Salem, MA: American Chemical Society.

[28] Dunning, T. H. (1989). Gaussian basis sets for use in correlated molecular calculations. I. The atoms boron through neon and hydrogen. *The Journal of Chemical Physics*, 90(2), 1007–1023.

[29] Edwards, J. K., Freakley, S. J., Lewis, R. J., Pritchard, J. C., & Hutchings, G. J. (2015). Advances in the direct synthesis of hydrogen peroxide from hydrogen and oxygen. *Catalysis Today*, 248, 3–9.

[30] Evans, M. G. & Polanyi, M. (1936). Equilibrium Constants and Velocity Constants. *Nature*, 130, 530–531.

[31] Fang, Y. H. & Liu, Z. P. (2010). Mechanism and tafel lines of electro-oxidation of water to oxygen on RuO2(110). *Journal of the American Chemical Society*, 132(51), 18214–18222.

[32] Ferri, D., Mondelli, C., Krumeich, F., & Baiker, A. (2006). Discrimination of active palladium sites in catalytic liquid-phase oxidation of benzyl alcohol. *Journal of Physical Chemistry B*, 110(46), 22982–22986.

[33] Fiege, H. & Wedemeyer, K. (1981). Activation of Oxidations with Oxygen on Metallic Platinum as an Example of the Conversion of 2-Phyeboxyethanols to Phenoxyacetic Acids. *Angewandte Chemie - International Edition*, 12(51), 783–784.

[34] Ford, D. C., Nilekar, A. U., Xu, Y., & Mavrikakis, M. (2010). Partial and complete reduction of O2 by hydrogen on transition metal surfaces. *Surface Science*, 604(19-20), 1565–1575.

[35] Freakley, S. J., He, Q., Harrhy, J. H., Lu, L., Crole, D. A., Morgan, D. J., Ntainjua, E. N., Edwards, J. K., Carley, A. F., Borisevich, A. Y., Kiely, C. J., & Hutchings, G. J. (2016). Palladium-tin catalysts for the direct synthesis ofH2O2 with high selectivity. *Science*, 351(6276), 965–968.

[36] Friend, C. M. & Xu, B. (2017). Heterogeneous catalysis: A central science for a sustainable future. *Accounts of Chemical Research*, 50(3), 517–521.

[37] Frisch, M., Trucks, G., Schlegel, H. B., Scuseria, G. E., Robb, M. A., Cheeseman, J. R., Scalmani, G., Barone, V., Mennucci, B., Petersson, G. A., Nakatsuji, H., Caricato, M., Li, X., Hratchian, H. P., Izmaylov, A. F., Bloino, J., Zheng, G., Sonnenberg, J. L., Had, M., & Fox, D. J. (2009). Gaussian 09 Revision D.01.

[38] Furuseth, S., Kjekshus, A., Andresen, A. F., Nordal, V., Lindberg, A. A., & Craig, J. C. (1969). On the Magnetic Properties of CoSe2, NiS2, and NiSe2. *Acta Chemica Scandinavica*, 23, 2325–2334.

[39] Gale, W. & Totemeir, T. (2004). *Smithells Metals Reference Book*. Burlington, MA: Elsevier Science, 8 edition.

[40] Gao, C. W., Allen, J. W., Green, W. H., & West, R. H. (2016). Reaction Mechanism Generator: Automatic construction of chemical kinetic mechanisms. *Computer Physics Communications*, 203, 212–225.

[41] Gao, J., bin Yang, H., Huang, X., Hung, S. F., Cai, W., Jia, C., Miao, S., Chen, H. M., Yang, X., Huang, Y., Zhang, T., & Liu, B. (2020). Enabling Direct H_2O_2 Production in Acidic Media through Rational Design of Transition Metal Single Atom Catalyst. *Chem*, 6(3), 658–674.

[42] Gil, A., Clotet, A., Ricart, J. M., Kresse, G., García-Hernández, M., Rösch, N., & Sautet, P. (2003). Site preference of CO chemisorbed on Pt(1 1 1) from density functional calculations. *Surface Science*, 530(1-2), 71–87.

[43] Gokhale, A. A., Kandoi, S., Greeley, J. P., Mavrikakis, M., & Dumesic, J. A. (2004). Molecular-level descriptions of surface chemistry in kinetic models using density functional theory. *Chemical Engineering Science*, 59(22-23), 4679–4691.

[44] Goodwin, D. G., Speth, R. L., Moffat, H. K., & Weber, B. W. (2018). Cantera: An Object-oriented Software Toolkit for Chemical Kinetics, Thermodynamics, and Transport Processes.

[45] Gossé, S. & Guéneau, C. (2011). Thermodynamic assessment of the palladium-tellurium (Pd-Te) system. *Intermetallics*, 19(5), 621–629.

[46] Grabow, L. C., Gokhale, A. A., Evans, S. T., Dumesic, J. A., & Mavrikakis, M. (2008). Mechanism of the water gas shift reaction on Pt: First principles, experiments, and microkinetic modeling. *Journal of Physical Chemistry C*, 112(12), 4608–4617.

[47] Greeley, J., Jaramillo, T. F., Bonde, J., Chorkendorff, I. B., & Nørskov, J. K. (2006a). Computational high-throughput screening of electrocatalytic materials for hydrogen evolution. *Nature materials*, 5(11), 909–13.

[48] Greeley, J., Nørskov, J. K., Kibler, L. A., El-Aziz, A. M., & Kolb, D. M. (2006b). Hydrogen evolution over bimetallic systems: Understanding the trends. *ChemPhysChem*, 7(5), 1032–1035.

[49] Grimme, S., Antony, J., Ehrlich, S., & Krieg, H. (2010). A consistent and accurate ab initio parametrization of density functional dispersion correction (DFT-D) for the 94 elements H-Pu. *Journal of Chemical Physics*, 132(15).

[50] Grimme, S., Ehrlich, S., & Goerigk, L. (2011). Effect of the Damping Function in Dispersion Corrected Density Functional Theory. *Journal of Computational Chemistry*, 32, 1456–1465.

[51] Gu, W., Hu, L., Hong, W., Jia, X., Li, J., & Wang, E. (2016). Noble-metal-free Co₃S₄–S/G porous hybrids as an efficient electrocatalyst for oxygen reduction reaction†. *Chem. Sci.*, 7(7), 4167–4173.

[52] Hansen, H. A., Rossmeisl, J., & Nørskov, J. K. (2008). Surface Pourbaix diagrams and oxygen reduction activity of Pt, Ag and Ni(111) surfaces studied by DFT. *Physical Chemistry Chemical Physics*, 10, 3722–3730.

[53] Haraldsen, H., Møllerud, R., Røst, E., Cyvin, S. J., & Hagen, G. (1967). On the System Co-Ni-Se. *Acta Chemica Scandinavica*, 21, 1727–1736.

[54] Hasché, F., Oezaslan, M., Strasser, P., & Fellinger, T. P. (2016). Electrocatalytic hydrogen peroxide formation on mesoporous non-metal nitrogen-doped carbon catalyst. *Journal of Energy Chemistry*, 25(2), 251–257.

[55] Hayashi, H., Sugiyama, S., Shigemoto, N., Miyaura, K., Tsujino, S., Kawashiro, K., & Uemura, S. (1993). Formation of an intermetallic compound Pd_3Te with deactivation of Te/Pd/C catalysts for selective oxidation of sodium lactate to pyruvate in aqueous phase. *Catalysis Letters*, 19(4), 369–373.

[56] Henkelman, G., Jóhannesson, G., & Jónsson, H. (2002). Theoretical methods in condensed phase chemistry. *Theoretical Methods in Condensed Phase Chemistry - Progress in Theoretical Chemistry and Physics - Volume 5*, 5, 269–302.

[57] Henkelman, G. & Jónsson, H. (1999). A Dimer Method for Finding Saddle Points on High Dimensional Potential Surfaces using only First Derivatives. *J. Chem. Phys.*, 111(15), 7010–7022.

[58] Henkelman, G., Uberuaga, B. P., & Jónsson, H. (2000). A Climbing Image Nudged Elastic Band Method for Finding Saddle Points and Minimum Energy Paths. *J. Chem. Phys.*, 113(22), 9901.

[59] Hermes, E. D. (2018). *Realistic Models For Theoretical Studies of Heterogeneous Catalysis*. PhD thesis, University of Wisconsin Madison.

[60] Hermes, E. D., Janes, A. N., & Schmidt, J. R. (2018). Mechanistic Insights into Solution-Phase Oxidative Esterification of Primary Alcohols on Pd(111) from First-Principles Microkinetic Modeling. *ACS Catalysis*, 8(1), 272–282.

[61] Hermes, E. D., Janes, A. N., & Schmidt, J. R. (2019). Micki: A python-based object-oriented microkinetic modeling code. *The Journal of Chemical Physics*, 151(1), 014112.

[62] Heyd, J., Peralta, J. E., Scuseria, G. E., & Martin, R. L. (2005). Energy band gaps and lattice parameters evaluated with the Heyd-Scuseria-Ernzerhof screened hybrid functional. *Journal of Chemical Physics*, 123(17).

[63] Heyd, J. & Scuseria, G. E. (2004). Assessment and validation of a screened Coulomb hybrid density functional. *Journal of Chemical Physics*, 120(16), 7274–7280.

[64] Heyden, A., Bell, A. T., & Keil, F. J. (2005). Efficient methods for finding transition states in chemical reactions: Comparison of improved dimer method and partitioned rational function optimization method. *Journal of Chemical Physics*, 123(22).

[65] Hindmarsh, A. C., Brown, P. N., Grant, K. E., Lee, S. L., Serban, R., Shumaker, D. E., & Woodward, C. S. (2005). SUNDIALS: Suite of nonlinear and differential/algebraic equation solvers. *ACM Transactions on Mathematical Software (TOMS)*, 31(3), 363–396.

[66] Hoffman, A. & Kuhn, A. T. (1964). Open Circuit Reduction of Chemisorbed Oxygen and Platinum. *Electrochimica Acta*, 9, 835–839.

[67] Iglesias, D., Giuliani, A., Melchionna, M., Marchesan, S., Criado, A., Nasi, L., Bevilacqua, M., Tavagnacco, C., Vizza, F., Prato, M., & Fornasiero, P. (2018). N-Doped Graphitized Carbon Nanohorns as a Forefront Electrocatalyst in Highly Selective O_2 Reduction to H_2O_2. *Chem*, 4(1), 106–123.

[68] Izmaylov, A. F., Scuseria, G. E., & Frisch, M. J. (2006). Efficient evaluation of short-range Hartree-Fock exchange in large molecules and periodic systems. *Journal of Chemical Physics*, 125(10).

[69] Jain, A., Ong, S. P., Hautier, G., Chen, W., Richards, W. D., Dacek, S., Cholia, S., Gunter, D., Skinner, D., Ceder, G., & Persson, K. A. (2013). Commentary: The materials project: A materials genome approach to accelerating materials innovation. *APL Materials*, 1(1).

[70] Jenkins, S. J. & King, D. A. (2000). A Role for Induced Molecular Polarization in Catalytic Promotion : CO Coadsorbed with K on Co{101h0}. *Journal of American Chemical Society*, 122, 10610–10614.

[71] Jiang, H., He, Q., Zhang, Y., & Song, L. (2018). Structural Self-Reconstruction of Catalysts in Electrocatalysis. *Accounts of Chemical Research*, 51(11), 2968–2977.

[72] Jiang, K., Back, S., Akey, A. J., Xia, C., Hu, Y., Liang, W., Schaak, D., Stavitski, E., Nørskov, J. K., Siahrostami, S., & Wang, H. (2019). Highly selective oxygen reduction to hydrogen peroxide on transition metal single atom coordination. *Nature Communications*, 10(1).

[73] Jones, E., Oliphant, T., & Peterson, P. (2001). SciPy: Open source scientific tools for Python.

[74] Jung, E., Shin, H., Lee, B. H., Efremov, V., Lee, S., Lee, H. S., Kim, J., Hooch Antink, W., Park, S., Lee, K. S., Cho, S. P., Yoo, J. S., Sung, Y. E., & Hyeon, T. (2020). Atomic-level tuning of Co–N–C catalyst for high-performance electrochemical H2O2 production. *Nature Materials*, 19(4), 436–442.

[75] Kamyabi, M. A., Soleymani-Bonoti, F., Alirezaei, F., Bikas, R., Noshiranzadeh, N., Emami, M., Krawczyk, M. S., & Lis, T. (2019). Electrocatalytic properties of a dinuclear cobalt(III) coordination compound in molecular oxygen reduction reaction. *Applied Organometallic Chemistry*, 33(12), 1–11.

[76] Kandoi, S., Greeley, J., Sanchez-Castillo, M. A., Evans, S. T., Gokhale, A. A., Dumesic, J. A., & Mavrikakis, M. (2006). Prediction of experimental methanol decomposition rates on platinum from first principles. *Topics in Catalysis*, 37(1), 17–27.

[77] Kästner, J. & Sherwood, P. (2008). Superlinearly converging dimer method for transition state search. *Journal of Chemical Physics*, 128(1).

[78] Keith, J. A. & Jacob, T. (2010). Theoretical studies of potential-dependent and competing mechanisms of the electrocatalytic oxygen reduction reaction on Pt(111). *Angewandte Chemie - International Edition*, 49(49), 9521–9525.

[79] Kibsgaard, J., Gorlin, Y., Chen, Z., & Jaramillo, T. F. (2012). Meso-structured platinum thin films: Active and stable electrocatalysts for the oxygen reduction reaction. *Journal of the American Chemical Society*, 134(18), 7758–7765.

[80] Kim, H. W., Ross, M. B., Kornienko, N., Zhang, L., Guo, J., Yang, P., & McCloskey, B. D. (2018). Efficient hydrogen peroxide generation using reduced graphene oxide-based oxygen reduction electrocatalysts. *Nature Catalysis*, 1(4), 282–290.

[81] Kimura, H., Tsuto, K., Wakisaka, T., Kazumi, Y., & Inaya, Y. (1993). Selective oxidation of glycerol on a platinum-bismuth catalyst by using a fixed bed reactor. *Applied Catalysis A, General*, 105(2), 147–158.

[82] Kohn, W. (1999). Nobel lecture: Electronic structure of matter - Wave functions and density functional. *Reviews of Modern Physics*, 71(5), 1253–1266.

[83] Kresse, G. & Furthmüller, J. (1996a). Efficiency of ab-initio total energy calculations for metals and semiconductors using a plane-wave basis set. *Computational Materials Science*, 6(1), 15–50.

[84] Kresse, G. & Furthmüller, J. (1996b). Efficient iterative schemes for ab initio total-energy calculations using a plane-wave basis set. *Physical Review B - Condensed Matter and Materials Physics*, 54(16), 11169–11186.

[85] Kresse, G. & Hafner, J. (1993). Ab initio molecular dynamics for liquid metals. *Physical Review B*, 47(1), 558–561.

[86] Kresse, G. & Hafner, J. (1994). Ab initio molecular-dynamics simulation of the liquid-metal–amorphous-semiconductor transition in germanium. *Physical Review B*, 49(20), 14251–14269.

[87] Kresse, G. & Joubert, D. (1999). From ultrasoft pseudopotentials to the projector augmented-wave method. *Physical Review B*, 59(3), 1758–1775.

[88] Kulkarni, A., Siahrostami, S., Patel, A., & Nørskov, J. K. (2018). Understanding Catalytic Activity Trends in the Oxygen Reduction Reaction. *Chemical Reviews*, 118(5), 2302–2312.

[89] Kuznetsova, N. I., Zudin, V. N., Kuznetsova, L. I., Zaikovskii, V. I., Kajitani, H., Utsunomiya, M., & Takahashi, K. (2016). Versatile PdTe/C catalyst for liquid-phase oxidations of 1,3-butadiene. *Applied Catalysis A: General*, 513, 30–38.

[90] Larsen, A. H., Mortensen, J. J., Blomqvist, J., Castelli, I. E., Christensen, R., Dułak, M., Friis, J., Groves, M. N., Hammer, B., Hargus, C., Hermes, E. D., Jennings, P. C., Jensen, P. B., Kermode, J., Kitchin, J. R., Kolsbjerg, E. L., Kubal, J., Kaasbjerg, K., Lysgaard, S., Maronsson, J. B., Maxson, T., Olsen, T., Pastewka, L., Peterson, A., Rostgaard, C., Schiøtz, J., Schütt, O., Strange, M., Thygesen, K. S., Vegge, T., Vilhelmsen, L., Walter, M., Zeng, Z., & Jacobsen, K. W. (2017). The Atomic Simulation Environment — A Python library for working with atoms. *Journal of Physics: Condensed Matter*, 29(March), 273002.

[91] Lauder, I. (1948). Studies on Hemiacetal Formation: Part I.–The System Acetaldeyde-Water. *Transactions of the Faraday Society*, 44, 729–735.

[92] Li, L., Tang, C., Zheng, Y., Xia, B., Zhou, X., Xu, H., & Qiao, S. Z. (2020). Tailoring Selectivity of Electrochemical Hydrogen Peroxide Generation by Tunable Pyrrolic-Nitrogen-Carbon. *Advanced Energy Materials*, 10(21), 1–10.

[93] Li, W., Walther, C. F., Kuc, A., & Heine, T. (2013). Density functional theory and beyond for band-gap screening: Performance for transition-metal oxides and dichalcogenides. *Journal of Chemical Theory and Computation*, 9(7), 2950–2958.

[94] Liang, Y., Li, Y., Wang, H., & Dai, H. (2013). Strongly coupled inorganic/nanocarbon hybrid materials for advanced electrocatalysis. *Journal of the American Chemical Society*, 135(6), 2013–2036.

[95] Logadottir, A., Rod, T. H., Nørskov, J. K., Hammer, B., Dahl, S., & Jacobsen, C. J. (2001). The Brønsted-Evans-Polanyi relation and the volcano plot for ammonia synthesis over transition metal catalysts. *Journal of Catalysis*, 197(2), 229–231.

[96] Lu, Z., Chen, G., Siahrostami, S., Chen, Z., Liu, K., Xie, J., Liao, L., Wu, T., Lin, D., Liu, Y., Jaramillo, T. F., Nørskov, J. K., & Cui, Y. (2018). High-efficiency oxygen reduction to hydrogen peroxide catalysed by oxidized carbon materials. *Nature Catalysis*, 1(2), 156–162.

[97] M. G. Evans & M. Polanyi (1936). Dynamics of Chemical Equilibria and. *Transactions of the Faraday Society*, 32, 1333–1360.

[98] Ma, F., Wang, S., Liang, X., Wang, C., Tong, F., Wang, Z., Wang, P., Liu, Y., Dai, Y., Zheng, Z., & Huang, B. (2020). Ni_3B as a highly efficient and selective catalyst for the electrosynthesis of hydrogen peroxide. *Applied Catalysis B: Environmental*, 279(July).

[99] Mallat, T. & Baiker, A. (2004). Oxidation of alcohols with molecular oxygen on solid catalysts. *Chemical Reviews*, 104(6), 3037–3058.

[100] Mallat, T., Bodnar, Z., & Baiker, A. (1993a). Partial oxidation of water—insoluble alcohols over Bi—promoted Pt on alumina. Electrochemical characterization of the catalyst in its working state. *Studies in Surface Science and Catalysis*, 78(C), 377–384.

[101] Mallat, T., Bodnar, Z., & Baiker, A. (1993b). Promotion and deactivation of platinum catalysts in liquid-phase oxidation of secondary alcohols. *ACS Symp. Ser.*, 523, 308–317.

[102] Mallat, T., Bodnar, Z., Hug, P., & Baiker, A. (1995). Selective Oxidation of Cinnamly Alcohol to Cinnamaldehyde with Air over Bi-Pt/Alumina Catalysts. *Journal of Catalysis*, 153, 131–143.

[103] Mannel, D. S. (2015). *Noble Metal Heterogeneous Catalysts for Aerobic Alcohol Oxidation : Discovery and Mechanism By*. PhD thesis, University of Wisconsin Madison.

[104] Mannel, D. S., Ahmed, M. S., Root, T. W., & Stahl, S. S. (2017). Discovery of Multicomponent Heterogeneous Catalysts via Admixture Screening: PdBiTe Catalysts for Aerobic Oxidative Esterification of Primary Alcohols. *Journal of The American Chemical Society*.

[105] Marenich, A. V., Cramer, C. J., & Truhlar, D. G. (2009). Universal solvation model based on solute electron density and on a continuum model of the solvent defined by the bulk dielectric constant and atomic surface tensions. *Journal of Physical Chemistry B*, 113(18), 6378–6396.

[106] Mathew, K. & Hennig, R. G. (2016). Implicit self-consistent description of electrolyte in plane-wave density-functional theory. *Arxiv preprint*, (pp. 1–6).

[107] Mathew, K., Sundararaman, R., Letchworth-Weaver, K., Arias, T. A., & Hennig, R. G. (2014a). Implicit solvation model for density-functional study of nanocrystal surfaces and reaction pathways. *Journal of Chemical Physics*, 140(8).

[108] Mathew, K., Sundararaman, R., Letchworth-Weaver, K., Arias, T. A., & Hennig, R. G. (2014b). Implicit solvation model for density-functional study of nanocrystal surfaces and reaction pathways. *J. Chem. Phys.*, 140, 84106.

[109] McCrory, C. C., Jung, S., Peters, J. C., & Jaramillo, T. F. (2013). Benchmarking heterogeneous electrocatalysts for the oxygen evolution reaction. *Journal of the American Chemical Society*, 135(45), 16977–16987.

[110] Mckenna, F. E., Tartar, H. V., & Lingafelter, E. C. (1953). Studies of Hemiacetal Formation in Alcohol-Aldehyde Systems. II. Refraction Studies. *Journal of American Chemical Society*, 75, 604–607.

[111] McQuarrie, D. A. (1976). *Statistical Mechanics*. New York, NY: Harper Collins.

[112] Medford, A. J., Shi, C., Hoffmann, M. J., Lausche, A. C., Fitzgibbon, S. R., Bligaard, T., & Nørskov, J. K. (2015). CatMAP: A Software Package for Descriptor-Based Microkinetic Mapping of Catalytic Trends. *Catalysis Letters*, 145(3), 794–807.

[113] Methfessel, M. & Paxton, A. T. (1989). High-precision sampling for Brillouin-zone integration in metals. *Physical Review B*, 40(6), 3616–3621.

[114] Meurer, A., Smith, C. P., Paprocki, M., Čertík, O., Kirpichev, S. B., Rocklin, M., Kumar, A., Ivanov, S., Moore, J. K., Singh, S., Rathnayake, T., Vig, S., Granger, B. E., Muller, R. P., Bonazzi, F., Gupta, H., Vats, S., Johansson, F., Pedregosa, F., Curry,

M. J., Terrel, A. R., Roučka, Š., Saboo, A., Fernando, I., Kulal, S., Cimrman, R., & Scopatz, A. (2017). SymPy: symbolic computing in Python. *PeerJ Computer Science*, 3, e103.

[115] Michaelides, A., Liu, Z. P., Zhang, C. J., Alavi, A., King, D. A., & Hu, P. (2003). Identification of general linear relationships between activation energies and enthalpy changes for dissociation reactions at surfaces. *Journal of the American Chemical Society*, 125(13), 3704–3705.

[116] Moellmann, J. & Grimme, S. (2014). DFT-D3 study of some molecular crystals. *Journal of Physical Chemistry C*, 118(14), 7615–7621.

[117] Mondelli, C., Ferri, D., Grunwaldt, J. D., Krumeich, F., Mangold, S., Psaro, R., & Baiker, A. (2007). Combined liquid-phase ATR-IR and XAS study of the Bi-promotion in the aerobic oxidation of benzyl alcohol over Pd/Al_2O_3. *Journal of Catalysis*, 252(1), 77–87.

[118] Mondelli, C., Grunwaldt, J.-D., Ferri, D., & Baiker, A. (2010). Role of Bi promotion and solvent in platinum-catalyzed alcohol oxidation probed by in situ X-ray absorption and ATR-IR spectroscopy. *Physical Chemistry Chemical Physics*, 12, 5307–5316.

[119] Murray, A. T., Voskian, S., Schreier, M., Hatton, T. A., & Surendranath, Y. (2019). Electrosynthesis of Hydrogen Peroxide by Phase-Transfer Catalysis. *Joule*, 3(12), 2942–2954.

[120] Nguyen-Cong, H., De la Garza Guadarrama, V., Gautier, J. L., & Chartier, P. (2003). Oxygen reduction on $Ni_xCo_{3-x}O_4$ spinel particles/polypyrrole composite electrodes: Hydrogen peroxide formation. *Electrochimica Acta*, 48(17), 2389–2395.

[121] Nie, X., Luo, W., Janik, M. J., & Asthagiri, A. (2014). Reaction mechanisms of CO_2 electrochemical reduction on Cu(1 1 1) determined with density functional theory. *Journal of Catalysis*, 312, 108–122.

[122] NIST (2018). NIST Chemistry Webbook.

[123] Nitzan, A. (2006). *Chemical Dynamics in Condensed Phases*. New York, NY: Oxford University Press.

[124] Nørskov, J. K., Abild-Pedersen, F., Studt, F., & Bligaard, T. (2011). Density functional theory in surface chemistry and catalysis. *Proceedings of the National Academy of Sciences of the United States of America*, 108(3), 937–943.

[125] Nørskov, J. K., Bligaard, T., Rossmeisl, J., & Christensen, C. H. (2009). Towards the computational design of solid catalysts. *Nature chemistry*, 1(1), 37–46.

[126] Nørskov, J. K., Rossmeisl, J., Logadottir, A., Lindqvist, L., Kitchin, J. R., Bligaard, T., & Jónsson, H. (2004a). Origin of the overpotential for oxygen reduction at a fuel-cell cathode. *Journal of Physical Chemistry B*, 108(46), 17886–17892.

[127] Nørskov, J. K., Rossmeisl, J., Logadottir, A., Lindqvist, L., Lyngby, D., & Jo, H. (2004b). Origin of the Overpotential for Oxygen Reduction at a Fuel-Cell Cathode. (pp. 17886–17892).

[128] Okamoto, H. (1994). The Bi-Pd (Bismuth-Palladium) System. *Journal of Phase Equilibria*, 15(2), 191–194.

[129] Oliphant, T. E. (2006). *A guide to NumPy*. Trelgol Publishing USA, 1 edition.

[130] Onoda, T., Yamura, A., Ohno, A., Haji, J., Toriya, J., Sata, M., & Ishizaki, N. (1974). Process for Preparing an Unsaturated Ester.

[131] Pack, J. D. & Monkhorst, H. J. (1976). Special points for Brillouin-zone integrations. *Physical Review B*, 16(4), 1748–1749.

[132] Pal, D. B., Chand, R., Upadhyay, S. N., & Mishra, P. K. (2018). Performance of water gas shift reaction catalysts: A review. *Renewable and Sustainable Energy Reviews*, 93(June), 549–565.

[133] Parmegianni, C. & Cardona, F. (2012). Transition Metal Catalysis in Aerobic Alcohol Oxidation. *Green Chemistry*, 14, 547.

[134] Parsons, R. & Vandernoot, T. (1988). The oxidation of small organic molecules A survey of recent fuel cell related research. *J. Electroanal. Chem*, 257, 9–45.

[135] Perdew, J. P., Burke, K., & Ernzerhof, M. (1996). Generalized Gradient Approximation Made Simple. *Physical Review Letters*, 77(18), 3865–3868.

[136] Perdew, J. P., Burke, K., & Ernzerhof, M. (1997). Generalized Gradient Approximation Made Simple. *Physical Review Letters*, 78(7), 1396.

[137] Perry, S. C., ki Leung, P., Wang, L., & Ponce de León, C. (2020). Developments on carbon dioxide reduction: Their promise, achievements, and challenges. *Current Opinion in Electrochemistry*, 20, 88–98.

[138] Pizzutilo, E., Kasian, O., Choi, C. H., Cherevko, S., Hutchings, G. J., Mayrhofer, K. J., & Freakley, S. J. (2017). Electrocatalytic synthesis of hydrogen peroxide on Au-Pd nanoparticles: From fundamentals to continuous production. *Chemical Physics Letters*, 683, 436–442.

[139] Popovic, K. D., Markovic, N. M., Tripkovic, A. V., & Adtic, R. R. (1991). Structural effects in electrocatalysis Oxidation of D-glucose on single crystal platinum electrodes in alkaline solution. *J. Electroanal. Chem*, 313, 181–199.

[140] Powell, A. B. & Stahl, S. S. (2013). Aerobic oxidation of diverse primary alcohols to methyl esters with a readily accessible heterogeneous Pd/Bi/Te catalyst. *Organic Letters*, 15(19), 5072–5075.

[141] Qiang, Z., Chang, J. H., & Huang, C. P. (2002). Electrochemical generation of hydrogen peroxide from dissolved oxygen in acidic solutions. *Water Research*, 36(1), 85–94.

[142] Reaction Design (2013). CHEMKIN 10131.

[143] Reis, R. M., Valim, R. B., Rocha, R. S., Lima, A. S., Castro, P. S., Bertotti, M., & Lanza, M. R. (2014). The use of copper and cobalt phthalocyanines as electrocatalysts for the oxygen reduction reaction in acid medium. *Electrochimica Acta*, 139, 1–6.

[144] Ressler, T., Kniep, B. L., Kasatkin, I., & Schlögl, R. (2005). The microstructure of copper zinc oxide catalysts: Bridging the materials gap. *Angewandte Chemie - International Edition*, 44(30), 4704–4707.

[145] Ridruejo, C., Alcaide, F., Álvarez, G., Brillas, E., & Sirés, I. (2018). On-site H_2O_2 electrogeneration at a CoS_2-based air-diffusion cathode for the electrochemical degradation of organic pollutants. *Journal of Electroanalytical Chemistry*, 808(September 2017), 364–371.

[146] Santen, R. A. V., Neurock, M., & Shetty, S. G. (2010). Reactivity theory of transition-metal surfaces: A brønsted-evans- polanyi linear activation energy-free-energy analysis. *Chemical Reviews*, 110(4), 2005–2048.

[147] Santos, E., Lundin, A., Pötting, K., Quaino, P., & Schmickler, W. (2009). Model for the electrocatalysis of hydrogen evolution. *Physical Review B - Condensed Matter and Materials Physics*, 79(23), 1–10.

[148] Sathiskumar, C., Alex, C., & John, N. S. (2020). Nickel Cobalt Phosphite Nanorods Decorated with Carbon Nanotubes as Bifunctional Electrocatalysts in Alkaline Medium with a High Yield of Hydrogen Peroxide. *ChemElectroChem*, 11, 1935–1942.

[149] Schlexer, P. (2017). Computational Modeling in Heterogeneous Catalysis. In *Reference Module in Chemistry, Molecular Sciences and Chemical Engineering* (pp. 0–7).

[150] Schlögl, R. (2003). Catalytic synthesis of ammonia - A "never-ending story"? *Angewandte Chemie - International Edition*, 42(18), 2004–2008.

[151] Schuurman, Y., Kuster, B. F. M., Wiele, K. V. D., & Marin, G. B. (1992). Selective oxidation of methyl a-D-glucoside on carbon supported platinum III . Catalyst deactivation. *Applied Catalysis A, General*, 89, 47–68.

[152] Seh, Z. W., Kibsgaard, J., Dickens, C. F., Chorkendorff, I., Nørskov, J. K., & Jaramillo, T. F. (2017). Combining theory and experiment in electrocatalysis: Insights into materials design. *Science*, 355(6321).

[153] Shekhar, R. & Barteau, M. (1997). Adsorption and reaction of aldehydes on Pd surfaces. *The Journal of Physical Chemistry B*, 5647(97), 7939–7951.

[154] Sheldon, R., Arends, I., & Dijksman, A. (2000). New developments in catalytic alcohol oxidations for fine chemicals synthesis. *Catalysis Today*, 57(1-2), 157–166.

[155] Sheldon, R. A. (2015). Recent advances in green catalytic oxidations of alcohols in aqueous media. *Catalysis Today*, 247, 4–13.

[156] Shen, R., Chen, W., Peng, Q., Lu, S., Zheng, L., Cao, X., Wang, Y., Zhu, W., Zhang, J., Zhuang, Z., Chen, C., Wang, D., & Li, Y. (2019). High-Concentration Single Atomic Pt Sites on Hollow CuS_x for Selective O_2 Reduction to H_2O_2 in Acid Solution. *Chem*, (pp. 1–12).

[157] Sheng, H., Hermes, E. D., Yang, X., Ying, D., Janes, A. N., Li, W., Schmidt, J. R., & Jin, S. (2019). Electrocatalytic Production of H_2O_2 by Selective Oxygen Reduction Using Earth-Abundant Cobalt Pyrite (CoS_2). *ACS Catalysis*, 9(9), 8433–8442.

[158] Sheng, H., Janes, A. N., Ross, R. D., Kaiman, D., Huang, J., Song, B., Schmidt, J. R., & Jin, S. (2020). Stable and selective electrosynthesis of hydrogen peroxide and the electro-Fenton process on $CoSe_2$ polymorph catalysts . *Energy & Environmental Science*.

[159] Sheppard, D., Terrell, R., & Henkelman, G. (2008). Optimization methods for finding minimum energy paths. *Journal of Chemical Physics*, 128(13), 1–10.

[160] Shledon, R. (2012). *Metal-Catalyzed Oxidations of Organic Compounds: Mechanistic Principles and Synthetic Methodology Including Biochemical Processes*. New York, NY: Elsevier Science.

[161] Siahrostami, S., Verdaguer-Casadevall, A., Karamad, M., Deiana, D., Malacrida, P., Wickman, B., Escudero-Escribano, M., Paoli, E. a., Frydendal, R., Hansen, T. W., Chorkendorff, I., Stephens, I. E. L. S., & Rossmeisl, J. (2013). Enabling direct H_2O_2 production through rational electrocatalyst design. *Nature materials*, 12(December), 1137–43.

[162] Silbaugh, T. L. & Campbell, C. T. (2016). Energies of Formation Reactions Measured for Adsorbates on Late Transition Metal Surfaces. *The Journal of Physical Chemistry C*, 120, 25161–25172.

[163] Singh, A. K., Zhou, L., Shinde, A., Suram, S. K., Montoya, J. H., Winston, D., Gregoire, J. M., & Persson, K. A. (2017). Electrochemical Stability of Metastable Materials. *Chemistry of Materials*, 29(23), 10159–10167.

[164] Smil, V. (2002). Nitrogen and food production: Proteins for human diets. *Ambio*, 31(2), 126–131.

[165] Smith, P. T., Kim, Y., Benke, B. P., Kim, K., & Chang, C. J. (2020). Supramolecular Tuning Enables Selective Oxygen Reduction Catalyzed by Cobalt Porphyrins for Direct Electrosynthesis of Hydrogen Peroxide. *Angewandte Chemie - International Edition*, 59(12), 4902–4907.

[166] Smith R J, B., Loganathan, M., & Shantha, M. S. (2010). A review of the water gas shift reaction kinetics. *International Journal of Chemical Reactor Engineering*, 8(January).

[167] Smits, P., Kuster, B., van der Wiele, K., & van der Baan, H. (1987). Lead Modified Platinum on Carbon Catalysts For the Selectinve Oxidation of (2-) Hydroxycarbonic Acids, and Especially Polyhydroycarbonic Acids to Theiry 2-Keto Derivatives. *Applied Catalysis*, 33, 83–96.

[168] Song, X., Li, N., Zhang, H., Wang, L., Yan, Y., Wang, H., Wang, L., & Bian, Z. (2020). Graphene-Supported Single Nickel Atom Catalyst for Highly Selective and Efficient Hydrogen Peroxide Production. *ACS Applied Materials and Interfaces*, 12(15), 17519–17527.

[169] Stamenkovic, V., Mun, B. S., Mayrhofer, K. J. J., Ross, P. N., Markovic, N. M., Rossmeisl, J., Greeley, J., & Nørskov, J. K. (2006). Changing the Activity of Electrocatalysts for Oxygen Reduction by Tuning the Surface Electronic Structure. *Angewandte Chemie*, 118(18), 2963–2967.

[170] Stegelmann, C., Andreasen, A., & Campbell, C. T. (2009). Degree of rate control - how much the energies of intermediate and transition states control rates. *JACS*, 131, 8077–8082.

[171] Stoltze, P. & Nørskov, J. K. (1985). Bridging the "pressure gap" between ultrahigh-vacuum surface physics and high-pressure catalysis. *Physical Review Letters*, 55(22), 2502–2505.

[172] Strmcnik, D., Kodama, K., Van Der Vliet, D., Greeley, J., Stamenkovic, V. R., & Marković, N. M. (2009). The role of non-covalent interactions in electrocatalytic fuel-cell reactions on platinum. *Nature Chemistry*, 1(6), 466–472.

[173] Sun, Y., Silvioli, L., Sahraie, N. R., Ju, W., Li, J., Zitolo, A., Li, S., Bagger, A., Arnarson, L., Wang, X., Moeller, T., Bernsmeier, D., Rossmeisl, J., Jaouen, F., & Strasser, P. (2019). Activity-Selectivity Trends in the Electrochemical Production of Hydrogen Peroxide over Single-Site Metal-Nitrogen-Carbon Catalysts. *Journal of the American Chemical Society*, 141(31), 12372–12381.

[174] Sun, Y., Sinev, I., Ju, W., Bergmann, A., Dresp, S., Kühl, S., Spöri, C., Schmies, H., Wang, H., Bernsmeier, D., Paul, B., Schmack, R., Kraehnert, R., Roldan Cuenya, B., & Strasser, P. (2018). Efficient Electrochemical Hydrogen Peroxide Production from Molecular Oxygen on Nitrogen-Doped Mesoporous Carbon Catalysts. *ACS Catalysis*, 8(4), 2844–2856.

[175] Takehira, K., Mimoun, H., & De Roch, I. S. (1979). Liquid Phase Diacetoxylation of 1,3-Butadiene with Pd-Te-C Catalyst. *Journal of Catalysis*, 58(2), 155–169.

[176] Tang, C., Jiao, Y., Shi, B., Liu, J. N., Xie, Z., Chen, X., Zhang, Q., & Qiao, S. Z. (2020). Coordination Tunes Selectivity: Two-Electron Oxygen Reduction on High-Loading Molybdenum Single-Atom Catalysts. *Angewandte Chemie - International Edition*, 59(23), 9171–9176.

[177] Tang, W., Sanville, E., & Henkelman, G. (2009). A grid-based Bader analysis algorithm without lattice bias. *Journal of physics. Condensed matter : an Institute of Physics journal*, 21(8), 084204.

[178] Trebushat, D. V., Kuznetsova, N. I., Koshcheev, S. V., & Kuznetsova, L. I. (2013). Oxidation of 1,3-butadiene over Pd/C and Pd-Te/C catalysts in polar media. *Kinetics and Catalysis*, 54(2), 233–242.

[179] U.S. Environmen Protection Agency (2020). List N: Disinfectants for Use Against SARS-CoV-2.

[180] Vassilyev, Y. B., Khazova, O. A., & Nikolaeva, N. N. (1985). Kinetics and Mechanism of Glucose Electrooxidation on Different Electrode-Catalysts. Part II Effect of the Nature of the Electrode and the Electrooxidation Mechanism. *J. Electroanal. Chem*, 196, 127–144.

[181] Verdaguer-Casadevall, A., Deiana, D., Karamad, M., Siahrostami, S., Malacrida, P., Hansen, T. W., Rossmeisl, J., Chorkendorff, I., & Stephens, I. E. (2014). Trends in the electrochemical synthesis of H_2O_2: Enhancing activity and selectivity by electrocatalytic site engineering. *Nano Letters*, 14(3), 1603–1608.

[182] Vinod, C. P., Wilson, K., & Lee, A. F. (2011). Recent advances in the heterogeneously catalysed aerobic selective oxidation of alcohols. *Journal of Chemical Technology and Biotechnology*, 86(2), 161–171.

[183] Vinogradova, O., Krishnamurthy, D., Pande, V., & Viswanathan, V. (2018). Quantifying Confidence in DFT-Predicted Surface Pourbaix Diagrams of Transition-Metal Electrode – Electrolyte Interfaces. *Langmuir*, 34(Xc), 12259–12269.

[184] Viswanathan, V., Hansen, H. A., Rossmeisl, J., & Nørskov, J. K. (2012). Unifying the 2e–and 4e–Reduction of Oxygen on Metal Surfaces. *The Journal of Physical Chemistry Letters*, 3(20), 2948–2951.

[185] Vojvodic, A. & Nørskov, J. K. (2015). New design paradigm for heterogeneous catalysts. *National Science Review*, 2(2), 140–143.

[186] Vydrov, O. A., Heyd, J., Krukau, A. V., & Scuseria, G. E. (2006). Importance of short-range versus long-range Hartree-Fock exchange for the performance of hybrid density functionals. *Journal of Chemical Physics*, 125(7).

[187] Wang, J., Li, X., Wei, B., Sun, R., Yu, W., Hoh, H. Y., Xu, H., Li, J., Ge, X., Chen, Z., Su, C., & Wang, Z. (2020a). Activating Basal Planes of $NiPS_3$ for Hydrogen Evolution by Nonmetal Heteroatom Doping. *Advanced Functional Materials*, 1908708, 1–9.

[188] Wang, Y.-H., Mondal, B., & Stahl, S. S. (2020b). Molecular Cobalt Catalysts for O_2 Reduction to H_2O_2 : Benchmarking Catalyst Performance via Rate–Overpotential Correlations . *ACS Catalysis*, 10(20), 12031–12039.

[189] Wenkin, M., Ruiz, P., Delmon, B., & Devillers, M. (2002). The role of bismuth as promoter in Pd-Bi catalysts for the selective oxidation of glucose to gluconate. *Journal of Molecular Catalysis A: Chemical*, 180(1-2), 141–159.

[190] Witońska, I., Frajtak, M., & Karski, S. (2011). Selective oxidation of glucose to gluconic acid over Pd-Te supported catalysts. *Applied Catalysis A: General*, 401(1-2), 73–82.

[191] Wu, X., Han, S., He, D., Yu, C., Lei, C., Liu, W., Zheng, G., Zhang, X., & Lei, L. (2018). Metal Organic Framework Derived Fe-Doped $CoSe_2$ Incorporated in Nitrogen-Doped Carbon Hybrid for Efficient Hydrogen Evolution. *ACS Sustainable Chemistry & Engineering*, 6, 8672–8678.

[192] Xia, C., Xia, Y., Zhu, P., Fan, L., & Wang, H. (2019). Direct electrosynthesis of pure aqueous H_2O_2 solutions up to 20% by weight using a solid electrolyte. *Science*, 366(6462), 226–231.

[193] Yamanaka, I., Ichihashi, R., Iwasaki, T., Nishimura, N., Murayama, T., Ueda, W., & Takenaka, S. (2013). Electrocatalysis of heat-treated cobalt-porphyrin/carbon for hydrogen peroxide formation. *Electrochimica Acta*, 108, 321–329.

[194] Yang, H., Vogel, W., Lamy, C., & Alonso-Vante, N. (2004). Structure and electrocatalytic activity of carbon-supported Pt-Ni alloy nanoparticles toward the oxygen reduction reaction. *Journal of Physical Chemistry B*, 108(30), 11024–11034.

[195] Yang, S., Kim, J., Tak, Y. J., Soon, A., & Lee, H. (2016). Single-atom catalyst of platinum supported on titanium nitride for selective electrochemical reactions. *Angewandte Chemie - International Edition*, 55(6), 2058–2062.

[196] Yang, S., Verdaguer-Casadevall, A., Arnarson, L., Silvioli, L., Čolić, V., Frydendal, R., Rossmeisl, J., Chorkendorff, I., & Stephens, I. E. (2018). Toward the Decentralized Electrochemical Production of H_2O_2 : A Focus on the Catalysis. *ACS Catalysis*, 8(5), 4064–4081.

[197] Zeng, Z. & Greeley, J. (2014). Theoretical study of CO adsorption on Au catalysts under environmental catalytic conditions. *Catalysis Communications*, 52, 78–83.

[198] Zhang, J., Sasaki, K., Sutter, E., & Adzic, R. R. (2007). Stabilization of Platinum Oxygen-Reduction Electrocatalysts Using Gold Clusters. *Science*, 220(2007), 10–13.

[199] Zhang, J., Vukmirovic, M. B., Sasaki, K., Nilekar, A. U., Mavrikakis, M., & Adzic, R. R. (2005). Mixed-metal Pt monolayer electrocatalysts for enhanced oxygen reduction kinetics. *Journal of the American Chemical Society*, 127(36), 12480–12481.

[200] Zhao, W.-w., Bothra, P., Lu, Z., Li, Y., Mei, L.-p., Liu, K., Zhao, Z., Chen, G., Back, S., Siahrostami, S., Kulkarni, A., Nørskov, J. K., Bajdich, M., & Cui, Y. (2019). Improved Oxygen Reduction Reaction Activity of Nanostructured CoS 2 through Electrochemical Tuning. *ACS Applied Energy Materials*, 2(12), 8605–8614.

[201] Zhao, Z. J., Li, Z., Cui, Y., Zhu, H., Schneider, W. F., Delgass, W. N., Ribeiro, F., & Greeley, J. (2017). Importance of metal-oxide interfaces in heterogeneous catalysis: A combined DFT, microkinetic, and experimental study of water-gas shift on Au/MgO. *Journal of Catalysis*, 345, 157–169.

[202] Zitolo, A., Ranjbar-Sahraie, N., Mineva, T., Li, J., Jia, Q., Stamatin, S., Harrington, G. F., Lyth, S. M., Krtil, P., Mukerjee, S., Fonda, E., & Jaouen, F. (2017). Identification of catalytic sites in cobalt-nitrogen-carbon materials for the oxygen reduction reaction. *Nature Communications*, 8(1), 1–10.